Fabrication & Characterization of TCO-less Cylindrical Dye-sensitized Solar Cells using Metallic Wires

著者	Kapil Gaurav
year	2015
その他のタイトル	メタル細線をバックコンタクト電極に用いた透明導電膜を必要としない色素増感太陽電池の作製と光電変換特性
学位授与年度	平成27年度
学位授与番号	17104甲生工第244号
URL	http://hdl.handle.net/10228/5553

Fabrication & Characterization of TCO-less Cylindrical Dye-sensitized Solar Cells using Metallic Wires

GRADUATE SCHOOL OF LIFE SCIENCE AND SYSTEMS ENGINEERING
KYUSHU INSTITUTE OF TECHNOLOGY

THESIS

FOR THE DEGREE OF

DOCTOR OF PHILOSOPHY

GAURAV KAPIL

ENROLLMENT NO: 12897016

JUNE 2015

PHD. SUPERVISOR

PROFESSOR. SHYAM S. PANDEY

TABLE OF CONTENTS

ABSTRACT

Dye-sensitized solar cells (DSSCs) are now able to enter in to the commercialization stage after the profound researches carried over the past two decade after their successful inception in 1991. Some of the possible reasons for the popularity are their low cost of production, short energy payback time (EPBT), simple methods of fabrication and possibilities of fabricating on the flexible substrates. Cost of the solar cell is an important factor in implementing the DSSC's use at the mass consumer level having mainly three possible ways to decrease the overall cost. One approach is to design the dyes with high molar extinction coefficient such as organic dyes or to increase the absorption range of the dyes for example black dye, which increases the DSSC efficiency or output power. Second one is to increase the life-time of DSSC, which can be done by improving the dye stability, proper sealing of DSSC and replacing the corrosive redox electrolyte. Third approach is to decrease the cost of materials implemented for DSSC fabrication such as designing the cheap dye material, removal of costly transparent conductive oxide (TCO) and costly catalytic Pt etc. TCO glass is one of the expensive elements in conventional DSSC architecture. In this step, past researches for the removal of TCO have been done. Back contact TCO-less DSSC using metal mesh have been reported by our group. Further the back contact TCO-less cylindrical DSSC architecture was reported using metal mesh owing to advantage of uniform solar harvesting from all directions, higher total output power in a day compared to flat conventional DSSC, easy to carry and install. The fabrication process involved in the cylindrical DSSC is a bit cumbersome and need simplification for the commercial exploitation. Therefore, the goal of my current research was to develop a new cylindrical architecture for DSSC which could solve some of the previously existing problems in cylindrical DSSC architectures. In this report, I will discuss mainly the following points.

(1) Different flexible metal wires such as Copper (Cu), Stainless-Steel (SS) and Titanium (Ti) were employed to fabricate the novel cylindrical DSSC and we gave it a name as coil type cylindrical DSSC (C-DSSC). The fabrication steps involved were fast and easy. We have shown that the nature of the wire plays an important role on the performance of the solar cells. The effect of surface passivation on the metal wire surface with a thin layer of Ti was discussed. Electrochemical Impedance spectroscopy (EIS) analyses were done to investigate about the differential performance of the solar cell using different metal wires.

(2) Relatively lower resistance, good flexibility, superior corrosion resistance and high temperature tolerance of Ti wire make it a better choice for C-DSSC. Here we presented the comparative study of the photovoltaic characteristics of the solar cells prepared with Ti wires having different diameters. The Ti wire surface was modified using hydrogen peroxide (H_2O_2). This surface treatment have been found to influence the adhesion as well as electrical contact between coated nanoporous titanium oxide (TiO_2) and Ti-wires. The results were supported by X-ray diffraction (XRD), X-ray photoelectron spectroscopy (XPS) and scanning electron microscopy (SEM).

(3) Diffused light performance is one of the application areas of DSSC where they can outperform to their inorganic solar cell counterparts. In this part we investigated the 1 SUN and low light intensity fluorescent light performance of Ti wire based C-DSSC using ruthenium based N719 dye and organic dyes such as D205 and Y123. The cylindrical geometry gives an advantage above flat conventional DSSC i.e. it allows to use the reflectors to further enhance the output power. Therefore, we used different parabolic reflectors to tap diffused light for indoor applications. Effect of shape and size of the reflector geometry on the C-DSSC performance was also investigated. Optical simulation software Trace Pro 7.5.1 was also used to analyze the spectral distribution on the TiO_2 surface.

CHAPTER 1: INTRODUCTION

1.1 General overview of solar cells

Renewable energy consists of the resources which continue to restore without human involvement. These resources include solar, wind, geothermal and hydro energies. Fossil fuels, such as coal and oil are non-renewable. They are produced when plant and animal matter decays within the earth-crust & this process takes a substantial amount of time to form usable fuel. These resources have proved their effectiveness for the progress of world economy. However, in the coming future the energy consumption and, therefore, total energy demand is going to increase with the ever increasing population. It has been reported that there will be need of about 28 TW by the year 2050 considering the similar rate of population growth and standard of human life[1-3]. The environmental issues such as greenhouse gas emissions and their impact on weather and climate which are also one of the concerns of using the non-renewable energy resources have encouraged the research for advancement of green energy and implementation of energy saving green technologies. Moving towards the clean and environment friendly renewable energy resources would be the future of energy sector. Recent past have seen the high increase in the cost of coal and oil which also led to the intensive research in different renewable energy sectors focusing on reducing their manufacturing costs. There are different kinds of renewable energies such as wind energy, hydro energy, geothermal energy, solar energy, tidal energy etc. as shown in Figure. 1 [4]. These sources have ability to provide 3000 times the current global energy demand [5].

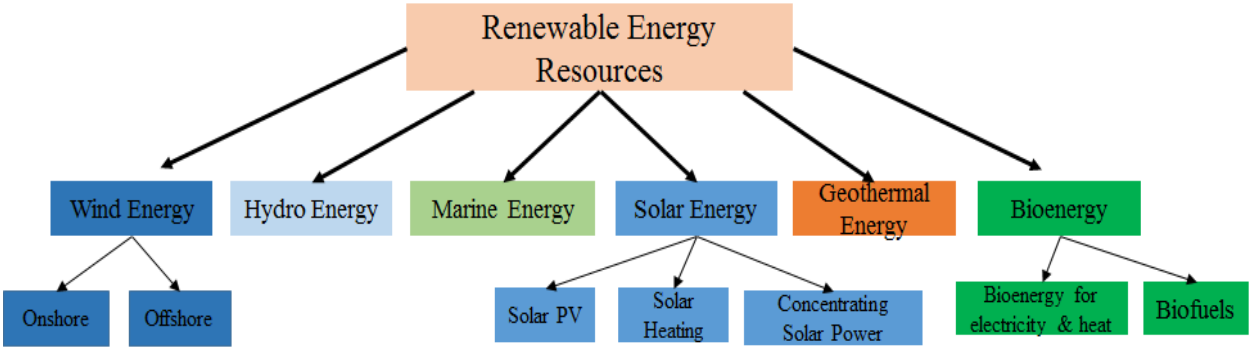

Figure 1. Different types of renewable energies

The total electricity being generated is expected to increase 2.7 times from 2010 to 2035 as shown in Table 1 [6]. In this category solar photovoltaic (PV) system is now third most important renewable energy source after hydro and wind power**.** In 2013, its fast-growing capacity increased by 36% to a running total of 136 GW, worldwide. The solar cell is the main component of PV systems. It converts solar energy directly into the usable direct-current (DC) electricity. These solar cells when connected together known as PV modules & gives increased output power in the range of few watts (W) to megawatts (MW). The modules are combined with electrical components such as inverters, batteries, mounting systems etc. to form a PV system. There are mainly three different categories of solar cell family. Single and polycrystalline silicon based solar cells are the first generation solar cells which are highly efficient and most popular. The second generation solar cells are thin film semiconductor (such as CIGS, CZTS, and CdTe etc.) based which are less efficient than first generation solar cells, however, their comparative manufacturing costs are less. The third generation solar cells which includes dye-sensitized solar cells (DSSCs), Organic solar cells and recently became popular solution processed organic-inorganic hybrid solar cells (OIHSCs) are most researched and standing on the door-steps of commercialization with some still remaining issues to be solved like cost, flexibility and durability etc.

Table1. World renewable energy use by type [6]

	2010	2020	2035
Electricity generation (TW h)	**4206**	**6999**	**11,342**
Bioenergy	331	696	1,487
Hydro	3431	4513	5,677
Wind	342	1272	2,681
Geothermal	68	131	315
Solar PV	32	332	846
Concentrating solar power	2	50	278
Marine	1	5	57
Share of total generation	**20%**	**25%**	**31%**
Heat demand (M toe)	337	447	604
Industry	207	263	324
Buildings & agriculture	131	184	280
Share of total production	10%	12%	14%
Bio fuels (mboe/d)	1.3	2.4	4.5
Road transport	1.3	2.4	4.4
Aviation	-	-	0.1
Share of total transport	2%	4%	6%

1.2 Flexible solar cells

Development of next generation solar cells on the flexible substrates with the reduced cost of fabrication is now not only the one of the highly researched areas but is the demand of time also [7-10]. These kind of solar cells are making the way for low cost electricity. Apart from being flexible they are light in weight, unbreakable, suitable for both indoor and outdoor applications & can be easily integrated with different shape elements along with faster payback time than conventional solar cells [11]. Flexible substrates have been used for organic, inorganic and organic-inorganic hybrid solar cells mostly using roll to roll printing technologies.

1.2.1 Silicon based flexible solar cells

The use of thin Si (both crystalline and amorphous) wafers for making flexible solar cells is one of the researched area with typical efficiency value in the range of 6% to 13.7% [12-15]. Very recently Sun *et.al* have used Si thin films with less than 50 μm thickness for making highly flexible and stable solar cell to reduce the materials cost [16]. In recent years some startup companies for example United Solar Ovonic (Michigan, USA) and Flexcell (Switzerland) have been involved in high-volume production of flexible solar cells [11]. Kaneka (Japan) which is one of the leading solar cell company also manufactures thin Si wafer based solar cells and are highly in demand because of its low cost and fast energy payback time compared to bulk Si based solar cells. Above all these still there are areas to be improved such as traditional manufacturing processes and efficiency. To fabricate thin Si films the wire cutting process involved is not suitable to manufacture at mass level because of their brittleness. Also for making p-n junction the doping needs to be done at high temperature which is a costly process and includes the risk of damage to the thin Si wafers [16] which impose to develop new methods.

1.2.2 CIGS based flexible solar cells

Copper Indium Gallium Diselenide [$Cu(InGa)Se_2$ (CIGS)] or chalcopyrite thin films solar cells are highly efficient amongst all of the inorganic thin film based photovoltaic devices. Efficiency around 20.3% has already been achieved on the rigid glass substrate. The research for fabricating

CIGS thin films on flexible substrates is being carried out since more than a decade [17]. Initially it was found to be difficult to achieve high efficiency on the flexible substrates, however, recently Azimi et al [18] have achieved efficiency around 18.7% on a polyamide film. There are so many companies and research institutes from USA, Europe and Japan which are involved in fabricating flexible CIGS based solar cells aiming towards reduction of fabricating cost keeping the photoconversion efficiency to be nearly the same. The methods currently being utilized for the preparation of the chalcopyrite absorber layer are sophisticated and expensive. Therefore, the focus is being directed on low-cost and vacuum-free processes such as electrodeposition using nanoparticle metal slurries as summarized in Table 2 [19].

Table 2. CIGS fabrication on different flexible substrates

	Institute or company	**CIGS process**	**Substrate**	**Special features**
USA	NREL, GSE, ITN	Co-evaporation	Stainless steel(SS), SS, polyimide (PI)	Highest eff. On SS roll-to-roll (ca. 1ft), patterning on PI roll-to-roll
	IEC		PI	
	DayStar		Ti	
	Florida Solar Energy Center	Sequential sputtering of precursors, sulfurisation non-vacuum, metal oxide precursors, printed or sprayed, selenisation	SS	In-line compatible, scalable
	ISET, UNISUN		Ti, Mo, PI	Low-cost process, allows the integration of patterning steps
Japan	Matsushita Electric	Co-evaporation	SS	High-eff process, roll-to-roll(width ca, 1ft)
Europe	ZSW, Univ. Struttgart (IPE), HMI, ETH Zurich, Univ. Uppsala (ASC)	Co-evaporation	SS, PI, Ti	ZSW: large-area evap. Sources
	Shell Solar (Germany)	Sequential sputtering of precursors, selenisation/sulfurisation	SS	In-line compatible, scalable
	Institut fuer Solartechnologien (IST)	electrodeposition of $CuInS_2$, sulfurisation	Cu-tape as substrate and back contact	Special non-vacuum process, roll-to-roll (1cm, Cu tape), series interconnection by shingling technique
	CIS solartechnik	Electrodeposition	SS(Cu)	Metal tape (3.5 cm) Roll-to-roll (20cm), special ion-beam-supported evaporation
	Solarion	Co-evaporation	PI, (Ti)	

1.2.3 Plastic Solar cells

After the discovery of semiconducting behavior in π-conjugated organic materials (known as conducting polymers/conjugated polymers), there has been a lot of research utilizing this property in different electronic devices such as light emitting diodes (LEDs), field effect transistors (FETs) and solar cells. Organic semiconductors show significant advantage over their inorganic counterparts, e.g. solution processed thin films of the organic materials can be prepared by low-cost methods such as drop costing, spraying, doctor blade coating, spin coating etc. This also gives the possibility of fabricating these devices on the flexible substrates such as conducting Indium-Tin-Oxide coated polyethylene terephthalate (PET/ITO) films [20], metallic foils (e.g. Stainless Steel, Titanium) [21-22], Silver nanowires (AgNWs) [23-26], carbon nanotubes [27-28] and graphenes [19-30]. This mechanical flexibility has further developed the interest for the applications in the areas of wearable electronics and robotics [31-32]. In fact, solar cells based on organic semiconductors are less expensive, easier to manufacture with more possibilities to tailor their material property. In this category bulk heterojunction (BHJ) solar cell, which is a distributed junction between polymers based donor and acceptor material [33] and dye-sensitized titanium oxide thin film, which is an artificial photosystem [34] have been popular for the flexible solar cells. Although they have less efficiency compared to inorganic flexible solar cells but are more popular due to their fast energy payback time and suitability for indoor aesthetic attributes. So many companies are now involved in commercializing the flexible DSSCs recently. Dyesol (Australia) is now providing dye-sensitized solar cells (DSSCs) based foldable, light weight solar panels for military applications [35] which is capable of working in wide range of lighting conditions. High efficiency is not always important in some of the applications, therefore consumers care more about the output power. The US based G24 innovation produces modules which are less than 1 mm thick with power capacity in range of 25 MW to 200 MW. They are manufacturing small flexible solar cells for various applications such as consumer electronics (wireless keyboard for Apple IPAD is recently popular), sensors & actuators and in retails. Israel based Solar 3G has developed flexible DSSC modules with 40% less cost per megawatt in comparison to silicon based solar cells [37]. The above discussion highlights some of the past and recent advances in the area of solar cells with a target to reduce the dependency on the non-renewable energy resources. Further, solar cells are in great demand as the Sun is singular source

for unlimited energy. But the cost utilized in harnessing this energy into useful electricity needs cheap PV systems, which can be possibly achieved by thin film based inorganic-organic solar cells.

1.3 Gratzel solar cell or Dye-sensitized solar cells (DSSCs)

1.3.1 Introduction & general working principle

DSSC works on the principle of photoelectric effect where light energy is converted to electric energy. This concept was first coined by the French scientist Edmond Becquerel [38] and since after that based on it several new concept came. The principle involved in PV system depends on capturing the available photons from the sunlight by the semiconductor surface. This results in generation of electron-hole pairs at the junction between two different semiconductor materials which causes in the formation of an electric potential across the junction responsible for dissociation of the exciton (or electron-hole pair) in to the free charge carriers. DSSCs are one of the attractive alternative to expensive solid semiconductor junction devices based on silicon. With recent progress in these new generation photovoltaics based on nanomaterials there are enormous opportunities for existing PV industries and researchers to use them for future energy based applications. The working principle of DSSC is different from conventional inorganic solar cells. It involves the photon absorption by the molecules then converting it to the electric charge without intermolecular transport of electronic excitation [39]. The light harvesting & the charge transport takes place separately, due to which the options for the light absorbing materials are more. These two process takes place simultaneously in inorganic solar cells which restricts the choice of the materials. The charge transport in DSSC is only due to the majority carriers whereas in inorganic solar cells it is due to both minority and majority carriers. The structure of the DSSC cell is shown in the Figure 2. Sensitizing dye molecules play a central role in the operation of DSSCs and controls the device performance since they are the actual harvesters of the photons. They can be visualized as the mimic of natural photosynthesis where dye molecules captures the light energy converting them to the usable chemical energy. The dye molecules are placed at the interface between electron transport (n-type semiconductors such as TiO_2, ZnO, SnO_2) and hole transport (redox electrolyte or a p-type semiconductor) material. The photogenerated electron are injected into the conduction band of n-type semiconductor and the hole thus formed in valence band of the

dye thus are filled by the electron from the redox electrolyte (HOMO level) or p-type semiconductor.

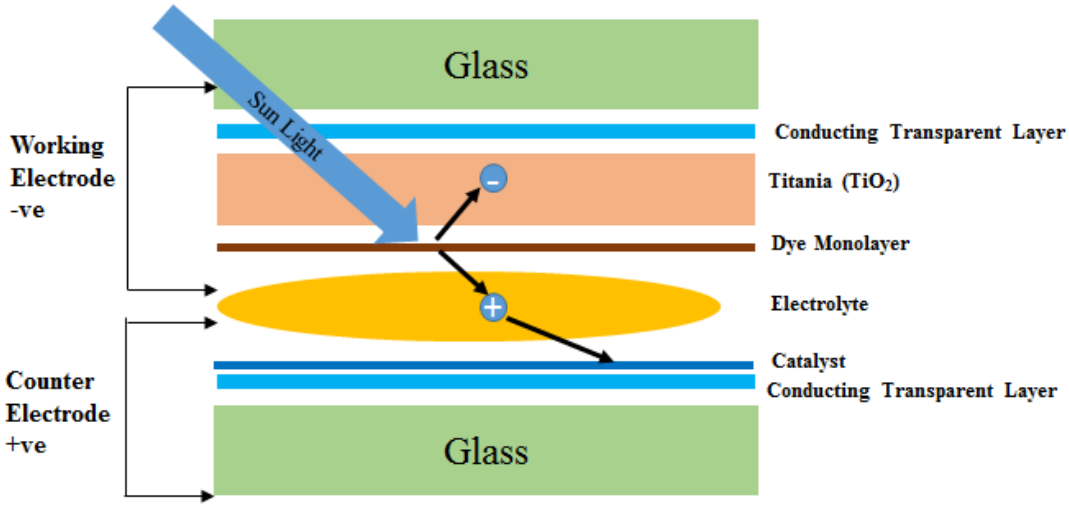

Figure 2. Schematic diagram showing operations involved in the functioning of DSSCs.

1.3.2 Energy band diagram with involved process dynamics

The energy band diagram with different processes involved is drawn in Figure 3. The performance of DSSC depends on the relative energy levels and the rate of the reactions involved at the sensitized TiO_2 & electrolyte interface. The process involved can be written in the following form:

$$TiO_2/S + h\upsilon \rightarrow TiO_2/S^* \quad (1)$$

$$TiO_2/S^* \rightarrow TiO_2/S^+ + e_{cb} \quad (2)$$

$$TiO_2/S^+ + e_{cb} \rightarrow TiO_2/S \quad (3)$$

$$TiO_2/S^+ + 3/2\ I^- \rightarrow TiO_2/S + 1/2\ I_3^- \quad (4)$$

$$1/2\ I_3^- + e_{(Pt)} \rightarrow 3/2\ I^- \quad (5)$$

$$I_3^- + 2\ e_{cb} \rightarrow 3I^- \quad (6)$$

The average time scales involved in the respective processes are also shown in the Figure 3 [40]. Upon the photoexcitation, dye molecules reaches to the excited state (S*) and photogenerated electron are transferred to conduction band of semiconductor in pico to femto seconds **(1&2)**. The dye is regenerated by the electrolyte **(4)** in microseconds. The recombination process involved the back transfer of the electrons from TiO_2 surface to HOMO of the sensitizer **(3)** or with the redox

electrolyte **(6)**. These recombination process takes place in the time range of milli seconds. These recombination process needs to be suppressed to their minimum possible extent for the attainment of high performance of the solar cell. The normal process of I_3^-/I^- conversion is supported by the electron transfer from catalytic surface of platinum (Pt), which is an ion diffusion process. In all, for high efficiency of the DSSC, first the rate of electron injection must be faster than decay of the excited dye. Second the rate of dye regeneration from electrolyte must be faster than rate of back electron transfer from injected electron in TiO_2 to excited dye, as well as the rate of reaction of injected electrons with electrolyte. Third one is the kinetics of the reaction at the counter-electrode **(5)**.

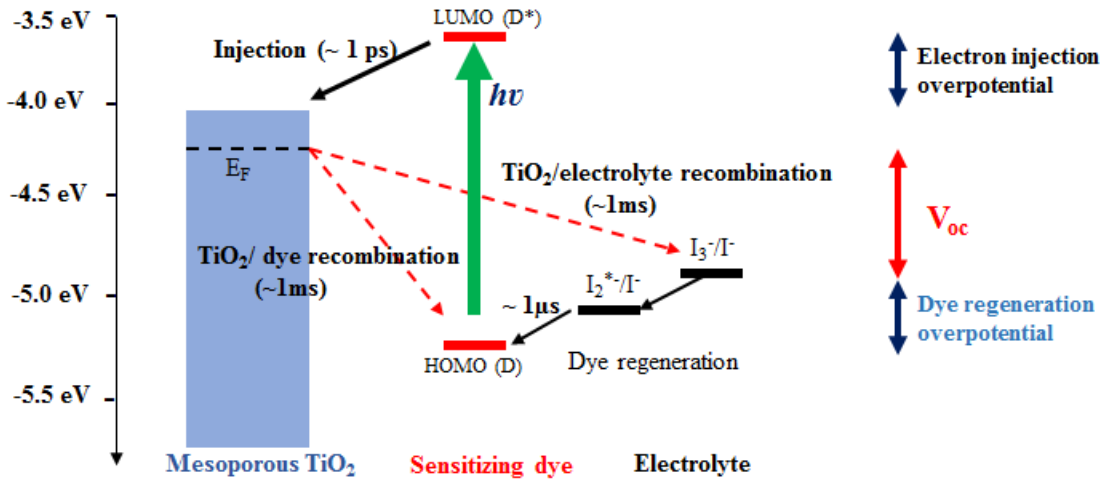

Figure 3. Schematic energy band diagram for DSSCs

1.4 TCO-less Dye-sensitized solar cells

DSSCs are undoubtedly a most interesting and feasible concept developed from the molecular photovoltaic effect [41, 42], for developing cost effective photovoltaic cells with high photoconversion efficiency to meet the global energy demand [43, 44]. Their emergence have led to the competition for solid-state junction solar cells. DSSCs offer cheap fabrication together with possibility of fabricating on flexible substrate. The recent progress in fabrication methods and the nanocrystalline materials has added the new opportunities in PV industry. For industrial application point of view, cost of production and ease of fabrication are crucial issues which are needed to be solved and requires attention of the researchers. Conventional DSSCs utilize a

transparent conducting oxide (TCO) electrode which is one of the bottlenecks towards the cost reduction and alone is responsible for 16% of overall cost for fabricating the DSSC based PV capacity of 1 MW_{peak}/year [45, 46]. Therefore, this have opened the research for developing new architectures without TCO in a manner to match the efficiency of standard DSSCs while reducing the cost [46–49]. TCO–less design apart from its advantages for fabrication in a variety of device architectures and enhanced areas of application avoids losses due to optical transmission enabling it to absorb light in the near infra-red (NIR) to IR wavelength region also. Kashiwa et al have reported all metal type flat DSSCs devoid of TCO completely having nearly similar photoconversion efficiency as compared to its TCO-based counterparts [46]. The design is typical back contact DSSC utilizing flexible Ti foil sputtered with Pt to work as a counter electrode as shown in Figure 4(a). Formation of working photoanode was done in an interesting manner. In this design first a layer of mesoporous TiO_2 was coated on a glass slide. Then tetrapod-shaped ZnO was deposited using electrospray apparatus followed by sputtering of thick Ti as back current collector. This substrate then finally washed with HCl solution to make straight holes in the

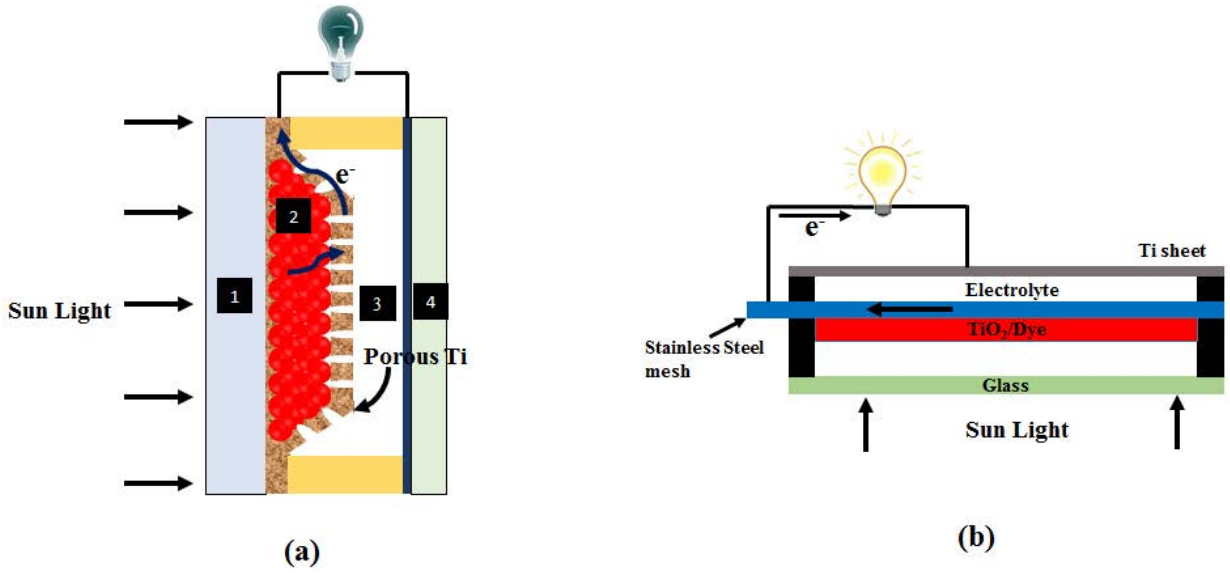

Figure 4. (a) Typical back contact TCO-less DSSC using porous Ti (b) Typical back contact TCO-less DSSC using stainless steel mesh sputtered with TiOx layer

sputtered Ti layer due to the tetra-pod ZnO. This complicated fabrication process was further made easy by Yoshida et al [47]. They used flexible Stainless-Steel metal mesh sputtered with TiOx layer as working electrode as shown in Fig. 4(b). This TiOx layer was compensating the stress caused by the difference in the thermal expansion coefficient between the stainless-steel and

porous TiO_2 layer, which helps to reduce the charge recombination. Research interest in TCO-less structure is relatively new. Figure 5 shows research for TCO-less design which was started since 2006 only, and very few laboratories are involved in it. This figure shows the number of publications on DSSC, TCO-less design, Cylindrical DSSC and Cylindrical TCO-less design since 1991. It indicates very few publications approximately around 49 on TCO-less architecture, which motivates the new architectures to be developed with more easily and comfortable fabrication processes especially compatible with existing industrial technologies.

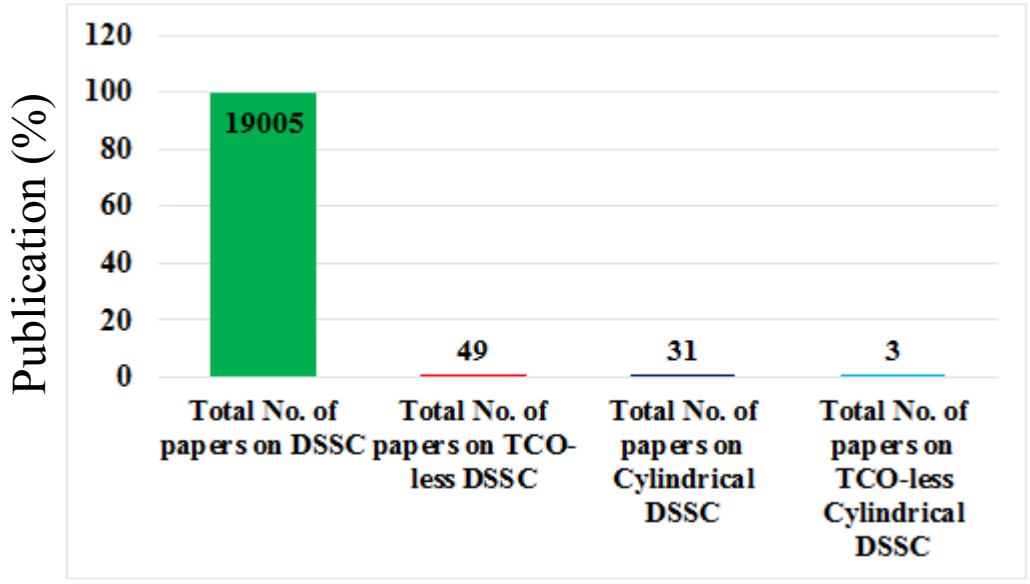

Figure 5. Data obtained from web of science on 24 March 2015. It shows the number of publications since 1991.

1.5 Cylindrical solar cells

Cylindrical architecture of the solar cells is one of the attractive ways to harness the solar energy more effectively. Due to their shape and construction cylindrical PVs exhibit unique features that a flat or conventional PVs don't have. Commercially, it has been implemented by some companies in Europe and US for example Sapagroup (Netherlands), Solaroad Technologies (US) etc . Solyndra, a US based startup company was one of the companies which started manufacturing solar cells which looks like a black fluorescent light tubes using CIGS (copper/indium/gallium/selenium) thin films with efficiency of 12 % to 14% [50]. However, later

on August 2011 due to high prices of the silicon solar cells led the company to shut down all its operating and manufacturing units as they were not able to compete with conventional silicon solar panels [51]. A cylindrical solar cell generates relatively more electricity as compared to the flat type commercial and industrial rooftop solar cells due to its device architecture. Some of its advantages are listed below:

1. **360 degree light harvesting:** This is one of the important advantage of cylindrical PV modules as they are capable of harvesting light from all the angles. There is no need of changing the direction of the solar cell, as cylindrical geometry allows equal light harvesting from all the angles throughout the day which can be seen from Figure 6. These solar cells have another advantage of absorbing the reflected light from the bottom of the surface, therefore, if implemented with reflecting bottom surface can produce more electricity. They can be spaced much more close together than conventional solar panels and enables more rooftop coverage with increased energy production.

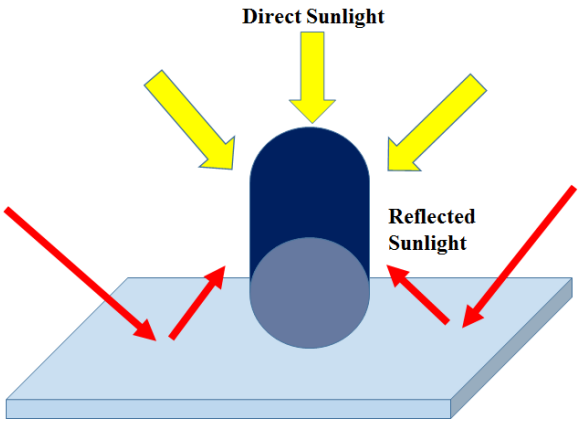

Figure 6. Cylindrical shape of the solar cell allows both direct and reflected sunlight to be absorbed

2. **Less wind loading:** Wind can easily pass through the cylindrical PV modules. These modules have shown their durability in countries such as Japan where typhoons are very strong. Some manufacturers have claimed that these modules can withstand wind strengths of up to force twelve [To measure wind speed Beaufort wind force scale is used, Force 12 is condition of hurricane]

3. **Reduce sealing area:** Efficient sealing is an important requirement to provide the durability to the solar cells and offers sufficient amount of cost burden. The cylindrical design of solar cells allow the sealing length which is less than a third from flat solar cell designs [52]. Technologically it is much simpler also to seal a tube than a conventional flat solar cell.

1.6 Cylindrical TCO-less Dye-sensitized solar cell

These solar cell architectures are the result of combining TCO-less DSSC concept with the cylindrical device architecture. The different configurations of cylindrical TCO-less came into picture in last few years and most of them were implemented using flexible metal substrate and wires as shown in Figure 7. Type A is the simplest way to fabricate cylindrical architecture based DSSCs. Both the counter and working electrode are kept parallel inside an electrolyte filled tube, but in this case light could be allowed to fall from only working electrode side, as counter electrode side would have shading effect. Type B~D architectures have no shading effect and can receive light from all the angles. Fan et al have designed the Type B using helical twisted working electrode (stainless-steel wire) coated with mesoporous TiO_2 and counter electrode (Pt wire) with the same diameter [53]. Due to use of equal diameter wires twisting causes stress which effects the solar cell performance. Also it causes less exposure of light to the working electrode. Therefore, Type C was developed using relatively thinner wire working as counter electrode and wrapped over a straight thick photoanode [54, 55]. In these architectures Ti wire was used as working electrode and twisted Pt wire as counter electrode. Both the working and counter electrodes were in direct contact, therefore pressure at the interfacial contact plays an important role in solar cell performance. Also, the thread pitch distance impacts the exposure area and the mass transport.

To avoid the pressure effect on the photoanode, Type D and Type E came into the picture [56-58]. Another advantage was the full exposure of the working photoanode, which can be considered as improvement over the Type A, B, & C. Type D is just an opposite architecture to Type C, as in this case working electrode was twisted and counter electrode is straight. Type E is also almost similar to type D, only difference is the twisted counter electrode in spiral shape. In

both of the types D and type E a large amount of Iodine based electrolyte as a redox was needed to be filled. All the structures mentioned from Type A to Type E are metallic wire based. The Type F and Type G uses the metal mesh coated with mesoporous TiO_2. Type F is the typical TCO-less planar DSSC structure. In the Type G design, the metal mesh was rolled around the counter electrode made up of either mesh or rod coated with thin Pt layer [59, 60]. The cylindrical DSSC was fabricated using flexible metal mesh based photoanode, Ti rod sputtered with Pt as counter electrode and porous polymer film soaked with electrolyte into a cylindrical glass tube.

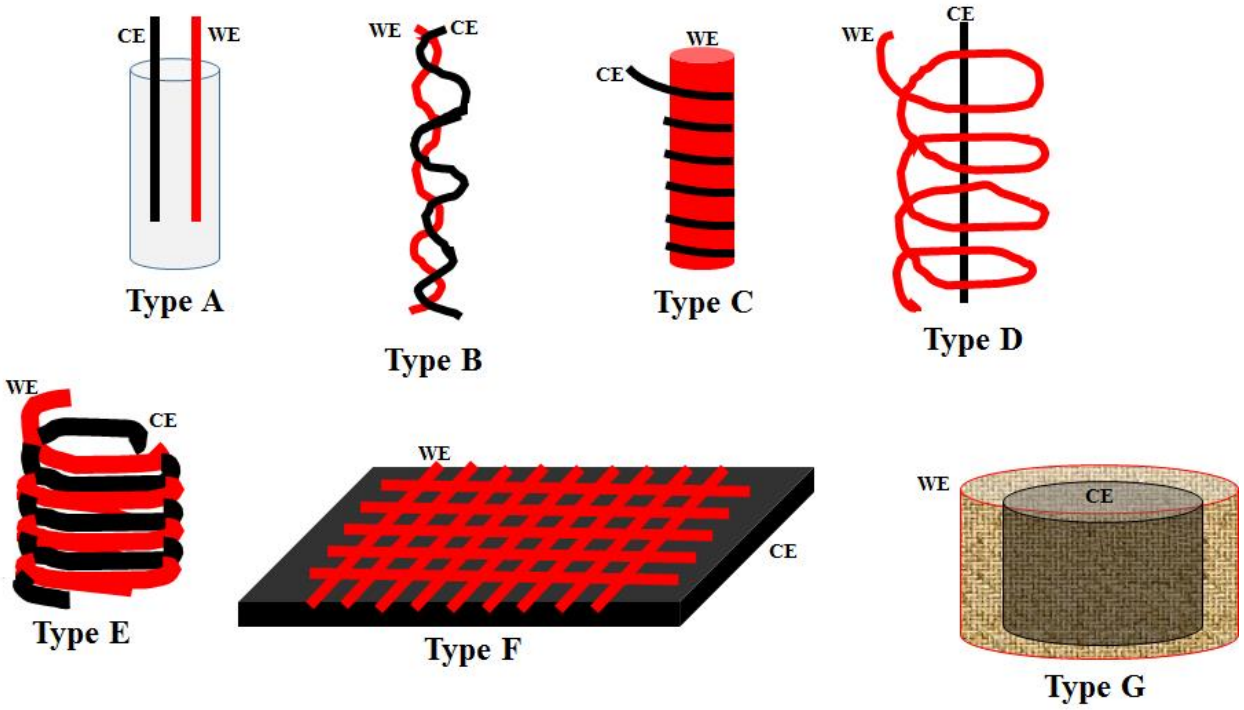

Figure 7. Different possible architectures used for cylindrical DSSC fabrication using metallic wires and mesh

1.6.1 Calculation of photoconversion efficiency for cylindrical solar cells:

The calculation involved in the measurement of device performance of the cylindrical electrode based solar cells is quite different from planar solar cells and needed to be discussed properly. The active area is the key point in performance calculation as it is difficult to define the exact illumination area. The percentage photoconversion efficiency (PCE η %) can be calculated as follows

$$(\eta\%) \quad = \frac{Pout}{Pin} * 100 = \frac{Jsc*Voc*FF}{Pin} * 100$$

Pout is the output power, *Pin* is the input power of the light source, *Jsc* is the short circuit current density, *Voc* is the open circuit voltage, *FF* is the fill factor. Among all these parameters the *Jsc* is affected by the active area selection, which finally affects the PCE. Metal wire based DSSC usually have small surface area. The diameter used up to now by the researchers are mostly less than 0.5 mm. The variation of current density with the active area of irradiation at different current flow shown in Figure 8 [61].

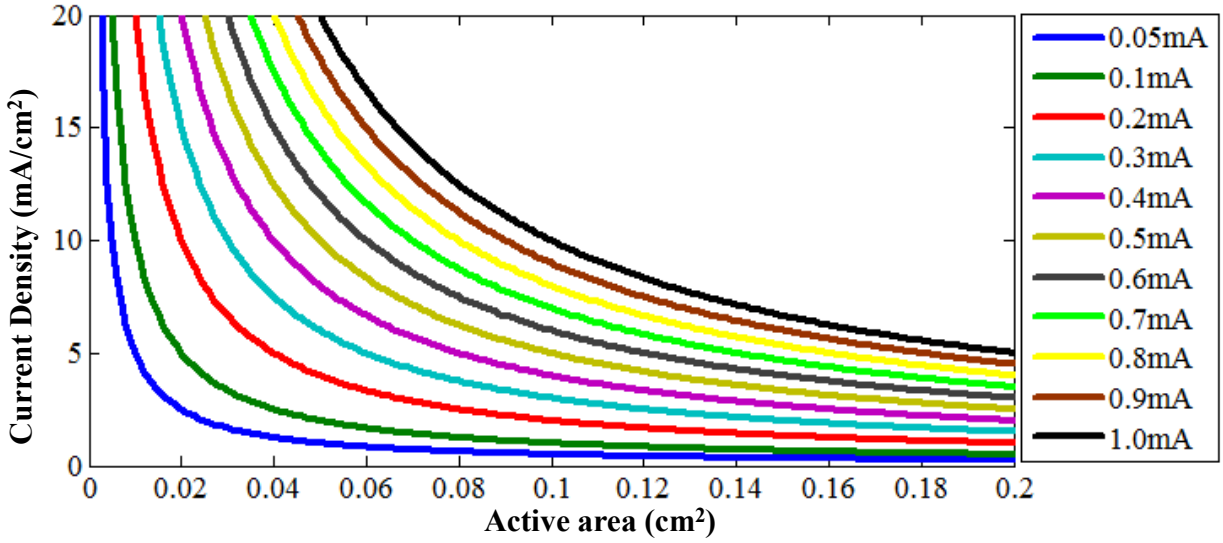

Figure 8. Current density variation with the active area at different net current flow in the device

It can be clearly seen that both of current density and active area under the consideration follows the inverse relation i.e. *Jsc* will be high at small area of irradiation & will be less at large active area. For example for the current being flown of 1 mA in a device of 0.20 cm^2 active area, Jsc is 5 mA/cm^2 and for a small active area of 0.05 cm^2 in a device with same current flow Jsc is as much as 20 mA/cm^2. Therefore, exact active area for the device performance is needed to be evaluated. It is a general practice to take the projection area of the cylindrical curved surface as the active area. This method is adopted on the basis of assumption that a parallel light is irradiating to the cylindrical solar cell surface. The projected area is $\pi/2$ times less than actual surface area of the cylindrical solar cell, when half of the area is considered. Therefore, one has to be careful while

presenting the solar cell efficiency. Other complication occurs when the diameter of cylindrical surface changes with the thickness of photoactive layer after coating, hence true illumination area is difficult to find [62, 63, 64-66]. Further, in the hollow cylindrical architectures such as Type D, E and G, some part of irradiating light after passing through first half could fall on the other half, which is generally not considered. In such cases the projection area of spiral photoanode [57, 67] or in some studies projection area of whole device was taken [68]. This becomes more complicated in case of metal mesh based cylindrical solar cells such as Type G design, as space between the mesh is also included in the active area [69], which might underestimate the device performance. To understand the actual active area some studies using imaging software has been done also [70]. To avoid all these discrepancies in measurement some studies have only shown total photocurrent obtained instead of current density [58, 53].

1.7 Challenges & ideas to overcome

Cylindrical TCO-less design has undoubtedly able to solve the issues related to cost of fabrication (as TCO is responsible for 16~24% of the total production cost [45]), flexibility requirement, aesthetic aspects and total mass of the module (64% of the total mass of module is due to TCO glass [71]). However, still there are lot of engineering efforts required to modify the various designs as shown in Figure 7 to further enhance the performance, durability and cost effectiveness. The Type B & C involves twisting of the wires, which may result in short circuiting. In structures like Type B, some porous polymer layer can be introduced so as to avoid the short circuiting and also it releases the stress between the wires twisted [53]. Another approach is the use of porous insulating layer such as SiO_2 [57, 58, 68]. All the structures shown suffers from back side darkness, as only one half is under the illumination. The other half which is in darkness, increases the resistance and hence reduces the overall cell performance. Therefore, proper PV systems needed to be developed. In this case a light reflector can be used [80] to increase the output power. Further the reflector geometry is needed to be considered. Proper coating of TiO_2 on the curved and flexible surfaces is an important aspect for the attainment of better performance of the device. Cracks are usually seen on the TiO_2 films coated [57, 58, 70], tensile deformation of the substrate leads to the loss in adhesion of TiO_2 film with the substrate [72, 73]. Generally the effect of tensile deformation is more on the nanoparticle coating [81], therefore coating of nanotubes and nanowires is

preferable as these are more tolerant to the tensile stress. However, for their coating on the metallic substrates like anodization conditions has to be optimized along with the control of thickness [74, 75].

Further studies are needed to be done to check the mechanical property of the nanotubes and nanowires on the flexible substrates to improve the device performance. Sealing of the cylindrical solar cell is another important issue. Type A, D, E & G are usually sealed inside the glass tube, which is not flexible. Also the amount of electrolyte filled is very large, which effects the device performance. To circumvent these issues, one possible approach is the use of plastic heat shrinkable tubes which is expected to solve these problems i.e. it gives flexibility and also one can adjust its volume for the required amount of electrolyte [59, 60]. The other possible approach could be the development of solid hole conducting materials so that liquid electrolyte can be avoided, and problem such as light absorption by large amount of electrolyte can be removed. Another important issue is the counter electrode fabrication which is also need to be discussed. Its arrangement in the device architecture affects the cell performance. For example in Type C structure counter electrode is wrapped above the working electrode causing light hindrance. Also its pitch distance [53, 57], diameter [59, 78], surface roughness [76] and Pt layer thickness [77, 78] affect light absorption, mass transport and redox processes involved. In fact, for the better performance of the cell, counter electrode should possess a good conductivity and high catalytic activity. Therefore, a combination such as Pt nanoparticle on a graphene fiber or on carbon fiber [77, 79] can be implemented.

References:

1. Hagfeldt, A., Boschloo, G., Sun, L., Kloo, L., & Pettersson, H. (2010). Dye-sensitized solar cells. *Chemical reviews*, *110*(11), 6595-6663.
2. Service, R. F. (2005). Is it time to shoot for the sun? *Science(Washington, D. C.)*, *309*(5734), 548-551
3. Potočnik, J. (2007). Renewable energy sources and the realities of setting an energy agenda. *Science*, *315*(5813), 810-811.
4. Brown, A., Müller, S., & Dobrotkova, Z. (2011). Renewable energy: Markets and prospects by technology. *IEA information paper*.
5. RE-thinking2050, ⟨www.erec.org⟩ [accessed on 9/4/2015].
6. Ellabban, O., Abu-Rub, H., & Blaabjerg, F. (2014). Renewable energy resources: Current status, future prospects and their enabling technology. *Renewable and Sustainable Energy Reviews*, *39*, 748-764.
7. Chopra, K. L., Paulson, P. D., & Dutta, V. (2004). Thin-film solar cells: an overview. *Progress in Photovoltaics: Research and Applications*, *12*(2-3), 69-92.
8. Lewis, N. S. (2007). Toward cost-effective solar energy use. *Science*, *315*(5813), 798-801.
9. Blom, P. W., Mihailetchi, V. D., Koster, L. J. A., & Markov, D. E. (2007). Device physics of polymer: fullerene bulk heterojunction solar cells. *Advanced Materials*, *19*(12), 1551-1566.
10. Li, G., Zhu, R., & Yang, Y. (2012). Polymer solar cells. *Nature Photonics*, *6*(3), 153-161.
11. Pagliaro, M., Ciriminna, R., & Palmisano, G. (2008). Flexible solar cells. *Chem Sus Chem*, *1*(11), 880-891.
12. Baca, A. J., Meitl, M. A., Ko, H. C., Mack, S., Kim, H. S., Dong, J. Y., Ferreira, P. M. & Rogers, J. A. (2007). Printable Single-Crystal Silicon Micro/Nanoscale Ribbons, Platelets and Bars Generated from Bulk Wafers. *Advanced Functional Materials*, *17*(16), 3051-3062.
13. Yoon, J., Baca, A. J., Park, S. I., Elvikis, P., Geddes, J. B., Li, L., ... & Rogers, J. A. (2008). Ultrathin silicon solar microcells for semitransparent, mechanically flexible and microconcentrator module designs. *Nature materials*, *7*(11), 907-915.

14. Wang, S., Weil, B. D., Li, Y., Wang, K. X., Garnett, E., Fan, S., & Cui, Y. (2013). Large-area free-standing ultrathin single-crystal silicon as processable materials. *Nano letters*, *13*(9), 4393-4398.

15. Jeong, S., McGehee, M. D., & Cui, Y. (2013). All-back-contact ultra-thin silicon nanocone solar cells with 13.7% power conversion efficiency. *Nature communications*, *4*.

16. Sun, H., Wei, J., Jia, Y., Cui, X., Wang, K., & Wu, D. (2014). Flexible carbon nanotube/mono-crystalline Si thin-film solar cells. *Nanoscale research letters*, *9*(1), 1-6.

17. Başol, B. M., Kapur, V. K., Leidholm, C. R., Halani, A., & Gledhill, K. (1996). Flexible and light weight copper indium diselenide solar cells on polyimide substrates. *Solar energy materials and solar cells*, *43*(1), 93-98.

18. Azimi, H., Hou, Y., & Brabec, C. J. (2014). Towards low-cost, environmentally friendly printed chalcopyrite and kesterite solar cells. *Energy & Environmental Science*, *7*(6), 1829-1849.

19. Kessler, F., Herrmann, D., & Powalla, M. (2005). Approaches to flexible CIGS thin-film solar cells. *Thin Solid Films*, *480*, 491-498.

20. Tong, F., Kim, K., Martinez, D., Thapa, R., Ahyi, A., Williams, J., ... & Park, M. (2012). Flexible organic/inorganic hybrid solar cells based on conjugated polymer and ZnO nanorod array. *Semiconductor Science and Technology*, *27*(10), 105005.

21. Yun, H. G., Jun, Y., Kim, J., Bae, B. S., & Kang, M. G. (2008). Effect of increased surface area of stainless steel substrates on the efficiency of dye-sensitized solar cells. *Applied physics letters*, *93*(13), 133311-133311.

22. An, J., Guo, W., & Ma, T. (2012). Enhanced Photoconversion Efficiency of All-Flexible Dye-Sensitized Solar Cells Based on a Ti Substrate with TiO_2 Nanoforest Underlayer. *Small*, *8*(22), 3427-3431.

23. Transparent, S. P. M. N. M. (2008). Electrodes Lee, Jung-Yong; Connor, Stephen T.; Cui, Yi; Peumans, Peter. *Nano Letters*, *8*(2), 689-692.

24. De, S., Higgins, T. M., Lyons, P. E., Doherty, E. M., Nirmalraj, P. N., Blau, W. J., ... & Coleman, J. N. (2009). Silver nanowire networks as flexible, transparent, conducting films: extremely high DC to optical conductivity ratios. *ACS nano*, *3*(7), 1767-1774.

25. Scardaci, V., Coull, R., Lyons, P. E., Rickard, D., & Coleman, J. N. (2011). Spray Deposition of Highly Transparent, Low-Resistance Networks of Silver Nanowires over Large Areas. *Small*, *7*(18), 2621-2628.

26. Leem, D. S., Edwards, A., Faist, M., Nelson, J., Bradley, D. D., & de Mello, J. C. (2011). Efficient organic solar cells with solution-processed silver nanowire electrodes. *Advanced Materials*, *23*(38), 4371-4375.

27. Wu, Z., Chen, Z., Du, X., Logan, J. M., Sippel, J., Nikolou, M., ... & Rinzler, A. G. (2004). Transparent, conductive carbon nanotube films. *Science*, *305*(5688), 1273-1276.

28. Dan, B., Irvin, G. C., & Pasquali, M. (2009). Continuous and scalable fabrication of transparent conducting carbon nanotube films. *ACS nano*, *3*(4), 835-843.

29. Becerril, H. A., Mao, J., Liu, Z., Stoltenberg, R. M., Bao, Z., & Chen, Y. (2008). Evaluation of solution-processed reduced graphene oxide films as transparent conductors. *ACS nano*, *2*(3), 463-470.

30. Wang, X., Zhi, L., & Müllen, K. (2008). Transparent, conductive graphene electrodes for dye-sensitized solar cells. *Nano letters*, *8*(1), 323-327.

31. Lipomi, D. J., & Bao, Z. (2011). Stretchable, elastic materials and devices for solar energy conversion. *Energy & Environmental Science*, *4*(9), 3314-3328.

32. Baca, A. J., Yu, K. J., Xiao, J., Wang, S., Yoon, J., Ryu, J. H., ... & Rogers, J. A. (2010). Compact monocrystalline silicon solar modules with high voltage outputs and mechanically flexible designs. *Energy & Environmental Science*, *3*(2), 208-211.

33. Yu, G., Gao, J., Hummelen, J. C., Wudl, F., & Heeger, A. J. (1995). Polymer photovoltaic cells: enhanced efficiencies via a network of internal donor-acceptor heterojunctions. *Science-AAAS-Weekly Paper Edition*, *270*(5243), 1789-1790.

34. O'regan, B., & Grätzel, M. (1991). A low-cost, high-efficiency solar cell based on dye-sensitized colloidal TiO_2 films.

35. http://www.dyesol.com[accessed on 9/4/2015].

36. http://www.g24i.com[accessed on 9/4/2015].

37. http://www.3gsolar.com[accessed on 9/4/2015].

38. Becquerel, A. E. (1839). On electric effects under the influence of solar radiation. *CR Acad. Sci*, *9*, 711-4.

39. Grätzel, M. (2009). Recent advances in sensitized mesoscopic solar cells. *Accounts of chemical research*, *42*(11), 1788-1798.

40. Rhee, S. W., & Kwon, W. (2011). Key technological elements in dye-sensitized solar cells (DSC). *Korean Journal of Chemical Engineering*, *28*(7), 1481-1494.

41. Grätzel, M. (2001). Photoelectrochemical cells. *Nature*, *414*(6861), 338-344.

42. Hagfeldt, A., & Grätzel, M. (2000). Molecular photovoltaics. *Accounts of Chemical Research*, *33*(5), 269-277.

43. Grätzel, M. (2005). Solar energy conversion by dye-sensitized photovoltaic cells. *Inorganic chemistry*, *44*(20), 6841-6851.

44. Grätzel, M. (2009). Recent advances in sensitized mesoscopic solar cells. *Accounts of chemical research*, *42*(11), 1788-1798.

45. Kroon, J. M., Bakker, N. J., Smit, H. J. P., Liska, P., Thampi, K. R., Wang, P., ... & Tulloch, G. E. (2007). Nanocrystalline dye-sensitized solar cells having maximum performance. *Progress in Photovoltaics: Research and Applications*, *15*(1), 1-18.

46. Kashiwa, Y., Yoshida, Y., & Hayase, S. (2008). All-metal-electrode-type dye sensitized solar cells (transparent conductive oxide-less dye sensitized solar cell) consisting of thick and porous Ti electrode with straight pores. *Applied Physics Letters*, *92*(3), 033308-033308.

47. Yoshida, Y., Pandey, S. S., Uzaki, K., Hayase, S., Kono, M., & Yamaguchi, Y. (2009). Transparent conductive oxide layer-less dye-sensitized solar cells consisting of floating electrode with gradient TiOx blocking layer. *Applied Physics Letters*, *94*(9), 093301.

48. Fuke, N., Fukui, A., Komiya, R., Islam, A., Chiba, Y., Yanagida, M., ... & Han, L. (2008). New approach to low-cost dye-sensitized solar cells with back contact electrodes. *Chemistry of Materials*, *20*(15), 4974-4979.

49. Beppu, T., Kashiwa, Y., Hayase, S., Kono, M., & Yamaguchi, Y. (2009). Transparent conductive oxide layer-less three dimensional dye sensitized solar cells: fabrication of ionic path in three dimensional Ti electrode. *Japanese Journal of Applied Physics*, *48*(6R), 061504.

50. http://www.alt-energy.info/solar-power/solyndra-generating-buzz-with-its-cylindrical-solar-cells/ [accessed on 03/04/2015]

51. http://www.nbcbayarea.com/news/local/Solyndra-Shutting-Down-128802718.html [accessed on 03/04/2015]

52. Tachan, Z., Rühle, S., & Zaban, A. (2010). Dye-sensitized solar tubes: a new solar cell design for efficient current collection and improved cell sealing. *Solar Energy Materials and Solar Cells*, *94*(2), 317-322.

53. Fan, X., Chu, Z. Z., Wang, F. Z., Zhang, C., Chen, L., Tang, Y. W., & Zou, D. C. (2008). Wire-shaped flexible dye-sensitized solar cells. *Advanced Materials*, *20*(3), 592-595.

54. Huang, S., Guo, X., Huang, X., Zhang, Q., Sun, H., Li, D., ... & Meng, Q. (2011). Highly efficient fibrous dye-sensitized solar cells based on TiO_2 nanotube arrays. *Nanotechnology*, *22*(31), 315402.

55. Lv, Z., Fu, Y., Hou, S., Wang, D., Wu, H., Zhang, C., ... & Zou, D. (2011). Large size, high efficiency fiber-shaped dye-sensitized solar cells. *Physical Chemistry Chemical Physics*, *13*(21), 10076-10083.

56. Zhang, S., Ji, C., Bian, Z., Liu, R., Xia, X., Yun, D., ... & Cao, A. (2011). Single-wire dye-sensitized solar cells wrapped by carbon nanotube film electrodes. *Nano letters*, *11*(8), 3383-3387.

57. Liu, Y., Li, M., Wang, H., Zheng, J., Xu, H., Ye, Q., & Shen, H. (2010). Synthesis of TiO_2 nanotube arrays and its application in mini-3D dye-sensitized solar cells. *Journal of Physics D: Applied Physics*, *43*(20), 205103.

58. Wang, Y., Liu, Y., Yang, H., Wang, H., Shen, H., Li, M., & Yan, J. (2010). An investigation of DNA-like structured dye-sensitized solar cells. *Current Applied Physics*, *10*(1), 119-123.

59. Usagawa, J., Pandey, S. S., Ogomi, Y., Noguchi, S., Yamaguchi, Y., & Hayase, S. (2013). Transparent conductive oxide-less three-dimensional cylindrical dye-sensitized solar cell fabricated with flexible metal mesh electrode. *Progress in Photovoltaics: Research and Applications*, *21*(4), 517-524.

60. Usagawa, J., Kogo, T., Sadamasu, K., Pandey, S. S., Ogomi, Y., & Hayase, S. (2012). Flexible transparent conductive oxide-less flat and cylinder dye-sensitized solar cells. *Journal of Photonics for Energy*, *2*(1), 021011-1.

61. Sun, L., Zhang, S., & Wang, Q. (2014). Conformal Growth of Anodic Nanotubes for Dye-Sensitized Solar Cells: Part II. Nonplanar Electrode. *Journal of nanoscience and nanotechnology*, *14*(2), 2050-2064.

62. Jessensky, O., Müller, F., & Gösele, U. (1998). Self-organized formation of hexagonal pore arrays in anodic alumina. *Applied Physics Letters*, *72*(10), 1173-1175.

63. Houser, J. E., & Hebert, K. R. (2009). The role of viscous flow of oxide in the growth of self-ordered porous anodic alumina films. *Nature materials*, *8*(5), 415-420.

64. Yasuda, K., Macak, J. M., Berger, S., Ghicov, A., & Schmuki, P. (2007). Mechanistic aspects of the self-organization process for oxide nanotube formation on valve metals. *Journal of the electrochemical society*, *154*(9), C472-C478.

65. Berger, S., Jakubka, F., & Schmuki, P. (2008). Formation of hexagonally ordered nanoporous anodic zirconia. *Electrochemistry Communications*, *10*(12), 1916-1919.

66. LeClere, D. J., Velota, A., Skeldon, P., Thompson, G. E., Berger, S., Kunze, J., ... & Nagata, S. (2008). Tracer investigation of pore formation in anodic titania. *Journal of the Electrochemical Society*, *155*(9), C487-C494.

67. Liu, Y., Wang, H., Shen, H., & Chen, W. (2010). The 3-dimensional dye-sensitized solar cell and module based on all titanium substrates. *Applied Energy*, *87*(2), 436-441.

68. Wang, Y., Yang, H., & Lu, L. (2010). Three-dimensional double deck mesh like dye-sensitized solar cells. *Journal of applied physics*, *108*(6), 064510.

69. Liu, Z., Subramania, V., & Misra, M. (2009). Vertically oriented TiO_2 nanotube arrays grown on Ti meshes for flexible dye-sensitized solar cells. *The Journal of Physical Chemistry C*, *113*(31), 14028-14033.

70. Rustomji, C. S., Frandsen, C. J., Jin, S., & Tauber, M. J. (2010). Dye-Sensitized Solar Cell Constructed with Titanium Mesh and 3-D Array of TiO_2 Nanotubes†. *The Journal of Physical Chemistry B*, *114*(45), 14537-14543.

71. Greijer, H., Karlson, L., Lindquist, S. E., & Hagfeldt, A. (2001). Environmental aspects of electricity generation from a nanocrystalline dye sensitized solar cell system. *Renewable Energy*, *23*(1), 27-39.

72. Ramier, J., Plummer, C. J. G., Leterrier, Y., Månson, J. A., Eckert, B., & Gaudiana, R. (2008). Mechanical integrity of dye-sensitized photovoltaic fibers.*Renewable Energy*, *33*(2), 314-319.

73. Ramier, J., Da Costa, N., Plummer, C. J. G., Leterrier, Y., Månson, J. A., Eckert, R., & Gaudiana, R. (2008). Cohesion and adhesion of nanoporous TiO_2 coatings on titanium wires for photovoltaic applications. *Thin Solid Films*, *516*(8), 1913-1919.

74. Liu, H., Wang, D., Ji, L., Li, J., Liu, S., Liu, X., & Jiang, S. (2010). A novel TiO_2 nanotube array/Ti wire incorporated solid-phase microextraction fiber with high strength, efficiency and selectivity. *Journal of Chromatography A*, *1217*(12), 1898-1903.

75. Wang, H., Liu, Y., Huang, H., Zhong, M., Shen, H., Wang, Y., & Yang, H. (2009). Low resistance dye-sensitized solar cells based on all-titanium substrates using wires and sheets. *Applied Surface Science*, *255*(22), 9020-9025.

76. Cai, X., Lv, Z., Wu, H., Hou, S., & Zou, D. (2012). Direct application of commercial fountain pen ink to efficient dye-sensitized solar cells. *Journal of Materials Chemistry*, *22*(19), 9639-9644.

77. Yang, Z., Sun, H., Chen, T., Qiu, L., Luo, Y., & Peng, H. (2013). Photovoltaic wire derived from a graphene composite fiber achieving an 8.45% energy conversion efficiency. *Angewandte Chemie*, *125*(29), 7693-7696.

78. Zhang, S., Ji, C., Bian, Z., Yu, P., Zhang, L., Liu, D., & Cao, A. (2012). Porous, platinum nanoparticle-adsorbed carbon nanotube yarns for efficient fiber solar cells. *ACS nano*, *6*(8), 7191-7198.

79. Sun, M., & Cui, X. (2013). Needle-shaped 3D dye-sensitized solar cells using anodized Ti wire and Pt nanoparticle/carbon fiber electrodes. *Journal of Power Sources*, *223*, 74-78.

80. Fu, Y., Lv, Z., Hou, S., Wu, H., Wang, D., Zhang, C., & Zou, D. (2011). Conjunction of fiber solar cells with groovy micro-reflectors as highly efficient energy harvesters. *Energy & Environmental Science*, *4*(9), 3379-3383.

81. Ramier, J., Plummer, C. J. G., Leterrier, Y., Månson, J. A., Eckert, B., & Gaudiana, R. (2008). Mechanical integrity of dye-sensitized photovoltaic fibers. *Renewable Energy*, *33*(2), 314-319.

CHAPTER 2: INSTRUMENTATION & CHARACTERIZATION

2.1 Characterization of solar cells

Typically solar cells are characterized by the output photovoltage V and current I when illuminated with a spectral distribution at a certain temperature. Solar cells work like a battery when connected across the load as shown in Figure 1. When it is kept under the dark condition, there is no current flow in the circuit. When it is irradiated by the light it develops a voltage, or electromotive force (e.m.f.), analogous to the e.m.f of the battery in the circuit. The voltage is developed when there is infinite resistance connected across the load terminals, known as *open circuit voltage* V_{oc}. The current drawn when there is zero resistance or the end terminals are connected directly, known as *short circuit current* I_{sc}. For any other resistance R_L in between zero and infinite resistance the solar cell develops a voltage $V=IR_L$, where I is the current flowing in the circuit. The current generated due to illumination of the solar cell is approximately proportional to the active area, in that case *short circuit current density* J_{sc} is useful parameter.

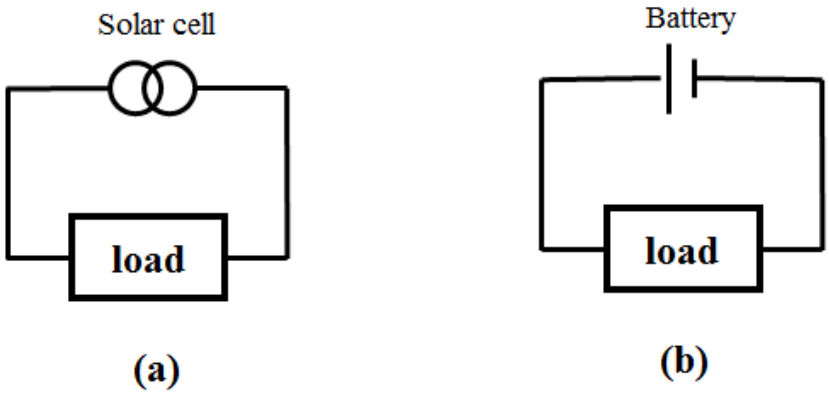

Figure 1. Solar cell can be in place of battery

One can argue that how solar cell is different from conventional battery? The e.m.f of the battery is due to permanent electrochemical potential difference between the two phases in the cell, while in case of the solar cell e.m.f generated is from temporary change in electrochemical potential caused by irradiation. Therefore, the output power delivered by the solar cell will be variable depending upon the incident light intensity. Whereas in case of the battery the output power generated is almost constant. Another difference is the life time, in case of battery it stops working

when it is completely discharged. But in case of solar cell, in principle it can never exhaust, because it can be continuously recharged with light. Electrically the battery is modelled as a *voltage source* [1] whereas solar cell is better modelled as a *current source* [2].

2.1.1 Current voltage measurements under standard test conditions

The Standard Test Conditions (STC) are used for the performance evaluation of the solar cells. The result of this test gives the electrical output of the solar cells. These conditions are fixed and are as follows,

- Cell temperature should be at 25^0C
- Spectral irradiation is 100 mW/cm^2
- Spectral energy distribution is according to Air Mass (AM) 1.5

As it shows the performance of the solar cell is dependent on temperature, irradiation intensity and spectral distribution of the light source, therefore, the same solar cell shows different performance under other conditions. In the present work, the photovoltaic measurements were carried out using solar simulator (KHP-1, Bunko-Keiki, Japan) equipped with a xenon lamp (XLS-150A) with the irradiation power of 100 mW/cm^2. The solar simulator spectrum and its power were adjusted using a spectroradiometer (LS-100, Eiko Seiki, Japan). The power of the incident light was also corrected using standard amorphous Si photo detector (BS- 520 S/N 007, Bunko-Keiki, Japan).

What is Air Mass (AM) 1.5?

Solar spectrum consists of wide range of electromagnetic radiations varying from ultraviolet, visible to infrared. When it travels through the atmosphere of earth its composition changes because of the presence of O_2, H_2O and CO_2. The different radiations thus transmitted depends on the angle and length by which sunlight

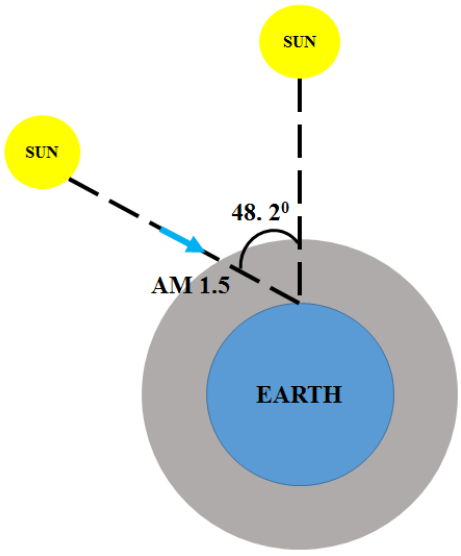

Figure 2. Schematic showing condition for AM 1.5.

passes through the atmosphere. The standard AM 1.5 spectrum is the solar spectrum at an incidence angle of 48.2^0 from zenith (*i.e.* when sun is directly overhead) as shown in Figure 2.

2.1.2 Short circuit current density (J_{sc}) and Incident photon to current conversion efficiency:

Short circuit current density is the largest current that can be drawn from a given solar cell. It depends on the incident light spectrum and some other factors as expressed by the following equation,

$$Jsc = \int q\, F(E)\, IPCE(E) dE, \ldots\ldots\ldots\ldots\ldots\ldots (1)$$

Where q is the electronic charge, F(*E*) is the incident photon flux density defined as the number of photons of energy in the range E to E+dE incident on unit area in unit time. Incident photon to current conversion efficiency (IPCE) is the quantum efficiency which is defined as the probability that an incident photon of energy E will deliver how much electron to the external circuit. Its value equal to 1.0 (100 %) represents that one photon striking on the surface of solar cell is capable to deliver one electron to the external circuit. IPCE depends on the absorption coefficient of the solar cell material, the efficiency of charge separation and the charge collection but does not depend on incident spectrum. Therefore, IPCE is an important quantity in describing solar cell performance

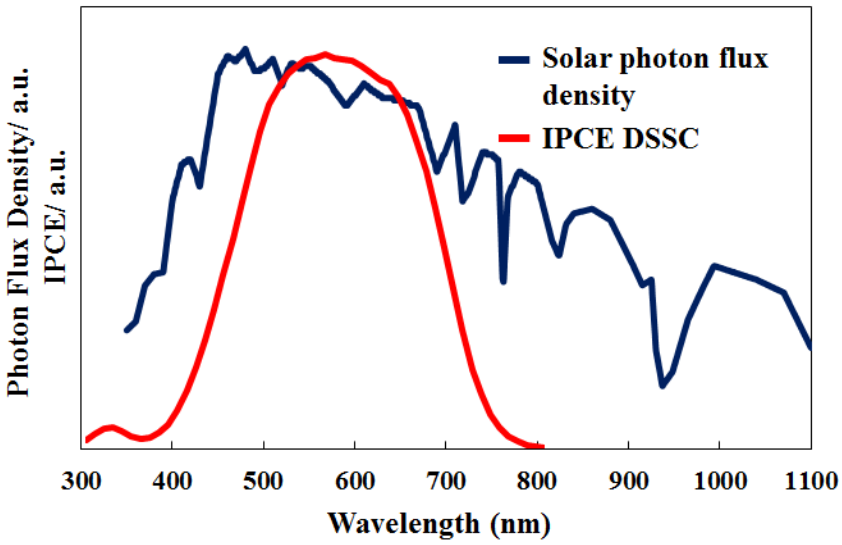

Figure 3. IPCE of DSSC using N719 dye and iodine based electrolyte is compared to the solar spectrum. The Jsc can be obtained by integrating the product of the photon flux density and IPCE over photon energy. It is desirable to have high and broader IPCE for high Jsc

under different conditions. Figure 3 shows typical IPCE along with 1 SUN spectral irradiation. Plot of IPCE as function of the wavelength is also known as photocurrent action spectrum and represents the extent of photon harvesting along with the photon harvesting window. IPCE can be expressed either as a function of photon energy or wavelength, λ. Energy (E) and wavelength (λ) can be related as,

$$E=hc/\lambda \quad \ldots\ldots\ldots\ldots\ldots (2)$$

Where, *h* is Planck's constant and *c* the speed of light in vacuum.

2.1.3 Dark current and Current- Voltage Characteristics

The current which flows in the solar cell in absence of light is known as dark current. In conventional solar cells as well as DSSCs too, it provides quantitative information about the recombination processes [3]. In the case of DSSC, the recombination involved are transfer of photogenerated electrons from TiO_2 surface to the redox electrolyte or to the HOMO of the oxidized dye. Although the processes involved are totally different, however, in both of the cases, lower the dark current higher will be the photocurrent. Therefore, in case of DSSC also the dark current characteristic can be modelled as in case of conventional solar cells. Solar cells behave like a diode in the dark, allowing large current to flow under forward bias (V>0) than compared to that under reversed bias (V<0). This feature of photovoltaic devices is also termed as rectifying behavior. It is expressed as follows,

$$I_{dark}(V) = Io\left\{exp\left(q\frac{V}{nkT}\right) - 1\right\} \quad \ldots\ldots\ldots\ldots\ldots (3)$$

Where Io is a constant associated with reverse saturation current, n is ideality factor, k is Boltzmann's constant and T is temperature in degrees Kelvin. Ideality factor is an important parameters for diodes and defines the quality of diode. This is the reason, it is also known as diode quality factor also.

Equivalent Circuit of DSSCs. The equivalent electrical model for the DSSC is shown in the Figure 4. It consists of a current source, a diode, capacitances, and the resistances. I_p is the photocurrent generated by the solar cell and modelled as current source. It is proportional to the irradiation intensity of the sunlight. The C_{Pt} and R_{Pt} are collectively the impedance to the charge transport on

the surface of the counter electrode. The C_{Elec} and R_{Elec} are the impedance to carrier transport through the ions in the electrolyte or in other words these are the electron transfer resistance of TiO_2/dye/electrolyte interfaces. R_W is basically the sheet resistance associated with the working electrode. R_{SH} represents the shunt resistance, which is generally the resistance associated with the back electron transfer, also known as recombination resistance. Higher value of this resistance is preferable for the better performance of the solar cells. Therefore eq. 3 can be written in modified form as,

$$I_{dark} = Io\left\{exp\left(q\frac{V+IRs}{nkT}\right) - 1\right\} \ldots\ldots\ldots\ldots\ldots (4)$$

Where R_s net series resistance which is given as, $R_{Pt} + R_{Elec} + R_W$

I_{SH} is the current flowing through shunt resistance R_{SH}. For better performance of the solar cell, this current should be low. It is given as

$$I_{SH} = \frac{V+IR_S}{R_{SH}} \ldots\ldots\ldots\ldots\ldots\ldots\ldots (5)$$

Therefore, net output current I_{net} can be given as [4-6],

$$I_{net} = I_P - \frac{V+IR_S}{R_{SH}} - Io\left\{exp\left(q\frac{V+IRs}{nkT}\right) - 1\right\} \ldots\ldots\ldots\ldots (6)$$

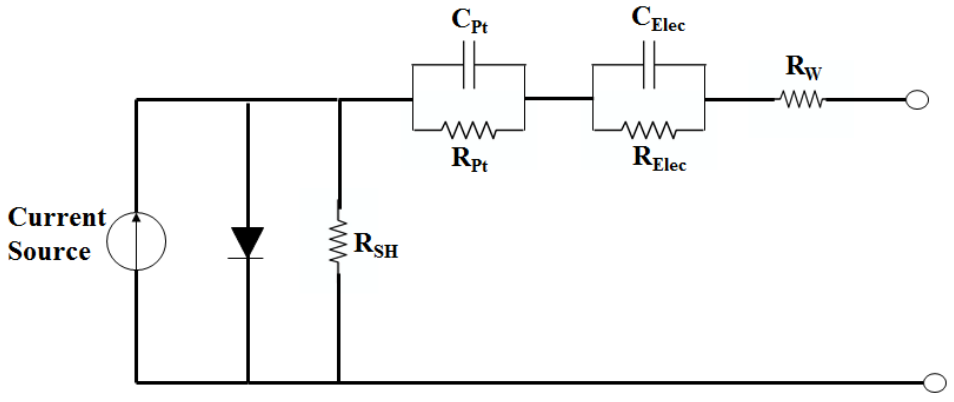

Figure 4. Equivalent circuit diagram for DSSC

2.1.4 Open Circuit Voltage (Voc)

This is the condition of a solar cell when there is no net current flow in the external circuit even under illumination by the light source. It is due to the high load resistance across the terminals of the solar cell. Thus the voltage developed across the load resistance is the open circuit voltage (Voc). In case of the DSSC, it is given by the difference in Fermi energy level of the TiO_2 (n-type) and the energy level of the redox electrolyte or HOMO energy level p-type hole conductor as shown in Figure 5. Basically this is the driving force for the net charge transfer inside the DSSC. In broader sense it varies with several other factors. The general expression for Voc can be given as [7]

$$V_{OC} = \left(\frac{kT}{e}\right) \ln\left(\frac{I_P}{n\, k_c}\right) \ldots\ldots\ldots\ldots\ldots (7)$$

Where I_p is the photocurrent injected into the conduction band of TiO_2, n is the photoelectron density in the conduction band of TiO_2 and k_C is rate constant of back electron transfer reaction from surface of TiO_2 with the redox electrolyte. Therefore, Voc will be higher for higher value of the photocurrent generated. Also, if recombination rate increases the Voc decreases accordingly. The recombination rate further depends on the various other factors such as the thickness of the TiO_2 layer [8] etc.

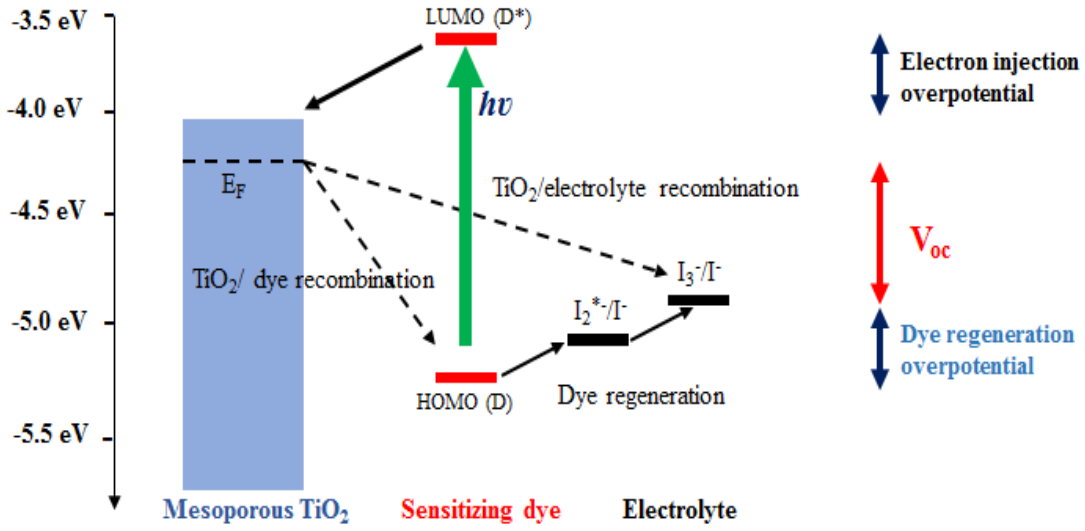

Figure 5. Energy band diagram for DSSC, redrawn from Chapter 1

2.1.5 Photoconversion Efficiency (PCE)

The range in which the solar cell delivers power to the external circuit is from 0 to Voc. The solar cell *power density, P* is given as,

$$P = \text{JV} \quad \text{..... (8)}$$

The point where value of *P* reaches maximum, is known as *maximum power point*. This value is obtained at voltage Vm and the corresponding current density Jm as shown in Figure 6. At this point thus resistance of the load would be Vm/Jm. Also, at this point one very important term for the solar cells can be defined, known as *fill factor* (FF). It is expressed as follows,

$$\text{FF} = \frac{Jm\,Vm}{Jsc\,Voc} \quad \text{..... (9)}$$

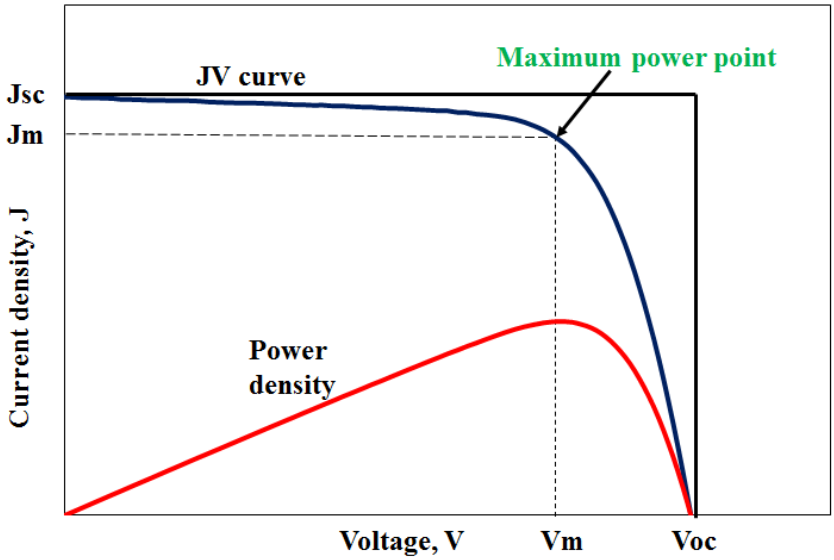

Figure 6. The current voltage (blue) and power-voltage (red) characteristics of a typical solar cell. The maximum output power is given by Jm*Vm, inner rectangle area. The outer rectangle area is Jsc*Voc. For maximum FF=1, the current-voltage curve follows outer rectangle.

The FF defines the 'square-ness' of the J-V curve. The *efficiency* η of the solar cell is the ratio of the maximum power density obtained from the solar cell (*i.e.* maximum power point) to the incident power density, P*i* as

$$\eta = \frac{JmVm}{Pi} \quad \text{..... (10)}$$

Efficiency can further be written in form of Jsc, Voc & FF as,

$$\eta = \frac{Jsc\ Voc\ FF}{Pi} \quad \text{.....(11)}$$

All these parameters, Jsc, Voc, FF and η are important for characterizing the solar cell. All of these are defined for particular conditions. Some of the recent results for different type of solar cells are listed in the Table 1 [9].

Table1. Performance of some PV cells under 1 SUN condition

Classification	Efficiency(η %)	Area (cm^2)	Voc (V)	Jsc (mA/cm^2)	FF (%)
Si (crystalline)	25.6 ± 0.5	143.7 (da)	0.740	41.8	82.7
GaAs (thin film)	28.8 ± 0.9	0.9927 (ap)	1.122	29.68	86.5
Si (multicrystalline)	20.8 ± 0.6	243.9 (ap)	0.6626	39.03	80.3
Perovskite (thin films)	20.1 ± 0.4	0.0955 (ap)	1.059	24.65	77.0
DSSC	11.9 ± 0.4	1.005 (da)	0.744	22.47	71.2

*ap = aperture area, *da = designated illumination area

2.1.6 Electrochemical impedance spectroscopy

Electrochemical impedance spectroscopy (EIS) is a method popularly used in electrochemistry for investigating the interfacial charge transfer between a solid electrode (as working electrode) and an electrolyte. A voltage is applied between working electrode (WE) and counter electrode (CE) with the assistance of the reference electrode (RE). The electrolyte provides the large conductivity and totally independent of drift phenomenon as in solid materials. Therefore, electrochemistry involves interfacial charge transfers mainly due to diffusion of reactants or products. With EIS, it is possible to study interfacial capacitance & charge-transfer resistance separately [10]. Impedance spectroscopy technique is popularly used in different classes of materials and devices. It is basically the frequency analysis of ac behavior of the materials such as inorganic, organic and biological. Generally in case of the solid state PV cells admittance spectroscopy is used.

Admittance is the reciprocal of impedance, therefore, almost same information can be drawn. Traditionally admittance spectroscopy consists of applying a reverse voltage and evaluating the energy levels of the trapped carriers or trap densities of states [11]. However, in case of photoelectrochemical systems EIS had been used [12, 13] since long time back. DSSCs are also a kind of photoelectrochemical systems and EIS can be used for getting information about electronic carrier concentration on the surface via Mott-Schottky plots and also about rates of interfacial charge transfer [14, 16]. In the case of solar cells, it is of great interest to know the mechanisms responsible for the photovoltaic performance between short-circuit and open-circuit condition (basically in forward bias directions, where energy extraction from the solar cell takes place). Therefore, exploring this region both in dark and under illumination with different light intensities, a variety of properties such as transport in the photoactive layer, contact, bulk and surface capacitance *etc.* can be studied.

This method has been used in past few years for studying amorphous Si solar cell [17-19], thin film CdTe/CdS [20], GaAs/Ge [21, 22] and CdS/CIGS solar cells [23]. Similar approach has been also been used for the next generation solar cells like DSSCs [24-30] and organic solar cells [31, 32]. In the present work, EIS measurements were carried out using electrochemical interface (solartron 1287) and frequency response analyzer (solartron 1255B) connected to solar simulator (Yamashita Denso YSS 50A). The measurement was performed in the frequency range of 10^{-3}–10^{5} Hz at room temperature. Impedance spectra were measured by applying a DC bias at constant current of 1 mA cm^{-2} and AC voltage with an amplitude of 10 mV. Z-View software (Solartron Analytical) was utilized for analysis of the EIS. Nyquist plot are basically representing the frequency response a system and displays the both of amplitude and phase angle in a single plot. A typical Nyquist plot for conventional DSSC is shown in Figure 7. It contains three semicircles in the order of decreasing frequency from left to right of the plot. The first semi-circle is the high frequency region. This corresponds to the resistance for the redox reaction at the counter electrode. Second in the mid frequency region corresponds to the resistance associated with TiO_2/dye/electrolyte interface. The final and third semicircle which falls in low frequency region is attributed to the diffusion resistance within electrolyte [33].

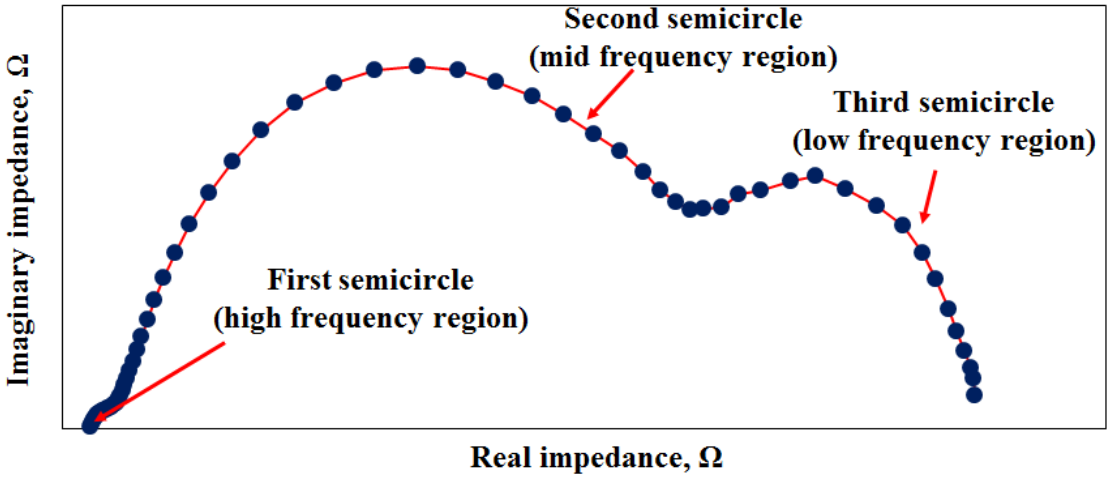

Figure 7. Typical Nyquist plot for the conventional DSSC

2.2 Characterization methods used to analyze photoanode

The worldwide research interest in one-dimensional nanostructures have been generated since the discovery of carbon nanotubes [34]. Since after that many diverse materials and nanostructures has been explored and studied for their physical and chemical properties. The physical and chemical properties of nanostructures are affected not only by the intrinsic electronic properties but the factors such as size, shape and surface properties too. Interesting morphologies such as nanotubes, nanorods, nanofibers and nanosheets have been explored in diverse area of applications. Sodium titanate nanotubes has been used for biological applications [35], $Na_2Ti_3O_7$ whiskers for photocatalysis [36], TiO_2 nanowire arrays for photoelectrochemical application [37], TiO_2 nanotube arrays implemented for diverse applications such as solid-phase microextraction [38], quantum dot photovoltaics [39], and supercapacitors [40]. TiO_2 nanostructures has been studied intensively because of its semiconducting and functional features.

Amongst the many semiconductor metal oxides, TiO_2 is distinguished candidate because of its high chemical and optical stability, nontoxicity, low cost, and corrosion resistance. DSSCs use nanoporous TiO_2 adsorbed with monolayer of sensitizing dye molecules to work as photoanode [41]. Nanostructures based on TiO_2 can be grown on various substrates using different methods such as $TiCl_4$ treatment [42], water-soaking treatment [43], hydrothermal treatment [44], *etc*. TiO_2 is widely popular in various applications due to its three main phases of rutile, anatase and brookite [45]. The anatase phase is preferred over other polymorphs for the solar cell applications because

of low recombination of electron-hole pairs and high conduction band edge energy [46]. Therefore, to characterize the TiO_2 phases and to understand the effect of these phases on applications such as solar cells, one need have the characterizing tools such as X-ray diffraction (XRD), X-ray photoelectron spectroscopy (XPS), *etc*. In the present work, we have used some of these techniques for characterization of anatase phase of TiO_2 on the metallic Ti substrates which we used to fabricate the photoanodes. Therefore, below I would like to give a brief discussion about the methods and the principle involved in the techniques, and their use for characterizing our devices.

2.2.1 X-ray diffraction (XRD) analysis

When electromagnetic rays are allowed to fall on the surface of a material, some of its part will be reflected so that the angle of incidence is equal to the angle of reflection. In case of the crystalline materials, constructive and destructive interference between the rays reflected from the consecutive crystal planes will occur. The interference occurs when the incident rays have wavelength (λ) comparable to the spacing (2-3 A^0) between the crystal planes. The condition for the constructive interference to occur is given by *Bragg's law:*

$$n\lambda = 2d_{hkl} \sin\theta \quad \text{.....eq (12)}$$

where, θ is the angle of incidence measured from the plane of reflection as shown in Figure 8(a), d_{hkl} is the inter-planar spacing and n is the *order of reflection*. X-rays are generated when electrons moving at very high speeds directed to a metal target. These X-rays thus generated are of two types, one is known as *white radiation* and another is *characteristic radiation*. The characteristic radiations are used for generating the diffraction patterns and are denoted as K_α, K_β, L_α, etc. K_α radiation has the highest intensity and commonly used in diffraction studies. Table 2 shows the wavelengths of K_α radiation of some target metals. If we go in more depth of the phenomenon involved, basically the X-rays are scattered when they interact with atomic electrons and interference takes place between X-rays scattered from different part of the atom.

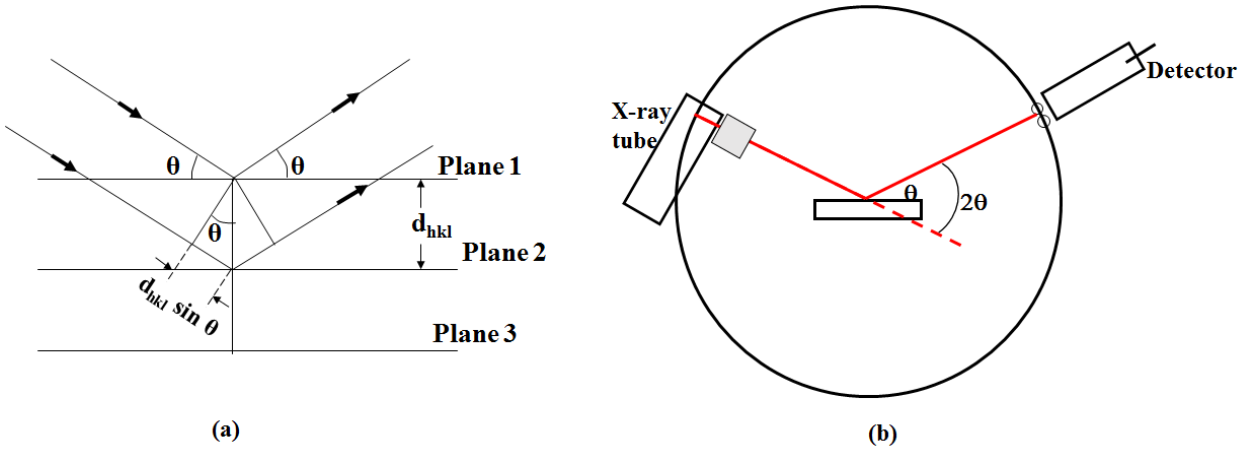

Figure 8. (a) Diagram showing reflection from parallel planes (b) Typical XRD measurement setup.

Table 2. Typical Kα value for different metal targets.

Target metal	**Mo**	**Cu**	**Co**	**Fe**	**Cr**
K_α Wavelength, A^0	0.71	1.54	1.79	1.94	2.29
nm	0.071	0.154	0.179	0.194	0.229

The intensity I_{hkl} of the resulting radiation after scattering from a set of planes $\{hkl\}$ can be written as

$$I_{hkl} \propto F^2_{\text{hkl}} \quad \text{..... (13)}$$

Where, F_{hkl} is the *structure factor* and it depends on the constituent atoms and their scattering factors. The crystal structure determination is often time consuming and needs a lot of patience. At first, macroscopic symmetry of the crystal is determined, then the space lattice and its dimensions and finally the atomic arrangement within the unit cell. A typical XRD analysis involve the plot of reflected intensity vs 2θ as shown in Figure 9, which is recorded from a diffractometer.

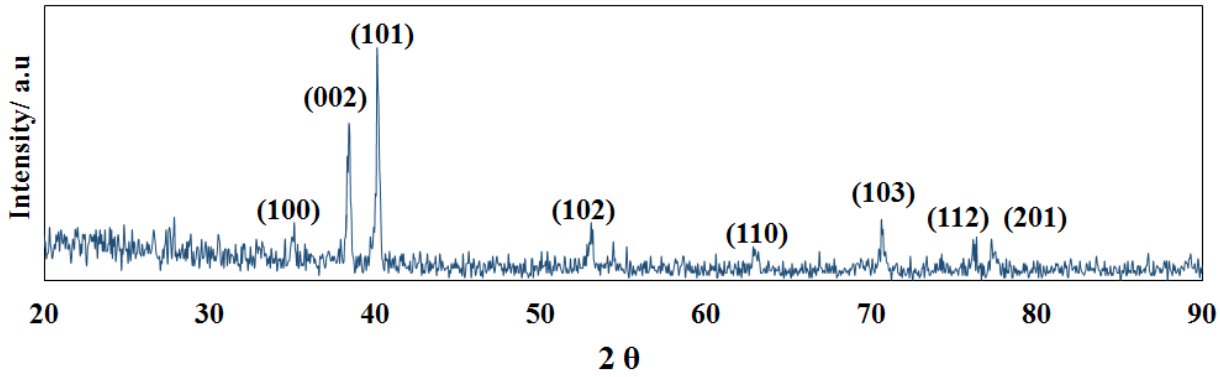

Figure 9. Typical XRD pattern obtained for α-Ti

The data thus obtained is compared with Joint committee on Powder Diffraction Standards (JCPDS) data files provided by International Center for Diffraction Data (ICDD). In the present work we have used Ti wires wrapped around the slide glass as shown in Figure 10 for doing the XRD analysis of the wire surfaces. Ti crystal have different phases named as α, β, ω, δ, and γ [47]. Commercially available Ti exists in the alloy form containing mainly two phases known as α phase (hexagonal closed pack) and β phase (body centered cubic) because they are stable phase of Ti while other phases are metastable. In case of pure Ti, α phase exists at room temperature and up to 882.3 ^{0}C, however, above this temperature it transforms to β phase. However, in case of different grades of Ti alloys both may exist together [48]. A typical XRD pattern obtained for α-Ti is shown in Figure 9, the peaks were matched using (JCPDS No. 44-1294) [49]. We have taken different diameter Ti wires and their surface was modified further using chemical treatments. The discussion on XRD patterns of each will be done in detail in the Chapter 4.

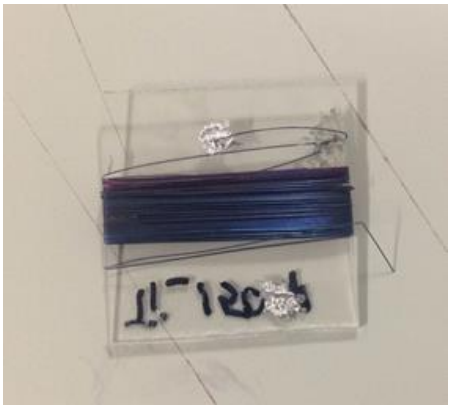

Figure 10. Ti wire sample used for XRD analysis

2.2.2 X-ray Photoelectron Spectroscopy (XPS)

X-ray photoelectron spectroscopy (XPS) is a surface analytical technique which provides qualitative and quantitative information about the electronic structure and/or chemical composition of the various materials. It is also known as electron spectroscopy for chemical analysis (ESCA). Here we have used the electromagnetic radiation to determine the ionization potential or work function of the material. Usually the X-rays (Mg Kα and Al Kα, with energy 1253.6 eV and 1486.6 eV, respectively) are used to emit the electrons from the core energy levels. As we know that these electrons are held by nucleus, therefore, certain amount of energy from X-ray will be required to take out the electron. When this electron will be released and the extra energy will come out in it as kinetic energy as shown in Figure 11. In the case of semiconductor and metals the *Fermi level*

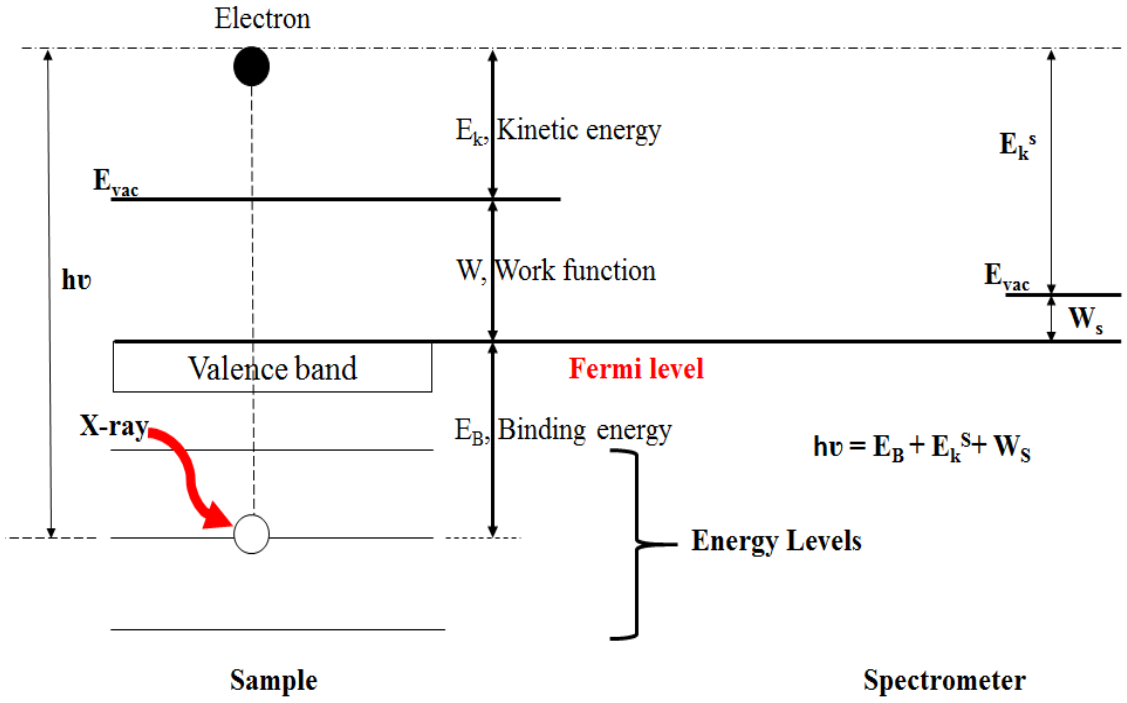

Figure 11. Basic principle for X-ray photoelectron spectroscopy

of the sample and the spectrometer are aligned or in other words both sample and spectrometer is grounded. Since, spectrometer and sample will surely have different work function as shown in the Figure 11, and here the work function of the spectrometer should be known accurately.

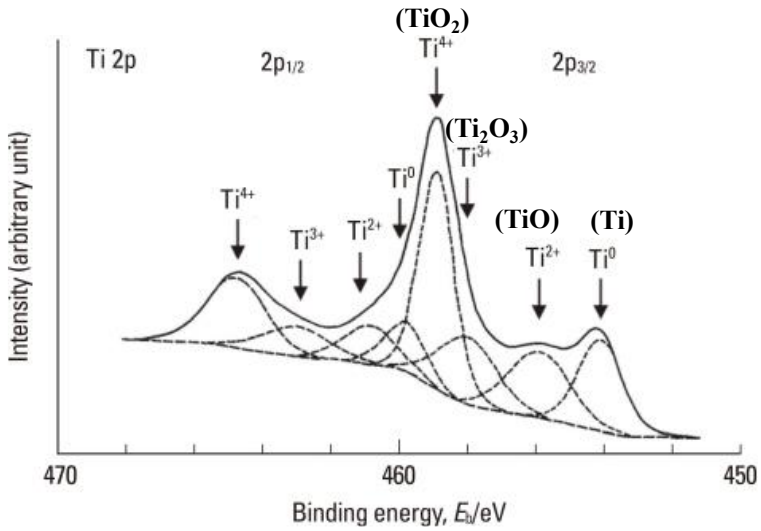

Figure 12. Typical XPS spectra for Ti 2p energy level for different Titanium valences. Right hand side figure denotes Ti wire sample arrangement used for XPS analysis in our experiments

The spectrometers are calibrated with standard samples before the photoemission and its work function can be determined. Hence, the binding energy vs intensity graph for the unknown sample can be plotted, which is a typical XPS analysis result as shown in Figure 12 [50].

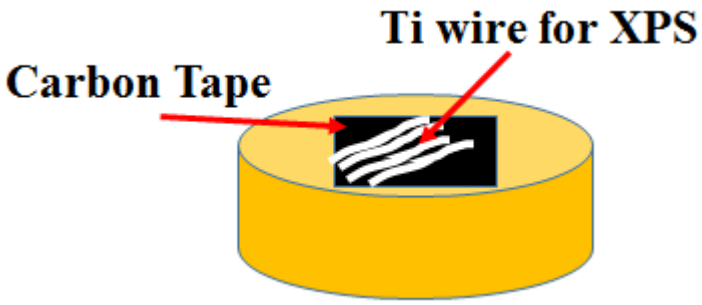

Figure 13. Ti wire sample arrangement used for XPS analysis in our experiments

2.2.3 Scanning Electron Microscopy (SEM)

Electron microscopy uses the focused beam of electrons accelerated through a potential and generated by thermionic emission from a metal filament. For example, an accelerating voltage of 100 kV will produce electron wavelength of $3.7 * 10^{-3}$ nm. When this beam of electrons is incident

on the material surface either they are diffracted, remain un-scattered or they will eject secondary electrons from the surface after interaction as shown in Figure 14 (a).

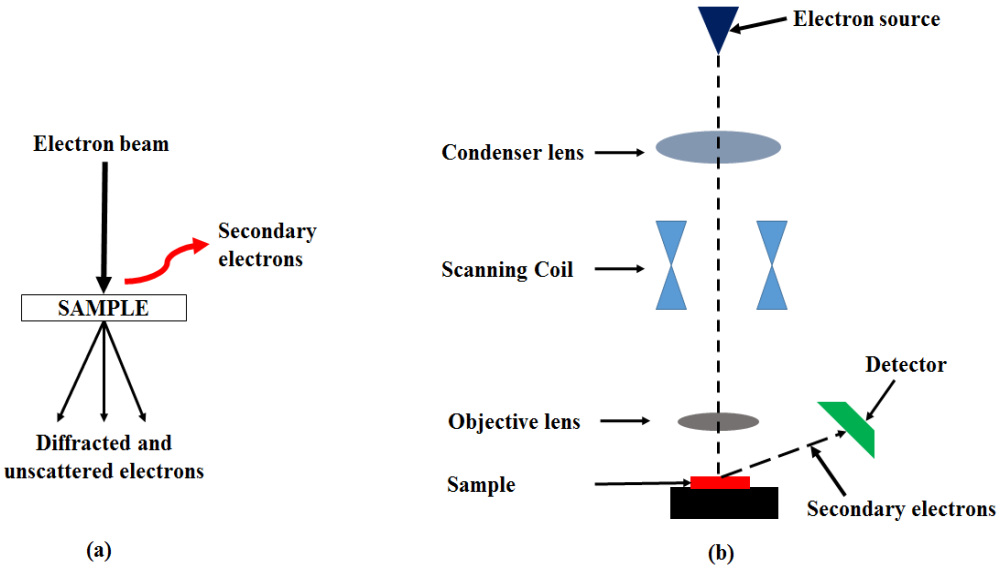

Figure 14 (a) Interactions involved and (b) approximate experimental setup for SEM

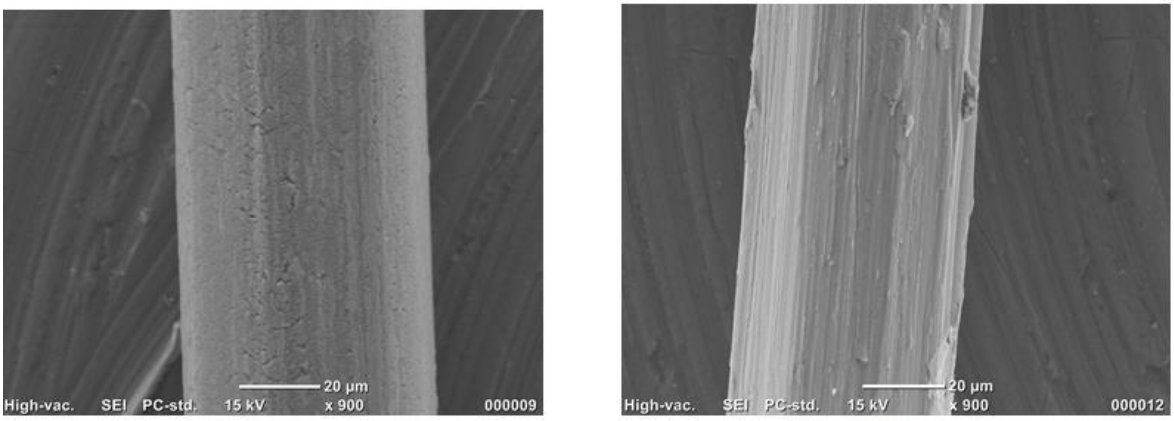

Figure 15. SEM image of Ti wire surface before polishing (a) and Ti wire surface after polishing (b)

The diffracted and un-scattered electrons are used in X-ray diffraction (XRD) study and Transmission electron microscopy (TEM) analysis for imaging. The low-energy (<50 eV) secondary electrons emitted are used for *scanning electron microscopy* (SEM). The schematic diagram of a typical SEM experiment-setup is shown in Figure 14(b). Electron beams are

condensed by condenser before focusing to a very fine point onto the sample using objective lens. The electron beams are scanned in a raster fashion across the sample using the scanning coils (generating magnetic fields). Secondary electrons thus emitted from the surface are detected and image of the material surface is predicted by the variable intensity of these secondary electrons. In the present work we have used SEM and FESEM (Field emission SEM) for analyzing the wire surfaces under investigation. Figure 15 shows the SEM image obtained for Ti wire before and after polishing of the surface. SEM is popularly used for measuring the thickness of the various layers of thin films [51]. We have also used SEM to see the thickness of TiO_2 coated in case of our devices fabricated. The images are shown in experimental section of Chapter 3 and Chapter 4.

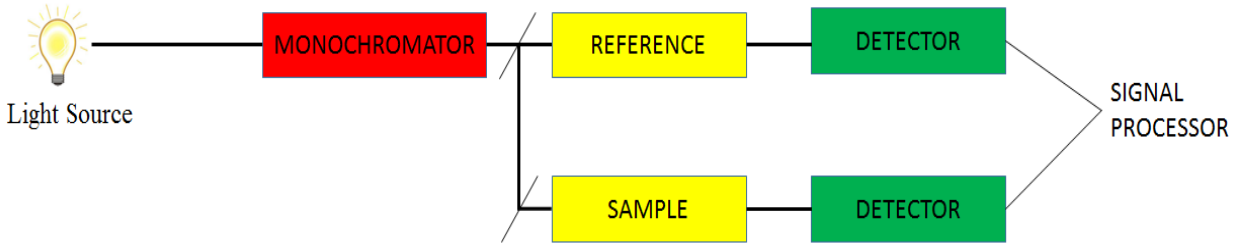

Figure 16. Block diagram showing instrumentation for UV-vis spectroscopy

2.2.4 Ultraviolet-visible (UV-vis) spectroscopy

It refers to the use of ultraviolet (UV) and visible region of the electromagnetic radiations for getting the absorption and reflection properties of different materials such as transition metal ions, highly conjugated organic compounds, *etc*. The UV radiation ranges from 10 nm to 400 nm and visible radiation ranges from 400 nm to 760 nm. Generally UV region used for analysis is above 200 nm. This spectroscopy is routinely being used in analytical chemistry. However, solid and gases may also be studied. The common instrumentation used for UV-Vis spectroscopy is drawn in Figure 16. It involves comparison of the intensity of light passing through a sample (I) to the intensity of light passing through reference (Io). The ratio I/Io is known as the transmittance, and usually expressed as a percentage (%T). The absorbance, A, is then written as,

$$A = -\log_{10}(\%T/100) \quad \ldots\ldots\ldots\ldots\ldots\ldots\ldots (14)$$

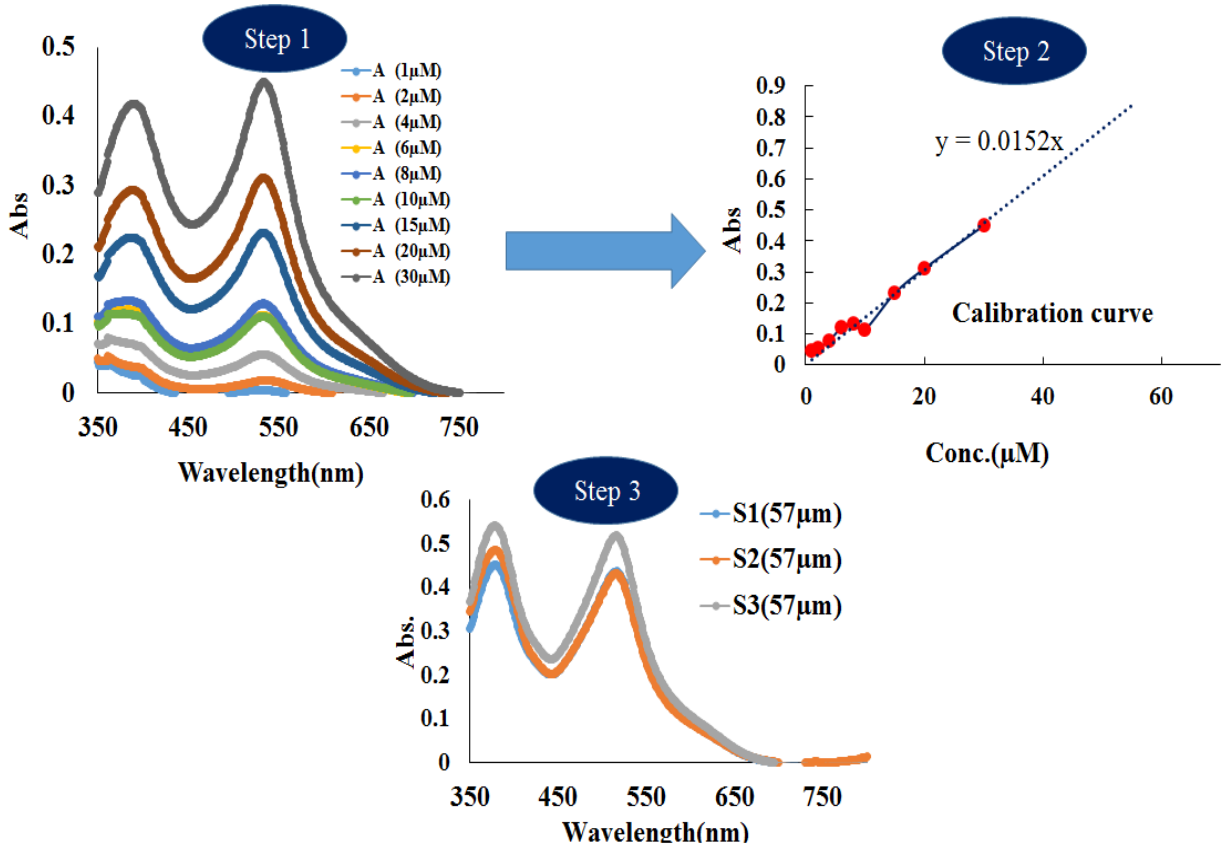

Figure 17. Steps involved in calculation for dye loading using UV-vis spectroscopy

In the present work, I have used UV-vis spectroscopy for calculating the dye loading (concentration of dye absorbed per unit square of the active area) of the device fabricated. The process involved is the dye desorption in equal volume of NaOH (0.1M), Ethanol, t-butyl alcohol, and acetonitrile. First a calibration curve is drawn using known concentration of the dye used as shown in Figure 17 (Step 1 & Step 2), then absorption spectra of the desorbed dye solution is taken & compared using the calibration curve for knowing the concentration. Finally the concentration of known desorbed volume thus obtained was divided by the total active area of the device. For example in Step 3, the sample S3 (57µm) has absorption peak value of **0.51728** (absorption peak seen for the highest wavelength), which corresponds to concentration of **34.48 µM**. In this case volume of desorbed solution taken is 5 ml, which gives concentration of the dye desorbed as **172.4 nmole**. The active area of device is 0.5 cm^2, hence dye loading is **344.12 nmol/cm^2**. The detailed discussion related to the effect of dye loading on device performance will be made in the chapters 3 and 4.

References:

1. He, H., Xiong, R., & Fan, J. (2011). Evaluation of lithium-ion battery equivalent circuit models for state of charge estimation by an experimental approach. *Energies*, *4*(4), 582-598.
2. Lorenzo, E. (Ed.). (1994). *Solar electricity: engineering of photovoltaic systems*. Earthscan/James & James.
3. Fahrenbruch, A.L; Bube, R.H. (1983). Fundamentals of solar cells. Photovoltaic solar energy conversion; Academic Press: New York.
4. Han, L., Koide, N., Chiba, Y., Islam, A., & Mitate, T. (2006). Modeling of an equivalent circuit for dye-sensitized solar cells: improvement of efficiency of dye-sensitized solar cells by reducing internal resistance. *Comptes Rendus Chimie*, *9*(5), 645-651.
5. Seo, H., Son, M. K., Lee, K. J., Kim, J., Hong, J. T. & Kim, H. J. (2008) A study on the improvement of the efficiency of dye-sensitized solar cell using the laser scribing and the grid electrode. *Transactions of the Korean Institute of Electrical Engineers*, 57(10), 1802–1806.
6. Saetre, T. O., Midtgård, O. M., & Yordanov, G. H. (2011). A new analytical solar cell I–V curve model. *Renewable Energy*, *36*(8), 2171-2176.
7. Lv, Z., Yu, J., Wu, H., Shang, J., Wang, D., Hou, S., Yongping, F., Kai, W. & Zou, D. (2012). Highly efficient and completely flexible fiber-shaped dye-sensitized solar cell based on TiO_2 nanotube array. *Nanoscale*, *4*(4), 1248-1253.
8. Barnes, P. R., & O'Regan, B. C. (2010). Electron recombination kinetics and the analysis of collection efficiency and diffusion length measurements in dye sensitized solar cells. *The Journal of Physical Chemistry C*, *114*(44), 19134-19140.
9. Green, M. A., Emery, K., Hishikawa, Y., Warta, W., & Dunlop, E. D. (2015). Solar cell efficiency tables (Version 45). *Progress in photovoltaics: research and applications*, *23*(1), 1-9.
10. Gabrielli, C. (1980) *Identification of Electrochemical Processes by Frequency Response Analysis*; Solartron Technical Report (http://www.solartronanalytical.com),.
11. Losee, D. L. (1975). Admittance spectroscopy of impurity levels in Schottky barriers. *Journal of Applied Physics*, *46*(5), 2204-2214.

12. Gomes, W. P., & Vanmaekelbergh, D. (1996). Impedance spectroscopy at semiconductor electrodes: review and recent developments. *Electrochimica acta*, *41*(7), 967-973.

13. Tomkiewicz, M. (1990). Impedance spectroscopy of rectifying semiconductor-electrolyte interfaces. *Electrochimica Acta*, *35*(10), 1631-1635.

14. Kelly, J. J., & Memming, R. (1982). The Influence of Surface Recombination and Trapping on the Cathodic Photocurrent at p‐Type III‐V Electrodes. *Journal of the Electrochemical Society*, *129*(4), 730-738.

15. Vanmaekelbergh, D. (1997). Direct and surface state mediated electron transfer at semiconductor/electrolyte junctions—II. A comparison of the interfacial admittance. *Electrochimica acta*, *42*(7), 1135-1141.

16. Fajardo, A. M., & Lewis, N. S. (1997). Free-energy dependence of electron-transfer rate constants at Si/liquid interfaces. *The Journal of Physical Chemistry B*, *101*(51), 11136-11151.

17. Raniero, L., Fortunato, E., Ferreira, I., & Martins, R. (2006). Study of nanostructured/amorphous silicon solar cell by impedance spectroscopy technique. *Journal of non-crystalline solids*, *352*(9), 1880-1883.

18. Mora-Seró, I., Luo, Y., Garcia-Belmonte, G., Bisquert, J., Muñoz, D., Voz, C., Puigdollors, J.,& Alcubilla, R. (2008). Recombination rates in heterojunction silicon solar cells analyzed by impedance spectroscopy at forward bias and under illumination. *Solar Energy Materials and Solar Cells*, *92*(4), 505-509.

19. Garcia-Belmonte, G., García-Cañadas, J., Mora-Seró, I., Bisquert, J., Voz, C., Puigdollers, J., & Alcubilla, R. (2006). Effect of buffer layer on minority carrier lifetime and series resistance of bifacial heterojunction silicon solar cells analyzed by impedance spectroscopy. *Thin Solid Films*, *514*(1), 254-257.

20. Proskuryakov, Y. Y., Durose, K., Taele, B. M., & Oelting, S. (2007). Impedance spectroscopy of unetched CdTe/CdS solar cells—equivalent circuit analysis. *Journal of Applied Physics*, *102*(2), 024504.

21. Kumar, R. A., Suresh, M. S., & Nagaraju, J. (2000). Measurement and comparison of AC parameters of silicon (BSR and BSFR) and gallium arsenide (GaAs/Ge) solar cells used in space applications. *Solar energy materials and solar cells*, *60*(2), 155-166.

22. Kumar, R. A., Suresh, M. S., & Nagaraju, J. (2004). GaAs/Ge solar cell AC parameters under illumination. *Solar energy*, *76*(4), 417-421.

23. H. Bayhan and A. S. Kavasoglu, Solar Energy, 2000, 361, 303.

24. Bisquert, J. (2002). Theory of the impedance of electron diffusion and recombination in a thin layer. *The Journal of Physical Chemistry B*, *106*(2), 325-333.

25. Fabregat-Santiago, F., Bisquert, J., Garcia-Belmonte, G., Boschloo, G., & Hagfeldt, A. (2005). Influence of electrolyte in transport and recombination in dye-sensitized solar cells studied by impedance spectroscopy. *Solar Energy Materials and Solar Cells*, *87*(1), 117-131.

26. Fabregat-Santiago, F., Bisquert, J., Palomares, E., Haque, S. A., & Durrant, J. R. (2006). Impedance spectroscopy study of dye-sensitized solar cells with undoped spiro-OMeTAD as hole conductor. *Journal of applied physics*, *100*(3), 034510.

27. Wang, Q., Moser, J. E., & Grätzel, M. (2005). Electrochemical impedance spectroscopic analysis of dye-sensitized solar cells. *The Journal of Physical Chemistry B*, *109*(31), 14945-14953.

28. Hoshikawa, T., Kikuchi, R., & Eguchi, K. (2006). Impedance analysis for dye-sensitized solar cells with a reference electrode. *Journal of Electroanalytical Chemistry*, *588*(1), 59-67.

29. Adachi, M., Sakamoto, M., Jiu, J., Ogata, Y., & Isoda, S. (2006). Determination of parameters of electron transport in dye-sensitized solar cells using electrochemical impedance spectroscopy. *The Journal of Physical Chemistry B*, *110*(28), 13872-13880.

30. Wang, Q., Ito, S., Grätzel, M., Fabregat-Santiago, F., Mora-Sero, I., Bisquert, J., Bessho, T & Imai, H. (2006). Characteristics of high efficiency dye-sensitized solar cells. *The Journal of Physical Chemistry B*, *110*(50), 25210-25221.

31. Garcia-Belmonte, G., Munar, A., Barea, E. M., Bisquert, J., Ugarte, I., & Pacios, R. (2008). Charge carrier mobility and lifetime of organic bulk heterojunctions analyzed by impedance spectroscopy. *Organic Electronics*, *9*(5), 847-851.

32. Bisquert, J., Garcia-Belmonte, G., Munar, A., Sessolo, M., Soriano, A., & Bolink, H. J. (2008). Band unpinning and photovoltaic model for P3HT: PCBM organic bulk heterojunctions under illumination. *Chemical Physics Letters*, *465*(1), 57-62.

33. Kern, R., Sastrawan, R., Ferber, J., Stangl, R., & Luther, J. (2002). Modeling and interpretation of electrical impedance spectra of dye solar cells operated under open-circuit conditions. *Electrochimica Acta*, *47*(26), 4213-4225.

34. Iijima, S. (1991). Helical microtubules of graphitic carbon. *Nature*, *354*(6348), 56-58.

35. Yada, M., Inoue, Y., Uota, M., Torikai, T., Watari, T., Noda, I., & Hotokebuchi, T. (2007). Plate, wire, mesh, microsphere, and microtube composed of sodium titanate nanotubes on a titanium metal template. *Langmuir*, *23*(5), 2815-2823.

36. Teshima, K., Lee, S., Murakoshi, S., Suzuki, S., Kiyohara, M., Yubuta, K., ... & Oishi, S. (2010). A unique three-dimensional photocatalytic structure consisting of highly crystalline $Na_2Ti_3O_7$ whiskers grown from a NaCl flux. *Crystal Growth & Design*, *10*(6), 2533-2540.

37. Dong, X., Li, Y., Lin, Z., Ge, J., & Qiu, J. (2013). Oriented TiO_2 nanowire array grown on curved surface of Ti wire with superior photoelectrochemical properties. *Applied Surface Science*, *270*, 457-461.

38. Liu, H., Wang, D., Ji, L., Li, J., Liu, S., Liu, X., & Jiang, S. (2010). A novel TiO_2 nanotube array/Ti wire incorporated solid-phase microextraction fiber with high strength, efficiency and selectivity. *Journal of Chromatography A*, *1217*(12), 1898-1903.

39. Huang, S., Zhang, Q., Huang, X., Guo, X., Deng, M., Li, D., ... & Meng, Q. (2010). Fibrous CdS/CdSe quantum dot co-sensitized solar cells based on ordered TiO_2 nanotube arrays. *Nanotechnology*, *21*(37), 375201.

40. Lu, X., Wang, G., Zhai, T., Yu, M., Gan, J., Tong, Y., & Li, Y. (2012). Hydrogenated TiO_2 nanotube arrays for supercapacitors. *Nano letters*, *12*(3), 1690-1696.

41. O'regan, B., & Grätzel, M. (1991). A low-cost, high-efficiency solar cell based on dye-sensitized colloidal TiO_2 films.

42. Chen, C. C., Chung, H. W., Chen, C. H., Lu, H. P., Lan, C. M., Chen, S. F., ... & Diau, E. W. G. (2008). Fabrication and characterization of anodic titanium oxide nanotube arrays of controlled length for highly efficient dye-sensitized solar cells. *The Journal of Physical Chemistry C*, *112*(48), 19151-19157.

43. Wang, D., Liu, L., Zhang, F., Tao, K., Pippel, E., & Domen, K. (2011). Spontaneous phase and morphology transformations of anodized titania nanotubes induced by water at room temperature. *Nano letters*, *11*(9), 3649-3655.

44. Liu, N., Albu, S. P., Lee, K., So, S., & Schmuki, P. (2012). Water annealing and other low temperature treatments of anodic TiO_2 nanotubes: a comparison of properties and efficiencies in dye sensitized solar cells and for water splitting. *Electrochimica Acta*, *82*, 98-102.

45. Kim, T. K., Lee, M. N., Lee, S. H., Park, Y. C., Jung, C. K., & Boo, J. H. (2005). Development of surface coating technology of TiO_2 powder and improvement of photocatalytic activity by surface modification. *Thin Solid Films*, *475*(1), 171-177.

46. Kavan, L., Grätzel, M., Gilbert, S. E., Klemenz, C., & Scheel, H. J. (1996). Electrochemical and photoelectrochemical investigation of single-crystal anatase. *Journal of the American Chemical Society*, *118*(28), 6716-6723.

47. Jafari, M., Vaezzadeh, M., & Noroozizadeh, S. (2010). Thermal Stability of α Phase of Titanium by Using X-Ray Diffraction. *Metallurgical and Materials Transactions A*, *41*(13), 3287-3290.

48. Malinov, S., Sha, W., Guo, Z., Tang, C. C., & Long, A. E. (2002). Synchrotron X-ray diffraction study of the phase transformations in titanium alloys. *Materials Characterization*, *48*(4), 279-295.

49. Muguruma, T., Iijima, M., Brantley, W. A., Yuasa, T., Ohno, H., & Mizoguchi, I. (2011). Relationship between the metallurgical structure of experimental titanium miniscrew implants and their torsional properties. *The European Journal of Orthodontics*, *33*(3), 293-297.

50. Hanawa, T. (2011). A comprehensive review of techniques for bio functionalization of titanium. *Journal of periodontal & implant science*, *41*(6), 263-272.

51. Christau, S., Thurandt, S., Yenice, Z., & von Klitzing, R. (2014). Stimuli-Responsive Polyelectrolyte Brushes As a Matrix for the Attachment of Gold Nanoparticles: The Effect of Brush Thickness on Particle Distribution. *Polymers*, *6*(7), 1877-1896.

CHAPTER 3: NOVEL TCO-LESS COIL TYPE CYLINDRICAL DYE SENSITIZED SOLAR CELLS

3.1 Introduction

Dye sensitized solar cells (DSSCs) have now reached the power conversion efficiency of 13% [1] since their invention in 1991 [2]. Low-cost of fabrication, simple manufacturing process along with some properties such as lightweight, flexible and performance in variable light conditions [3] have compelled the DSSC research to stand on the forefront of commercialization. The number of publications related to each component of DSSC have increased dramatically in past few years [4]. Although DSSCs are still lagging in conversion efficiencies compared to its inorganic solar cells counterparts such as crystalline silicon, amorphous silicon, CIGS and other. However, with the ongoing research in the field of taking DSSC from lab research to real life application using cost-effective transparent conductive-oxide less (TCO-less) architecture implemented mainly by the use of flexible substrates such as Titanium (Ti) and Stainless-Steel (SS) based mesh, foil and wires [5-8] have introduced DSSC as a strong contender for the solar cells towards commercialization. Fragile nature of the TCO and restrictions on shape variations, polymer based flexible plastic electrode for the DSSCs [12] have also been reported. However, due to lack of high temperature durability of polymers, we have reported stainless-steel mesh coated with gradient TiOx layer working as flexible working electrode [9]. This mesh based electrode has recently been utilized in our laboratory to fabricate DSSCs in the cylindrical device architecture [13]. The cylindrical DSSC was fabricated by inserting this flexible metal mesh based photoanode, metal rod as counter electrode and porous polymer film containing electrolyte into a cylindrical glass tube. Cylindrical TCO-less DSSCs offer additional advantage over flat standard DSSC such as self-light tracking, reduced sealing and installation costs.

In the TCO-less DSSC device architecture, to reduce the cost of metal mesh fabrication, some of the works pertaining to the fabrication of DSSCs based on metallic wires have also been reported in the recent past [13-16]. Liu et al. [15] have reported a device structure utilizing titanium wire in the spiral shape. In this structure the large amount of electrolyte inserted may be responsible for less absorption of incident light by TiO_2 coated wire. Fu et al.

[16] have also reported the DSSCs having cylindrical architecture based on the metallic wires, however, we feel that in their architecture, the counter electrode (Pt wire) could hinder the incident light falling on to the photo electrode owing to the shading effect by top catalytic and current collecting electrode. Problems pertaining to such shading effect due to counter electrode leading to reduced photon harvesting have been realized and discussed already in the recent past [17-19]. Some researchers directed their efforts in this context with partial successes [15, 19]. However, in the case of complete removal of the shading effect, other issues such as large electrolyte insertion and complex fabrication process are still the existing technical barriers. Keeping these pros and cons in mind, we would like to report a novel TCO-less DSSC architecture to fabricate cylindrical DSSCs based on nanoporous TiO_2 coated metal wires. The structure showed its effectiveness for roll-to-roll mass production compared to conventional and previous cylindrical DSSCs architecture reported so far. The machinery required and stages of production (such as, mount making, wire coiling, glass tube preparation, base preparation, sealing and assembly used in the incandescent lighting appliance production technology) is almost similar and can be easily adopted for the investigated coil type cylindrical architecture.

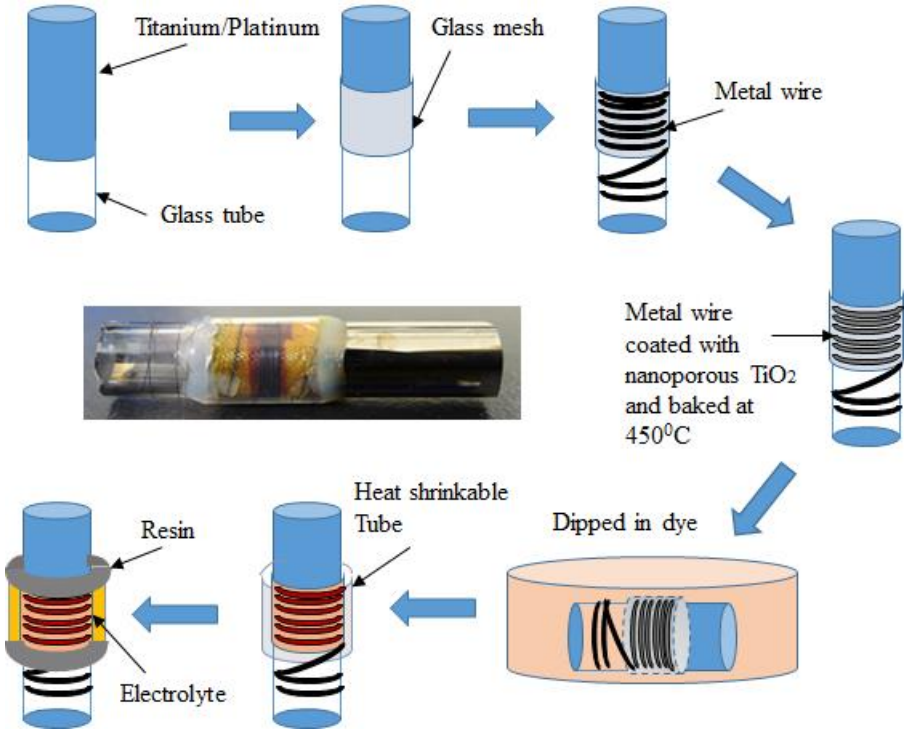

Figure1. Schematic representation for the fabrication of coil type TCO-less cylindrical DSSC [8].

3.2 Experimental

3.2.1 Device fabrication: Figure 1 exhibits the schematic of the processes involved in the fabrication of coil type cylindrical DSSC (C-DSSC). First a thin layer of titanium metal (240 nm) was sputtered on a cylindrical glass tube (outer diameter, 7 mm) followed by coating of a thin Pt catalytic layer (60 nm) to fabricate the counter electrode. A glass mesh (20 µm thick, Asahi glass Co. Japan) was then wrapped over the counter electrode to work as spacer along with serving the purpose of holding the redox electrolyte also. The metal wires were then wrapped by coiling them around the glass mesh. Figure 2 shows the different components used for the fabrication of solar cell in the present work. Nanoporous TiO_2 D/SP (Solaronix SA) was coated over the wrapped wire. The TiO_2 paste was diluted with ethanol (2.5:1) and mixed properly using mortar & pestle before coating on the wrapped wires. The TiO_2 coated wire was gradually heated from room temperature to 450^0C for 1 hour followed by sintering at this temperature for 30 min. The sintered electrode was allowed to cool down to 100^0C and was subjected to sensitization with the dye cis-bis (isothiocyanato)- bis(2,20-bypyridyl-4,40-dicarboxy-lato) ruthenium(II)bis-tetrabutyl ammonium (Solaronix SA, Ruthenium 535 bisTBA abbreviated as N719) 0.3 mM in t-butyl

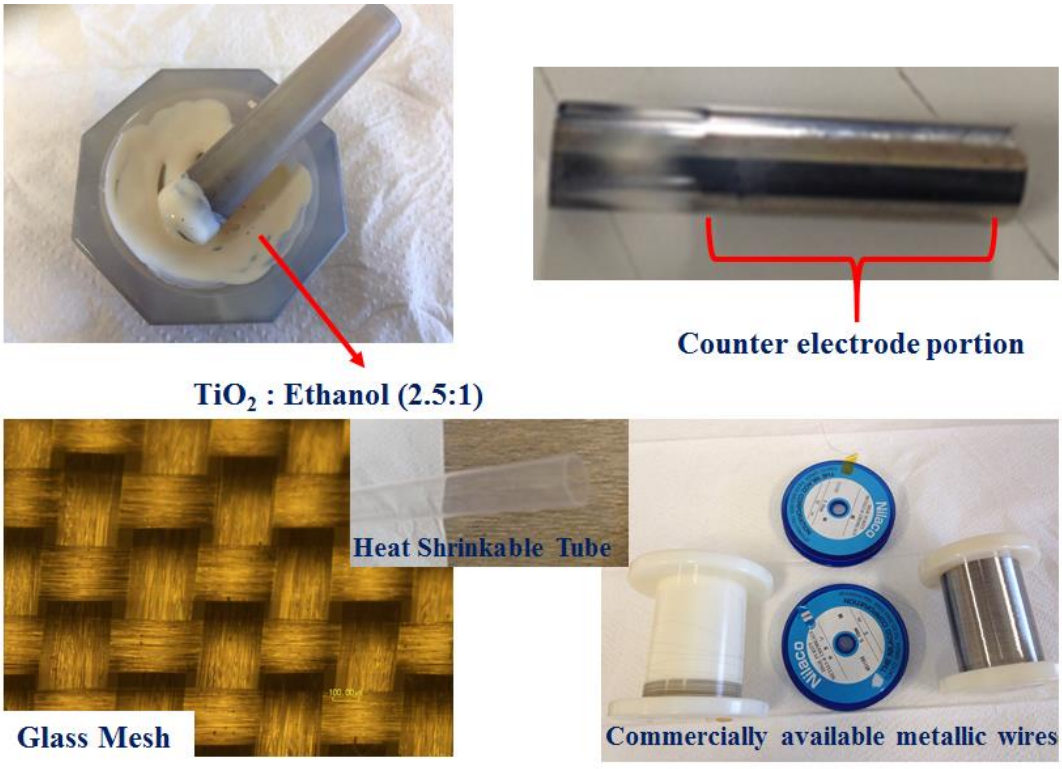

Figure 2. Components used for fabrication of the device

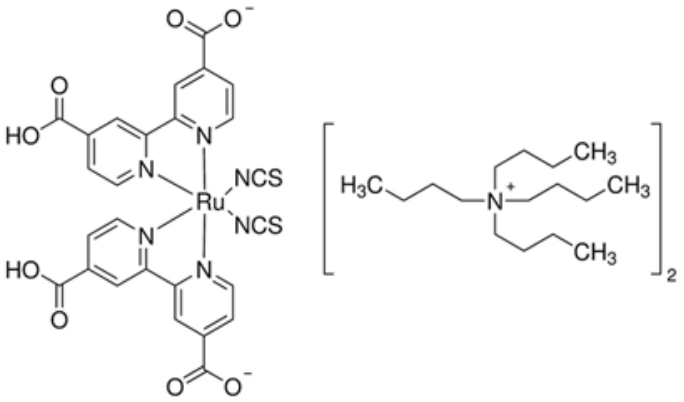

Figure 3. Molecular structure for the N719 dye

alcohol and acetonitrile (1 : 1 v/v) for 24 hours at the room temperature. Figure 3 shows the molecular structure of the sensitizing N719 dye. The structure was then covered with heat shrinkable tube (ø = 9.5 mm, JUNFLON NF090, Junkosha Inc., Japan) which shrinks to (ø = 7.3 mm) after heating at 120^0C for 5 min. Finally electrolyte containing 50 mM iodine, 500 mM lithium iodide, 580 mM t-butylpyridine and 600 mM 1-ethyl-3-methylimidazolium dicyanamide in acetonitrile was filled inside the heat shrinkable tube containing the whole structure and sealed at the both ends.

3.2.2 Metallic wires: The wires utilized for the present work were (1) commercially available Ti wire (ø=57 μm), (2) stainless steel wire (SUS-316, ø=50 μm), (3) Copper (Cu, ø=50 μm), Ti coated Copper wire (Cu/Ti, ø=43 μm) and (3) Ti sputtered stainless steel wire (SUS-316, ø=50 μm). All the metal wires used in this work were employed as received without any prior surface treatments until mentioned specifically. The thickness of the sputtered Ti on stainless-steel wire was kept 240 nm in all the cases.

3.2.3 Current-Voltage measurement: Photovoltaic performance of the device was measured with a solar simulator (KHP-1, Bunko-Keiki, Japan) equipped with a xenon lamp (XLS-150A). The intensity of light irradiation was adjusted to AM 1.5 (100 $mWcm^{-2}$). The solar simulator spectrum and its power was adjusted using a spectroradiometer (LS-100, Eiko Seiki, Japan). The exposure power was also corrected with standard amorphous Si photo detector (BS-520 S/N 007, Bunko Keiki, Japan), which has similar visible light sensitivity to the DSSC. The irradiation area of the device was calculated by multiplying the width of the wire wrapped with the diameter of

the counter electrode. The device characteristics were measured without any mask and whole device was exposed to the simulated light source. Photocurrent action spectrum also known as incident photon to current conversion efficiency as function of wavelength for the devices prepared were measured with a constant photon flux of $1*10^{16}$ photon per cm^2 at each wavelength in the direct current mode using the action spectrum measurement system connected to the solar simulator (CEP-2000, Bunko Keiki, Japan).

3.2.4 Electrochemical impedance spectroscopy: EIS was carried out with a frequency response analyzer (Solartron Analytical, 1255B) connected to a Potentiostat (Solartron Analytical, 1287) under illumination of 100 mW cm^{-2} light using a Yamashita Denso YSS-50A solar simulator. EIS measurements were performed in the frequency range of $5 * 10^{-3}$ to 10^5 Hz at room temperature. The electrical impedance spectra were analyzed using Z-View software (Solartron Analytical).

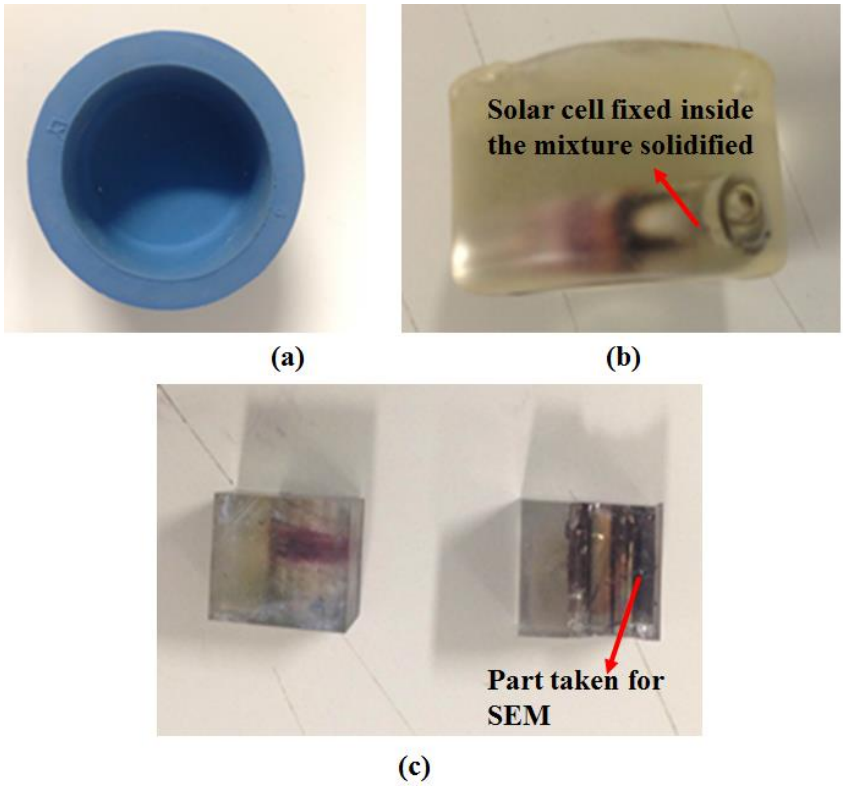

Figure 4. Sample preparation for measurement of thickness using SEM

3.2.5 Thickness measurement using scanning electron microscope (SEM): Thickness measurement for the cylindrical solar cell is quite different. First a mixture of Epoxycure epoxy resin (BUEHLER) and Epoxycure epoxy hardener (BUEHLER) in ratio of 5:1 was prepared. This mixture was then poured inside a cylindrical rubber cavity (a) as shown in Figure 4, and then solar cell was dipped into it and kept for 24 hours so that it can be fixed inside it once the mixture gets solidified (b). Finally the solidified part containing solar cell was cut down diametrically into small piece. The part taken for SEM analysis (C) was rubbed with sand papers and coated with a thin layer of gold (100 nm). Finally the thickness of the nanoporous TiO_2 film coated on the different metal wires was estimated by taking the cross-sectional image using scanning electron microscope (JEOL, NeoScope JCM-6000).

3.3 Results and discussion

3.3.1 Working principle and cross-sectional view:

Figure 5a shows schematic cross-sectional view of the C-DSSC device architecture. Typically, its working principle is similar to the conventional DSSC. Dye molecules adsorbed over the nanoporous TiO_2 layer harvests the photons. Photoexcited dye molecules inject electrons into the conduction band of the TiO_2 layer. Electrons are then transported towards the metal wire and to the external circuit leading to counter electrode (Ti/Pt). The oxidized dye is then reduced by I^- present in the glass mesh soaked with electrolyte and this I^- is reproduced by the reduction of I_3^- with electrons from counter electrode (Ti/Pt). Figure 5b exhibits the scanning electron microscopic (SEM) image for the cross sectional view of the photoanode which was taken in order to determine the thickness of the nanoporous TiO_2 layer coated on to the metal wire. Relatively less contrasting nanoporous TiO_2 layer can be clearly seen which is mainly coated on the top of the metal wires and the spacing between the wires. At the same time, average thickness of this nanoporous TiO_2 layer was found to be approximately 10 μm.

3.3.2 Solar cell performance using different wires:

The coil based cylindrical solar cells first fabricated using three wires namely Copper (Cu) which is highly conducting in nature [20], Titanium (Ti) wire which is highly resistive to corrosion and have high strength to density ratio [21] and Stainless-Steel (SS) which is an alloy having good

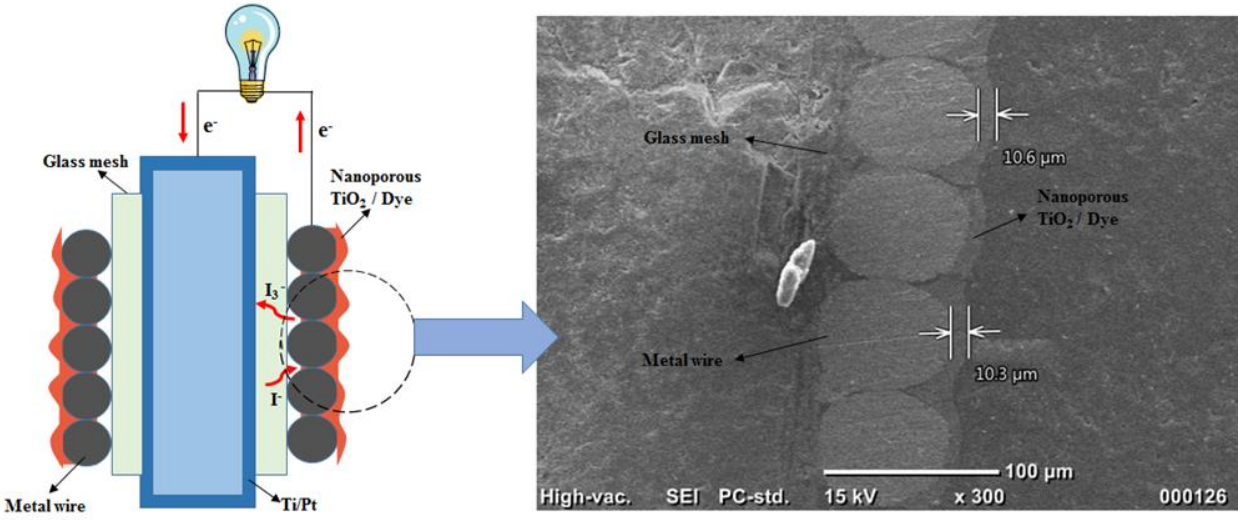

Figure 5(a) Schematic cross-sectional view of the device. (b) Scanning electron microscope image of nanoporous TiO_2 coated metal wire [8].

conductivity and good corrosion resistance properties [24]. From here onwards, wherever necessary we will use terminology such as Ti-cell for Ti wire based cylindrical solar cell and so for other wire based device also. Figure 6 reveals the direct impact of electrical and physical properties of wires on the solar cell performance along with the resulting photovoltaic parameters as shown in the table 1. Since, copper is highly reactive in nature, therefore, the electrolyte which contains highly corrosive iodine ions (I^- & I_3^-) is damaging the Cu wire leading to poorest performance for the device with 0.23 % PCE. Similarly, SS and Ti because of their better corrosion resistance properties shows better performance. SS-cell showed highest PCE among these three wire based solar cell with PCE of 2.03%, FF of 0.49, Voc of 0.66 V and Jsc of 6.21 mA/cm^2. Low performance of Ti-cell compared to SS-cell can be explained by observing the dark current characteristics which shows the higher recombination in case of Ti-cell responsible for lower Jsc of 4.89 mA/cm^2 and Voc of 0.59 V with poor FF of 0.39 compared to SS-cell.

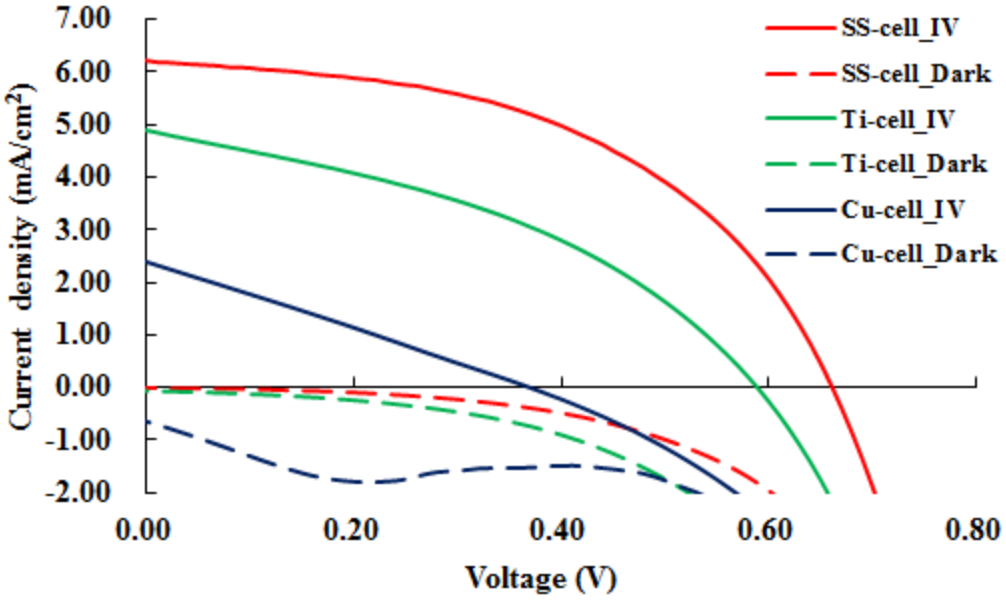

Figure 6 (a) Current-Voltage and dark current characteristics of device fabricated using Stainless-steel (SS), Titanium (Ti), & Copper (Cu) wires.

Table1. Photovoltaic performance for the devices (C-DDSCs) fabricated using different metal wires under investigation

	Cu-cell	SS-cell	Ti-cell
Efficiency [%]	0.23	2.03	1.13
FF	0.26	0.49	0.39
Voc [V]	0.37	0.66	0.59
Jsc [mA/cm^2]	2.39	6.21	4.89

3.3.2.1 Combining wire properties (a): The purpose here and after was to investigate the effect of combining the properties of two metals in a single wire on the solar cell performance. To accomplish this goal, a hybrid wire consisting of Cu (ø= 38 µm) externally coated with 5 µm layer of Ti (Cu/Ti) which was received from Nachi-Fujikoshi Corp., Japan. Figure 7 exhibits the photovoltaic characteristics for TCO-less C-DSSC fabricated using this hybrid wire (Cu/Ti-cell). It can be clearly seen that there is a large improvement in the photovoltaic parameters compared to Cu-cell. The Jsc of 9 mA/cm^2, FF of 0.63, Voc of 0.66 V gives improved PCE of 3.72%. This is probably due to the passivating action of Ti, which is reducing the charge recombination and

hence resulting in the higher device performance. Hence after realizing the passivating action of Ti, we further did the same experiment on the SS wire and performed the detailed analysis to deeply understand our device performance.

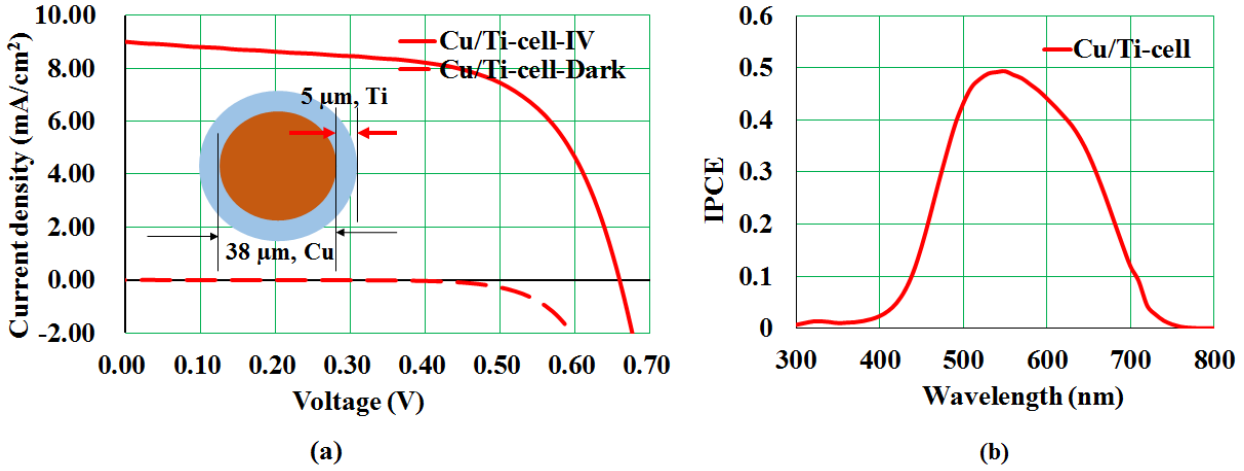

Figure 7 (a) Current-Voltage characteristic for Cu/Ti-cell (inset shows the diameter of the wire) (b) IPCE of Cu/Ti-cell.

3.3.2.2 Combining wire properties (b): Figure 8 shows photovoltaic performance of the coil based TCO-less cylindrical solar cells fabricated using different metal wires utilized for the fabrication of the photoanode along with the photovoltaic parameters shown in the Table 2. This Figure and Table 2 clearly indicate that nature of the wire plays an important role towards controlling the overall photoconversion efficiency of the device. Photoconversion efficiencies (η %) were found to be in the order Ti < SS-steel (SS) < Ti-sputtered stainless steel (SS/Ti) wires. A remarkable enhancement in the photoconversion efficiency was observed for photoanode based on SS/Ti wires as compared to the cylindrical DSSCs fabricated using SS and Ti wires alone without surface passivation with pure Ti layer. This tremendous increase in the overall photoconversion efficiency of coil based cylindrical DSSC using SS/Ti was resulting from enhancement in the all of the photovoltaic parameters such as open circuit voltage (Voc), short circuit current density (Jsc) and fill factor (FF) as shown in the Table 2. Under simulated AM 1.5 solar irradiation, this SS/Ti wire based DSSC exhibited a Jsc of 8.75 mA/cm^2 with much improved FF of 0.63 and an enhanced Voc of 0.70 V resulting in to the overall photoconversion efficiency of 3.88%.

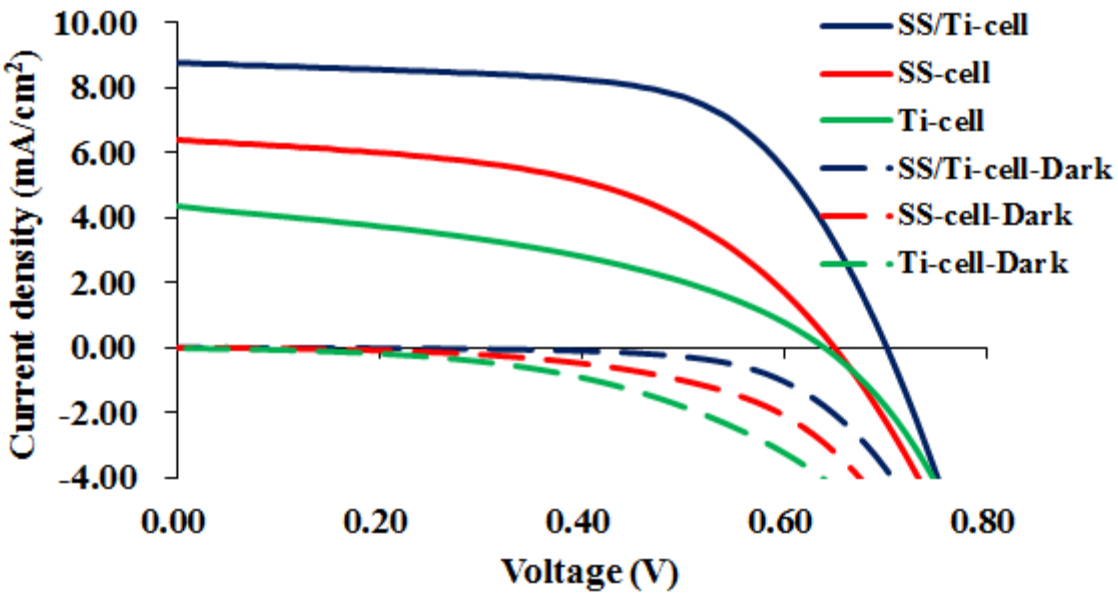

Figure 8 Photo/dark current–voltage characteristic for DSSCs using different metal wires [8].

Table 2 Photovoltaic and EIS parameters for metal wire based TCO-less cylindrical solar cells under simulated solar irradiation.

Parameter	SS-cell	SS/Ti-cell	Ti-cell
Efficiency (%)	2.09	3.88	1.12
FF	0.50	0.63	0.40
Voc [V]	0.65	0.70	0.64
Jsc [mA/cm^2]	6.38	8.75	4.35
R1 (Ω)	35.47	36.43	25.97
R2 (Ω)	100.2	88.38	56.43
R3 (Ω)	391.2	188.1	2433
Dye loading amount[nmol/cm^2]	319.4	318.6	322.6

On the other hand Ti wire exhibited the poorest photovoltaic performance (η = 1.12%) which was highly affected by the drastically hampered both of the Jsc and FF. Another striking difference can be noticed that photoanodes based on Ti and SS wires, the observed dark currents (leakage current) are much higher as compared to the photoanode based on SS/Ti wires. Therefore, this hampered dark current for SS/Ti could be attributed to the observation of higher Voc due to suppressed charge recombination. Thus sputtering of thin titanium over layer on the

stainless steel wire could be the possible reason for the reduced charge recombination as titanium coating forms charge recombination blocking layer [9].

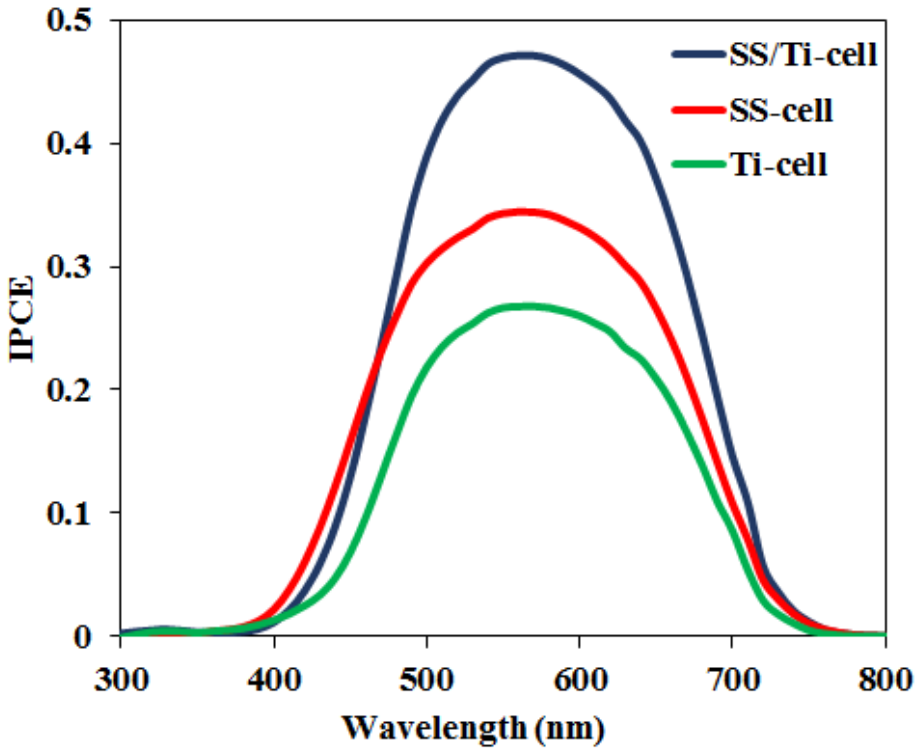

Figure 9 Incident photon-to-current conversion efficiency (IPCE) curves for TCO-less coil based DSSCs using different metal wires [8].

Since Jsc is one of major controlling factors of the overall photoconversion efficiency of our coil based cylindrical DSSCs with the nature of metal wires under investigation, spectral response of the DSSCs were also measured to elucidate this observed differential behaviour. Figure 9 depicts the incident photon-to-current conversion efficiency (IPCE) as a function of wavelength. It can be clearly seen that DSSC based on SS/Ti wire exhibits the highest IPCE (48%) at around 550 nm (absorption maximum of N-719 on TiO_2 surface) supports the highest observed Jsc in the J–V curve as compared to DSSCs based on other wires. Lack of photon harvesting in the 300–400 nm wavelength region could be attributed to the available electrolyte layer between the heat shrinkable tube and photoanode which is still large enough to absorb the appreciable amount of light by the electrolyte layer itself. Such kind of observations has also been made and reported by our group previously for the TCO-less cylindrical DSSCs based on SS-mesh [13].

The possibility of difference in IPCE could also be argued due to different extent of the dye loading on different metal wire surfaces coated with nanoporous TiO_2. To check the validity of this reason, the amount of dye loading was also estimated using equal volume of NaOH (0.1 M) solutions of ethanol, t-butyl alcohol and acetonitrile as dye desorption solvent. The results pertaining to estimation of the extent of dye molecules as shown in Table 2 strictly ruled out this possibility as it shows approximately same amount of dye loading for all of the three metal wire based photoanodes. In order to understand observed differential photovoltaic behaviour for the photoanodes based on different metal wires particularly Jsc, EIS measurements were also conducted to investigate the interfacial charge transfer processes. To analyze the EIS spectra, adequate physical models and suitable equivalent circuits have been proposed and widely implemented to study interfacial electron transfer processes in DSSCs [23-27].

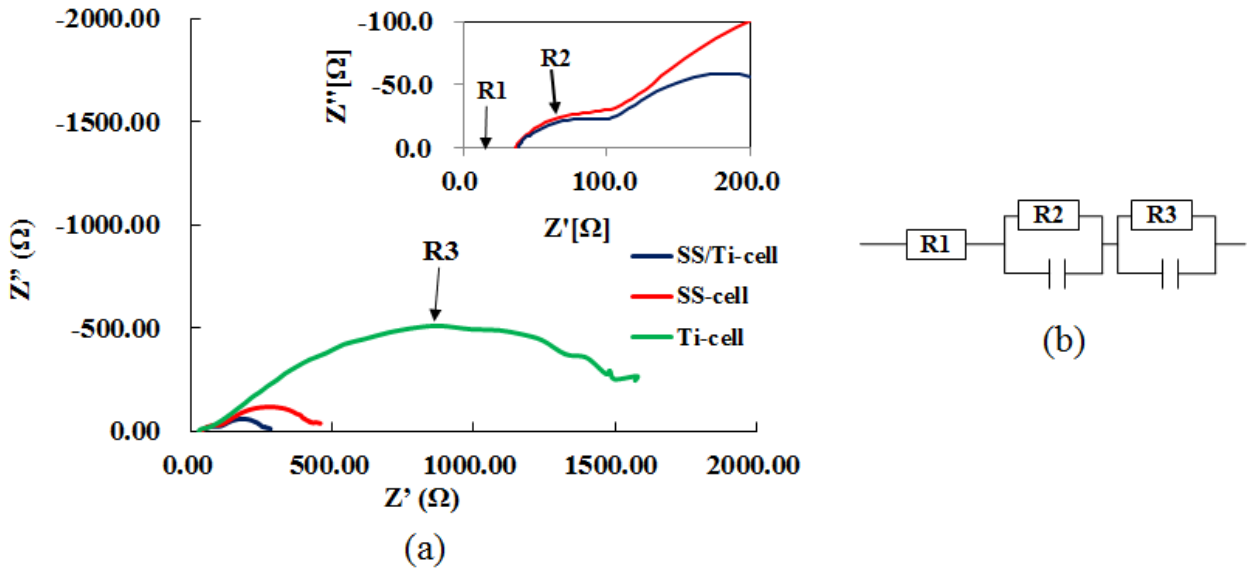

Figure 10 (a) EIS spectra of coil based TCO-less DSSCs measured at AM 1.5 and constant Jsc of 1 mA/cm^2 and (b) electrical equivalent circuit for impedance spectra [8].

Figure 10 exhibits the plot of real vs. imaginary part of the complex impedances (Nyquist plot) measured under AM 1.5 light illuminations at a constant Jsc of 1 mA/cm^2. First impedance element (R1) in the high frequency region is attributed to the series resistance of the conducting layer such as metal wires in the present case, which do not show appreciable differences. The

resistance associated with first semi-circle (R2) is assigned to the charge transfer at the counter electrode, which was not an important factor for the observed differential behavior of the solar cell performance. The second semi-circle appearing in the mid frequency region is attributed to be originated from the charge-transfer resistance (R3) of working electrode/TiO_2 and TiO_2/electrolyte interfaces. There are two possible interpretations for the origin of this semi-circle [28]. First is related to the proper electrical contact between the metal wire and TiO_2 nanoparticle while second interpretation is associated with charge recombination between TiO_2 and electrolyte [26, 28].The most striking differences in the resistance for this second semi-circle was observed for the photoanodes using different metal wires in the present investigation. SS/Ti shows very small resistance (188 Ω) in this region as compared to Ti wire (2433 Ω) which can be explained by enhanced interfacial adhesion between working electrode and nanoporous TiO_2. This facilitates the facile electron transport resulting into improved photovoltaic performance. The second possibility of large recombination resistance for Ti in our case can be ruled out since it shows relatively small Jsc and Voc as compared to the SS/Ti. The differential behaviour observed for photoanodes based on Ti and SS/Ti wires can be, therefore, explained by the presence of different extents of TiOx surface defects on the commercially procured Ti wire which might be passivated by sputtering of pure titanium on the stainless steel wire (SS/Ti) and are supposed to promote the better contact between the metal wire and nanoporous TiO_2. Similar enhancement in the electrical contact formation between the substrate and nanoporous TiO_2 by different kinds of surface treatments of metal foil for TiOx surface passivation resulting into improved photovoltaic performance has also been advocated by An *et al* [29].

3.3.2.3 Implementation on titanium wires:

Thin Ti layer when sputtered on SS is working as a passivating layer and leading to enhanced solar cell performance for SS/Ti-cell. However, poor performance obtained with photoanodes fabricated using as supplied Ti wires could be attributed to the probability of existence of different extent of surface oxidized impurities which might be responsible for poor performance. To confirm this, we sputtered pure Ti on the surface of Ti wire and prepared device and measured its characteristics, shown as Ti/TiSp-cell in Figure 11 along with the photovoltaic parameters listed in the Table 3. From the table 3 it can be seen that FF increased from 0.42 to 0.54, Voc from 0.57 V to 0.66 V and Jsc from 3.00 mA/cm^2 to 7.21 mA/cm^2 after sputtering of pure Ti leading to overall increased in PCE from 0.71% to 2.57%. This increased performance

after Ti sputtering confirmed existence of impurities are the reason for poor performance with Ti-cell. Since after sputtering the effect of the surface impurities have been reduced. This interesting result lead us to deeply study the surface properties of Ti wire, which will be discussed in detail in the next chapter 4.

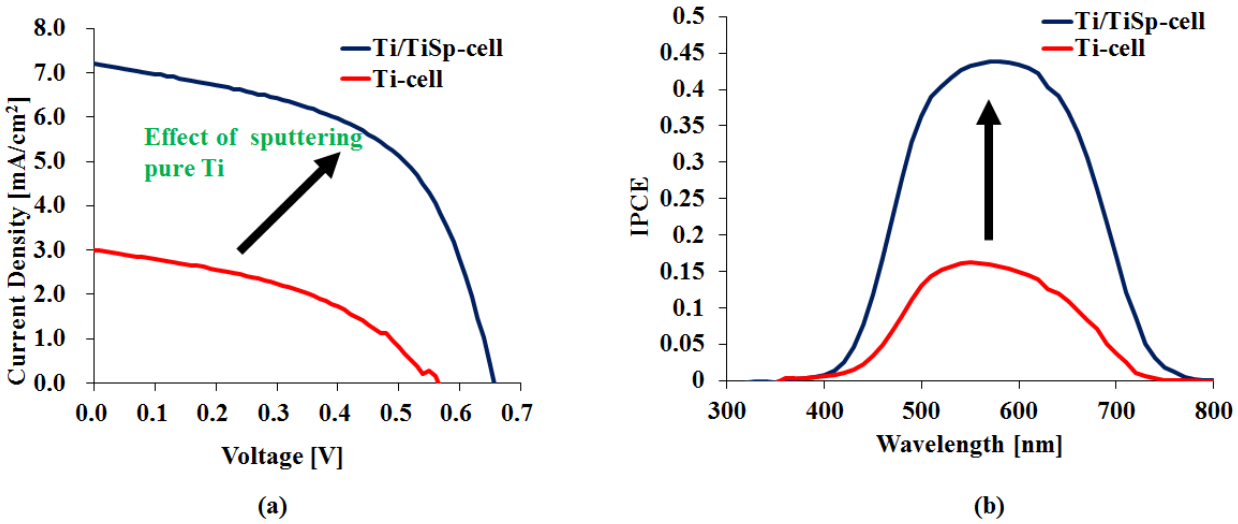

Figure 11. Photovoltaic characteristics after sputtering pure Ti on commercially available Ti leads to increase in performance of the device

Table 3 Photovoltaic parameters after sputtering pure Ti on commercially available Ti wire

	Ti/TiSp-cell	Ti-cell
Eff[%]	2.57	0.71
FF	0.54	0.42
Voc[V]	0.66	0.57
Jsc(mA/cm²)	7.21	3.00

3.3.3 A closer look to irradiation area (different wire gap): Irradiation area is an important issue for our solar cells (cylindrical shape) as the working electrode involves the wrapping of wires manually by hand. The spacing between the wires, therefore, can't be uniform as the wires are very fine and thin in diameter. The conventional area of irradiation is the width of the wire wrapped multiplied by the diameter of the glass tube over which these are wrapped. Here we have fabricated the three cells with approximately same active area using the same wire quality,

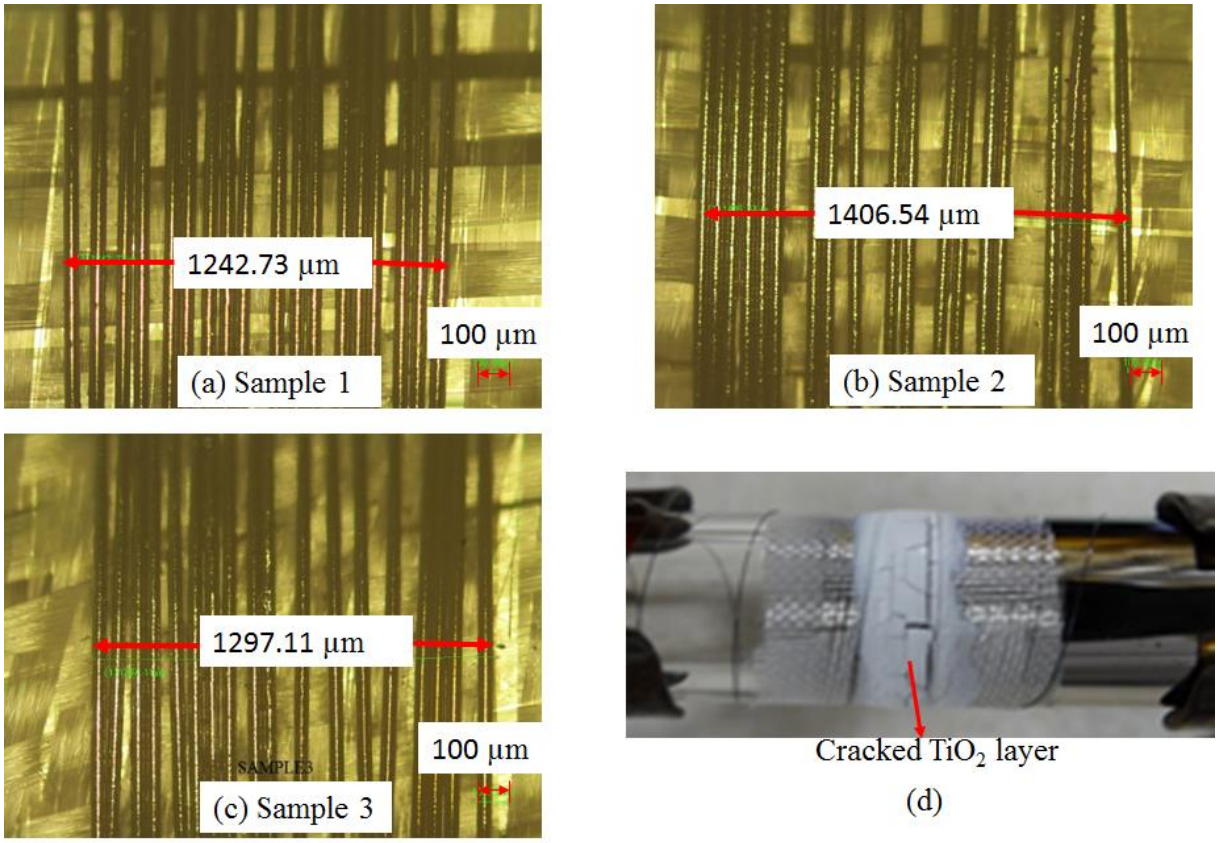

Figure 12 (a, b, & c) Microscopic images of the wrapped wires used as working electrode (d) Image showing cracking in TiO_2 layer when gaping is too large

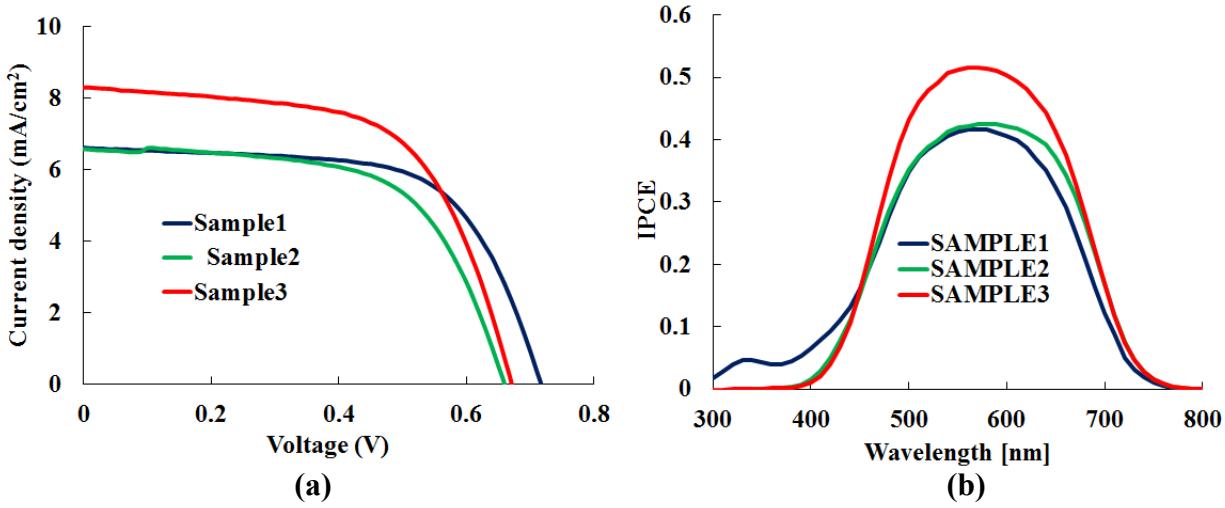

Figure 13 Photovoltaic characteristics for different wire arrangements

however, the arrangement of wires and spacing between them were different as shown in the Figure 12. The gaps between the wires are even more than 100 μm, but in that case also the devices are performing well. Figure 13 shows the photovoltaic characteristics for all of the samples with its parameters listed in Table 4.

Table 4 Photovoltaic parameters obtained using different arrangement of wires

	SAMPLE1	**SAMPLE2**	**SAMPLE3**
Eff [%]	3.04	2.68	3.38
FF	0.64	0.61	0.61
Voc[V]	0.71	0.65	0.67
Jsc[mA/cm^2]	6.61	6.57	8.30
Active [cm^2]	0.0850	0.0980	0.0900

It shows nearly same performance for all the devices under consideration. Although, some differences in the photovoltaic performance associated with gap due to different arrangement of wires was observed but is not much prominent. However, when there was increase in the gap between the wires further the possibilities of cracking in the sintered layer of TiO_2 was quite frequent as shown in Figure 12 (d).

3.3.4 A closer look to irradiation area (different irradiation area) It is well know that resistance of the wire is directly proportional to its length. Figure 14 shows this effect on the performance of our fabricated devices. For larger area we need to wrap more wire thus more length of the wire will be used. The device with active area of 0.085 cm^2 has FF of 0.71 which is less (0.53) for the device with more than two times active area (0.21 cm^2) and seems to be the main factor for variable performance of the two devices. As FF decreases with increase in the series resistance, therefore, the increased wire length in case of 0.21 cm^2 wrapped area is responsible for decreased value of FF. Although, there is decrease in value of FF, however, total PCE was not much affected. This is probably due to large area providing more photogenerated electrons to collect and also wires are working as current collecting grids, therefore overall PCE is almost same.

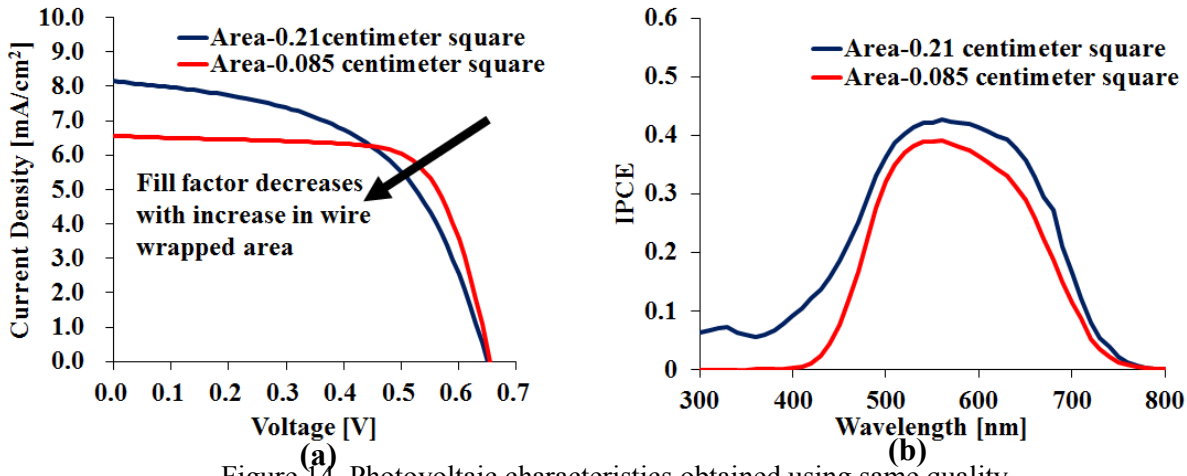

Figure 14. Photovoltaic characteristics obtained using same quality wire with different wrapped area

Table 5. Photovoltaic parameters obtained using same quality wire with different wrapped area

	Area-0.21centimeter square	**Area-0.085centimeter square**
Eff[%]	2.82	3.04
FF	0.53	0.71
Voc[V]	0.65	0.65
Jsc[mA/cm^2]	8.15	6.56
Active [cm^2]	0.2100	0.0850

3.4 Conclusions

In conclusion, we fabricated a novel TCO-less cylindrical dye-sensitized solar cell with more ease and fast method of fabrication compared to other TCO-less DSSC architectures. Problems related to previous device architectures such as shading effect and complex fabrication process were minimized. It has been demonstrated that nature of wire and surface treatment plays an important role in controlling the device performance. EIS investigation revealed that in spite of charge recombination between TiO_2/dye/electrolyte interfaces, better electrical contact between metal wires and nanoporous TiO_2 plays a dominating role in controlling the overall photovoltaic

performance. Passivating nature of Ti metal was confirmed in case of Cu & SS wires with improved performance of the devices. Coating of thin pure Ti metal over SS wire as surface passivating and electron recombination blocking layer led to the dramatic enhancement in the photoconversion efficiency from 1.12% (Ti) to 3.88% (SS/Ti). The same passivating effect of pure Ti thin layer on commercially available Ti wire confirms existence of impurities on Ti wire surface. Further the effect of irradiation area on the device performance was also investigated. In this context, gap between the wires were varied and it was found that even with spacing around 100 μm the devices were showing nearly the similar performance for approximately same active area. However, when the wrapped wire area was increased it caused an increase of the resistance hence lowered the FF. Since metal wires are highly conducting in nature, they are working as current collecting grids also which led to approximately same PCE for the device with small wrapped area.

References

1. Mathew, S., Yella, A., Gao, P., Humphry-Baker, R., Curchod, B. F., Ashari-Astani, N., ... & Grätzel, M. (2014). Dye-sensitized solar cells with 13% efficiency achieved through the molecular engineering of porphyrin sensitizers. *Nature chemistry*, *6*(3), 242-247.
2. O'regan, B., & Grätzel, M. (1991). A low-cost, high-efficiency solar cell based on dye-sensitized colloidal TiO_2 films.
3. Grätzel, M. (2006). The advent of mesoscopic injection solar cells. *Progress in Photovoltaics: Research and Applications*, *14*(5), 429-442.
4. Ye, M., Wen, X., Wang, M., Iocozzia, J., Zhang, N., Lin, C., & Lin, Z. (2014). Recent advances in dye-sensitized solar cells: from photoanodes, sensitizers and electrolytes to counter electrodes. *Materials Today*.
5. Kashiwa, Y., Yoshida, Y., & Hayase, S. (2008). All-metal-electrode-type dye sensitized solar cells (transparent conductive oxide-less dye sensitized solar cell) consisting of thick and porous Ti electrode with straight pores. *Applied Physics Letters*, *92*(3), 033308-033308.
6. Fan, X., Chu, Z. Z., Wang, F. Z., Zhang, C., Chen, L., Tang, Y. W., & Zou, D. C. (2008). Wire-shaped flexible dye-sensitized solar cells. *Advanced Materials*, *20*(3), 592-595.

7. Onoda, K., Ngamsinlapasathian, S., Fujieda, T., & Yoshikawa, S. (2007). The superiority of Ti plate as the substrate of dye-sensitized solar cells. *Solar Energy Materials and Solar Cells*, *91*(13), 1176-1181.
8. Kapil, G., Ohara, J., Ogomi, Y., Pandey, S. S., Ma, T., & Hayase, S. (2014). Fabrication and characterization of coil type transparent conductive oxide-less cylindrical dye-sensitized solar cells. *RSC Advances*, *4*(44), 22959-22963.
9. Yoshida, Y., Pandey, S. S., Uzaki, K., Hayase, S., Kono, M., & Yamaguchi, Y. (2009). Transparent conductive oxide layer-less dye-sensitized solar cells consisting of floating electrode with gradient TiOx blocking layer. *Applied Physics Letters*, *94*(9), 093301.
10. Fuke, N., Fukui, A., Komiya, R., Islam, A., Chiba, Y., Yanagida, M., ... & Han, L. (2008). New approach to low-cost dye-sensitized solar cells with back contact electrodes. *Chemistry of Materials*, *20*(15), 4974-4979.
11. Beppu, T., Kashiwa, Y., Hayase, S., Kono, M., & Yamaguchi, Y. (2009). Transparent conductive oxide layer-less three dimensional dye sensitized solar cells: fabrication of ionic path in three dimensional Ti electrode. *Japanese Journal of Applied Physics*, *48*(6R), 061504.
12. Miyasaka, T., & Kijitori, Y. (2004). Low-temperature fabrication of dye-sensitized plastic electrodes by electrophoretic preparation of mesoporous TiO_2 layers. *Journal of the Electrochemical Society*, *151*(11), A1767-A1773.
13. Usagawa, J., Pandey, S. S., Ogomi, Y., Noguchi, S., Yamaguchi, Y., & Hayase, S. (2013). Transparent conductive oxide-less three-dimensional cylindrical dye-sensitized solar cell fabricated with flexible metal mesh electrode. *Progress in Photovoltaics: Research and Applications*, *21*(4), 517-524.
14. Yu, J., Wang, D., Huang, Y., Fan, X., Tang, X., Gao, C., ... & Wu, K. (2011). A cylindrical core-shell-like TiO_2 nanotube array anode for flexible fiber-type dye-sensitized solar cells. *Nanoscale Res Lett*, *6*, 94.
15. Liu, Y., Wang, H., Shen, H., & Chen, W. (2010). The 3-dimensional dye-sensitized solar cell and module based on all titanium substrates. *Applied Energy*, *87*(2), 436-441.
16. Fu, Y., Lv, Z., Wu, H., Hou, S., Cai, X., Wang, D., & Zou, D. (2012). Dye-sensitized solar cell tube. *Solar Energy Materials and Solar Cells*, *102*, 212-219.

17. Liu, Z., & Misra, M. (2010). Dye-sensitized photovoltaic wires using highly ordered TiO2 nanotube arrays. *Acs Nano*, *4*(4), 2196-2200.
18. Wang, Y., Liu, Y., Yang, H., Wang, H., Shen, H., Li, M., & Yan, J. (2010). An investigation of DNA-like structured dye-sensitized solar cells. *Current Applied Physics*, *10*(1), 119-123.
19. Sun, L., Zhang, S., & Wang, Q. (2014). Conformal Growth of Anodic Nanotubes for Dye-Sensitized Solar Cells: Part II. Nonplanar Electrode. *Journal of nanoscience and nanotechnology*, *14*(2), 2050-2064.
20. Pops, H. (2008). Processing of wire from antiquity to the future. *Wire journal international*, *41*(6), 58-66.
21. Donachie, M. J. (2000). *Titanium: a technical guide*. ASM international.
22. http://www.azom.com/article.aspx?ArticleID=863 <accessed on 22/04/2015>
23. Fabregat-Santiago, F., Bisquert, J., Palomares, E., Otero, L., Kuang, D., Zakeeruddin, S. M., & Grätzel, M. (2007). Correlation between photovoltaic performance and impedance spectroscopy of dye-sensitized solar cells based on ionic liquids. *The Journal of Physical Chemistry C*, *111*(17), 6550-6560.
24. Kern, R., Sastrawan, R., Ferber, J., Stangl, R., & Luther, J. (2002). Modeling and interpretation of electrical impedance spectra of dye solar cells operated under open-circuit conditions. *Electrochimica Acta*, *47*(26), 4213-4225.
25. Yoshida, Y., Tokashiki, S., Kubota, K., Shiratuchi, R., Yamaguchi, Y., Kono, M., & Hayase, S. (2008). Increase in photovoltaic performances of dye-sensitized solar cells—Modification of interface between TiO_2 nano-porous layers and F-doped SnO_2 layers. *Solar Energy Materials and Solar Cells*, *92*(6), 646-650.
26. Choi, H., Nahm, C., Kim, J., Moon, J., Nam, S., Jung, D. R., & Park, B. (2012). The effect of $TiCl_4$-treated TiO_2 compact layer on the performance of dye-sensitized solar cell. *Current Applied Physics*, *12*(3), 737-741.
27. Wang, Q., Moser, J. E., & Grätzel, M. (2005). Electrochemical impedance spectroscopic analysis of dye-sensitized solar cells. *The Journal of Physical Chemistry B*, *109*(31), 14945-14953.

28. Kim, M., You, I. K., Lee, K. W., Lee, I. H., & Yun, H. G. (2013). Electrochemical analysis of transparent oxide-less photovoltaic cell with perforation patterned metal substrate. *Applied Physics Letters*, *102*(18), 183904.
29. An, J., Guo, W., & Ma, T. (2012). Enhanced Photoconversion Efficiency of All-Flexible Dye-Sensitized Solar Cells Based on a Ti Substrate with TiO_2 Nanoforest Underlayer. *Small*, *8*(22), 3427-3431.

CHAPTER4: INVESTIGATION OF TI WIRE BASED TCO-LESS CYLINDRICAL SOLAR CELLS

4.1 Introduction

Ever increasing world population, standard of human life and depleting precious fossil fuel reserves compel us to look for immense solar energy harvesting to meet with the huge future energy demands. Solar cells are one of the potential means to harness this solar energy directly in to usable electrical energy. Major part of current solar cell industry depends mainly on solid-state devices prepared from silicon and compound semiconductors. However, due to high cost of fabrication and high purity requirement limited its growth as compared to fossil fuels. Next generation solar cells based on mesoscopic titanium oxide (TiO_2) due to its high chemical stability, nontoxicity, low cost and corrosion resistance is one of the attractive alternatives to silicon photovoltaics and is the heart of dye-sensitized solar cells (DSSCs) [1]. In conventional DSSC the nanoporous TiO_2 is coated over the transparent conducting oxide (TCO) layer to form the scaffold for the dye adsorption [2]. Replacement of this TCO by other conducting substrates such as metal mesh, metallic foil and metallic wires [3-6] further reduces the DSSC fabrication cost and makes it not only a strong contender for silicon photovoltaics but gives the flexibility towards the roll-to-roll mass production also. Metallic titanium (Ti) substrates are used preferably for flexible DSSC with high-temperature sintered TiO_2 due to their low resistance, good flexibility, superior corrosion resistance and high temperature tolerance [7]. In this context, we have directed our efforts to combine the cylindrical device architecture with metal mesh and metal wire based photoanodes to fabricate TCO-less cylindrical DSSCs [8, 9]. Such a device structure offer advantages such as uniform solar harvesting throughout the day, high total output power in a day, less implication of wind and easy installation leading to low cost modules. In such metallic substrate based photoanode, facile electron transfer from TiO_2 to the conducting surface is one of the major controlling factors to achieve high power conversion efficiency (PCE). To improve this electron transfer process, great deal of the attempts such as introduction of interfacial layers on the Ti and stainless steel (SS) foils [10-15] have been made in order to provide a better binding force to the TiO_2 nanoparticle and smooth untreated metallic substrates.

Yun et. al. [10] discussed the importance of the substrate roughness and its effect on DSSC performance. In the DSSC research, interfacial surface passivation has been extensively investigated for the TCO and metal foil substrates, with only few reports on metallic wires [11, 12]. In our previously reported metal wire based novel cylindrical TCO-less DSSC (C-DSSC), [9] we discussed its advantages over the previous cylindrical architectures and the effect of different metal wire characteristics on the solar cell performance. It was realized that Ti wire is preferable over other metal wires owing to its less reactivity towards the ingredients of the redox electrolyte which is associated with the stability/durability of the DSSCs. However, use of the Ti wire to fabricate cylindrical photoanodes led to relatively poor photovoltaic performance as compared to the C-DSSCs based on stainless steel metal wires as discussed in the previous chapter. This could be attributed to the nature and surface properties of Ti-wires since Ti metal is reported to the form the surface oxide impurities [14, 15]. In this chapter, therefore, attempts have been directed to have the insight about change of Ti wire surface properties with the surface treatment and diameter variation, which directly affects the solar cell performance. This investigation shows the use of electrochemical impedance spectroscopy for getting optimum Ti wire diameter in order to enhance the C-DSSC performance. The X-ray diffraction (XRD), scanning electron microscope (SEM) and X-ray photoelectron spectroscopy (XPS) analyses were also conducted to have further insight about the surface properties.

4.2 Experimental

Fabrication of Pt counter electrode

A glass tube of diameter (ø=7 mm) was utilized for the fabrication of counter electrode. The glass tube was cut into the desired lengths for the C-DSSC fabrication. Proper washing of the tube was done with the detergent solution and water along with sonication for 10 minutes. The process was similarly followed by washing with acetone and isopropanol. After this UV-Ozone surface treatment (Filgen, Ozone killer, UV-253) was done to totally remove the organic surface contaminants. Thin titanium (240 nm) layer was then sputtered on the cleaned glass surface at the rate of 6 nm/min for 10 minutes followed by platinum sputtering at the same rate for 40 minutes. Coating of Ti before Pt layer was conducted in order to provide adherence of catalytic

Pt layer on the glass tube. The glass tube thus obtained finally was utilized as cylindrical counter electrode.

Fabrication of Photoanode

The metallic wires utilized for working electrode were commercially available titanium wire having diameters of 57 µm, 100 µm and 150 µm (Nilaco, Japan). The schematic device architecture of C-DSSC fabricated for the present investigation is shown in Figure 1. A 20 µm thick glass mesh (Asahi glass Co. Japan) was first wrapped over the Pt coated cylindrical glass tube serving as counter electrode which provides insulating separation between counter and working electrodes. Ti wire was then wrapped over the glass mesh holding it tightly. Nanoporous TiO_2 layer was then coated over the wrapped wires and the whole structure thus prepared was subjected for baking inside the electric furnace (Muffle Furnace F0300, Yamato, Japan). Gradual heating of the TiO_2 coated wire from room temperature to 450^0C for 1 hour followed by heating at this temperature for 30 min formed nanoporous TiO_2 scaffold. This was then allowed to cool down to 100^0C and sensitized with the *cis*-bis-(isothiocyanato) bis(2,2'-bypyridyl-4,4'-dicarboxylato) ruthenium(II) bis-tetrabutyl ammonium (Solaronix SA, Ruthenium 535-bisTBA

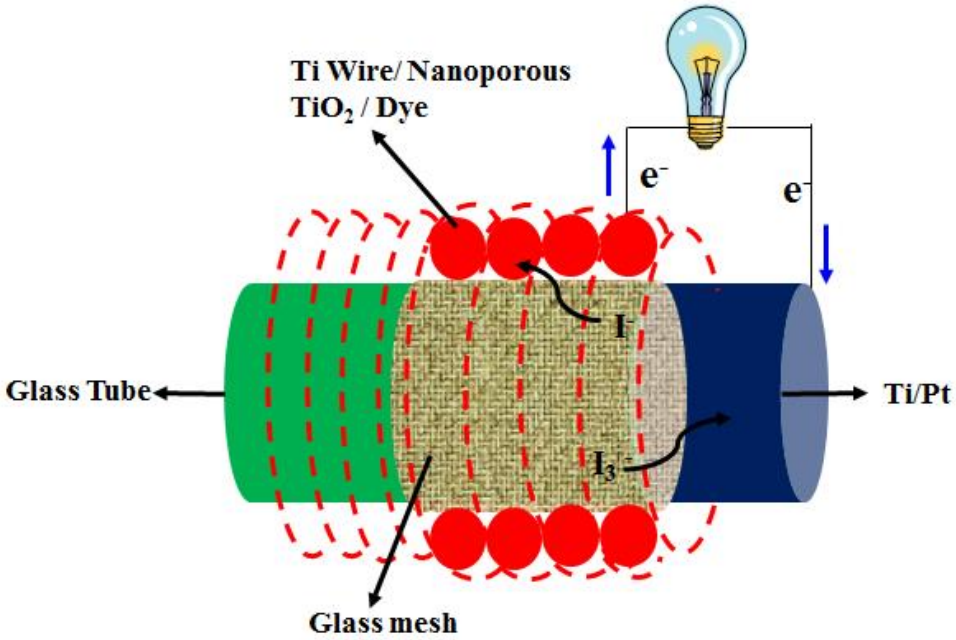

Figure 1. Schematic representation of device architecture and electron transport in TCO-less C-DSSC [25].

abbreviated as N719) from its 0.3 mM solution in t-butyl alcohol and acetonitrile (1:1 V/V) for 24 hours at the room temperature to form the TCO-less cylindrical photoanodes.

Ti wire surface treatment

The as-received Ti wires were rubbed properly using the emery paper and washed with isopropanol to remove the surface impurities. The Ti wires were then dipped in to the hydrogen peroxide solution (H_2O_2, 30 weight %) at 95^0C for 30 min for surface treatment. These wires were then heated gradually from room temperature to 450^0C in 1 hour and kept at this temperature for 30 min. The wires thus utilized for C-DSSC fabrication were as-received Ti wire with diameter 57 µm (Ti_57NT), rubbed Ti wires Ti_57, Ti_100, Ti_150 with diameter 57 µm, 100 µm, 150 µm, respectively along with their respective H_2O_2 treated counterparts represented as Ti_57HP, Ti_100HP and Ti_150HP.

Coil DSSC assembly

This is the final step in C-DSSC fabrication. The photoanodes thus obtained were inserted into a heat shrinkable tube (ø=9.5 mm, JUNFLON NF090, Junkosha Inc., Japan). This tube shrinks from 9.5 mm to 7.3 mm after heating at 120^0C for 5 min forming a small gap at the ends. The electrolyte containing 50 mM iodine, 500 mM lithium iodide, 580 mM t-butylpyridine and 600 mM 1-ethyl-3-methylimidazolium dicynoamide in acetonitrile was finally filled from the ends and the whole structure was sealed by epoxy resin.

Photovoltaic measurements

Photovoltaic measurements were carried out using solar simulator (KHP-1, Bunko-Keiki, Japan) equipped with a xenon lamp (XLS-150A) with the irradiation power of 100 mW/cm^2. The solar simulator spectrum and its power was adjusted using a spectroradiometer (LS-100, Eiko Seiki, Japan). The power of the incident light was also corrected using standard amorphous Si photo detector (BS-520 S/N 007, Bunko-Keiki, Japan). Area of irradiation was kept same for all of the C-DSSCs (0.1 cm^2), which is equal to the multiplication of width of the wire wrapped and the diameter of counter electrode. The photovoltaic characteristics were measured without any mask and whole device was exposed to the simulated light source. Incident photon to current conversion efficiency (IPCE) was measured with a constant photon flux of 1 x 10^{16} photon per

cm^2 at each wavelength in the direct current mode using the action spectrum measurement system connected to the solar simulator (CEP-2000, Bunko Keiki, Japan).

Electrochemical Impedance Spectroscopy

Electrochemical impedance spectroscopic (EIS) measurements were carried out using electrochemical interface (Solartron 1287) and frequency response analyzer (Solartron 1255B) connected to solar simulator (Yamashita Denso YSS-50A). The measurement was performed in the frequency range of 10^{-3} to 10^5 Hz at room temperature. Impedance spectra were measured by applying a DC bias at constant current of 1 mA cm^{-2} and AC voltage with an amplitude of 10 mV. Z-View software (Solartron Analytical) was utilized for analysis of electrical impedance spectra.

Surface analysis and dye loading test

The surface morphology of the Ti wires was observed through scanning electron microscope (SEM) (JEOL, Neoscope JCM-6000). X-Ray diffraction analysis (RINT-Ultima III, Rigaku, Japan) was performed in the range 20^0 to 90^0 for all the wires utilized for device fabrication. X-Ray photoelectron spectroscopy (XPS) (Axis-His/Kratos, Shimadzu) was carried out on the Ti wires for having the further insight about the surface states of Ti. The amount of dye loading was evaluated by desorbing the adsorbed dye on the nanoporous TiO_2 from solution consisting of equal volumes of NaOH (0.1 M), ethanol, t-butyl alcohol and acetonitrile followed by quantitation using spectrophotometer.

4.3 Results and discussion

Figure 1 shows the working principle involved in C-DSSC which is similar to typical back contact TCO-less DSSCs. Sensitizing dye anchored to the TiO_2 nanoparticles of the cylindrical TCO-less photoanodes absorbs the sun light (photons). This leads to photo-induced electron injection from excited dye molecules to the TiO_2 conduction band which travels to the Ti wire and finally to external circuit. The hole created at the dye ground state is filled by electron donation from I^- of I^-/I_3^- redox couple of the electrolyte producing I_3^-. I^- in turn is regenerated by reduction of I_3^- at the Pt counter electrode. Figure 2 exhibits the SEM surface micrographs of the

Ti wires utilized for the present work. The surface morphology of the Ti wire as-received was found to be changed exhibiting enhanced metallic luster after the mechanical polishing (Figure 2(a, b)). The surface impurities (TiO_x layer) which might be existing above the as-received wire surfaces due to oxidation of the Ti metal by environmental moisture, was etched after the

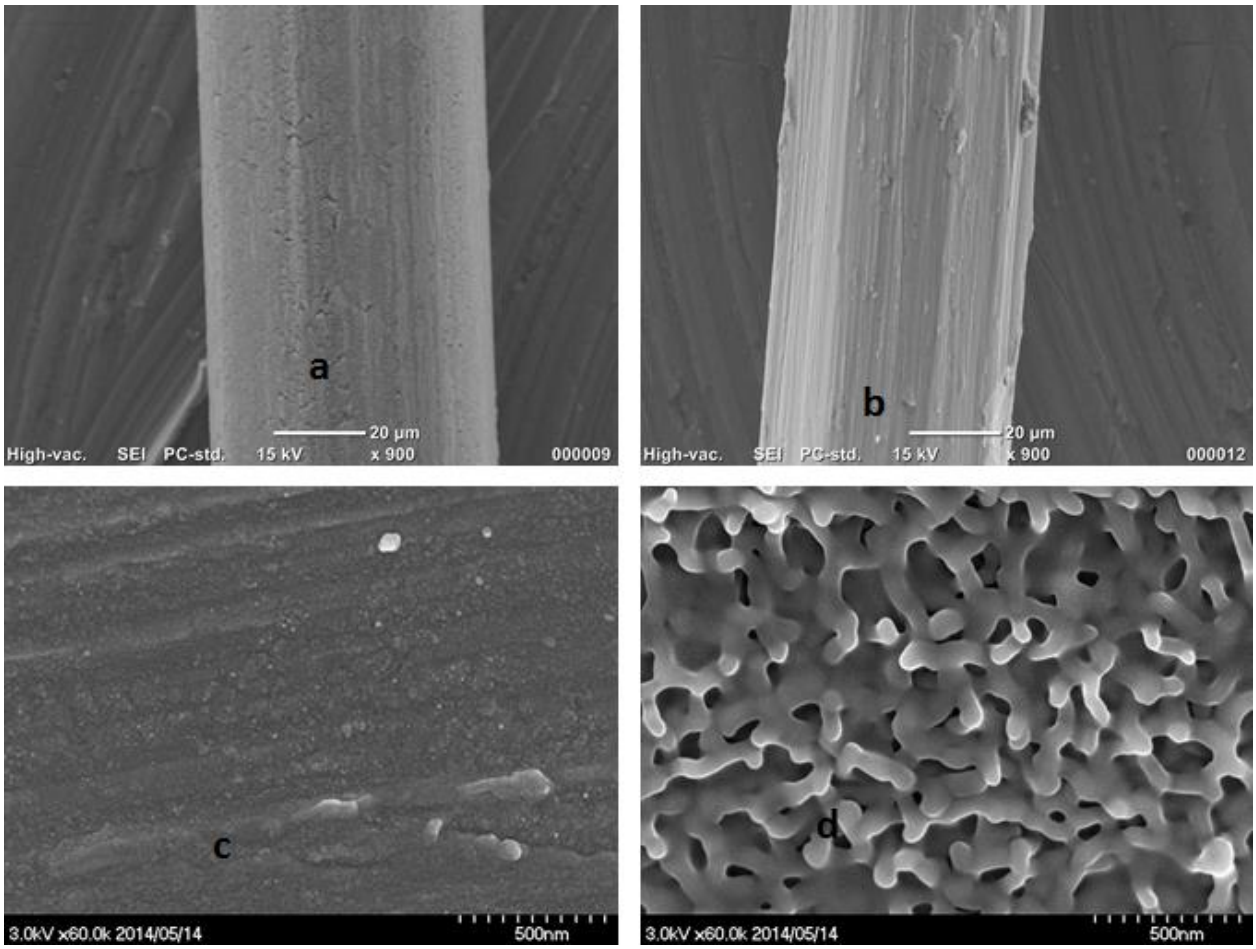

Figure 2. SEM images for Ti wires (a) as-received (b, c) after mechanical polishing and (d) after H_2O_2 surface treatment [25].

mechanical polishing of surface using emery paper. The noticeable difference between untreated Ti wire and H_2O_2 treated wire can be clearly as shown in Figure 2(c, d) with the formation of highly dense TiO_2 nanosheets due to the oxidation of metallic Ti by H_2O_2. A perusal of the Figure 2d corroborates that TiO_2 under layer formed have thickness of around 50 nm with spacing between the nanosheets in the range of 100-200 nm. Nanosheet formation is expected to

increase the specific area of Ti substrate because of its branched structure and improves the electrical contact between TiO_2 nanoparticles and the Ti wire substrate compared to untreated wire surface. Similar kind of observation pertaining to the TiO_2 nanosheet formation by the H_2O_2 oxidation of Ti-foil has been made by Tsai et al also [13].

In order to characterize surface properties of Ti-wires especially after the H_2O_2 surface treatment leading to nanosheet like surface morphology, XRD measurement was conducted for the mechanically polished Ti-wire before and after the H_2O_2 surface treatment. Figure 3 shows the typical XRD patterns consisting of characteristic peaks of Ti (JCPDS no. 44-1294) appearing at 2θ of about 35° (Ti-100), 38° (Ti-002), 40° (Ti-101) and 53° (Ti-102) [16]. Interestingly, upon H_2O_2 treatment additional peaks appearing at 2θ of 25.2° (A-101) and about 48° (A-200) are also

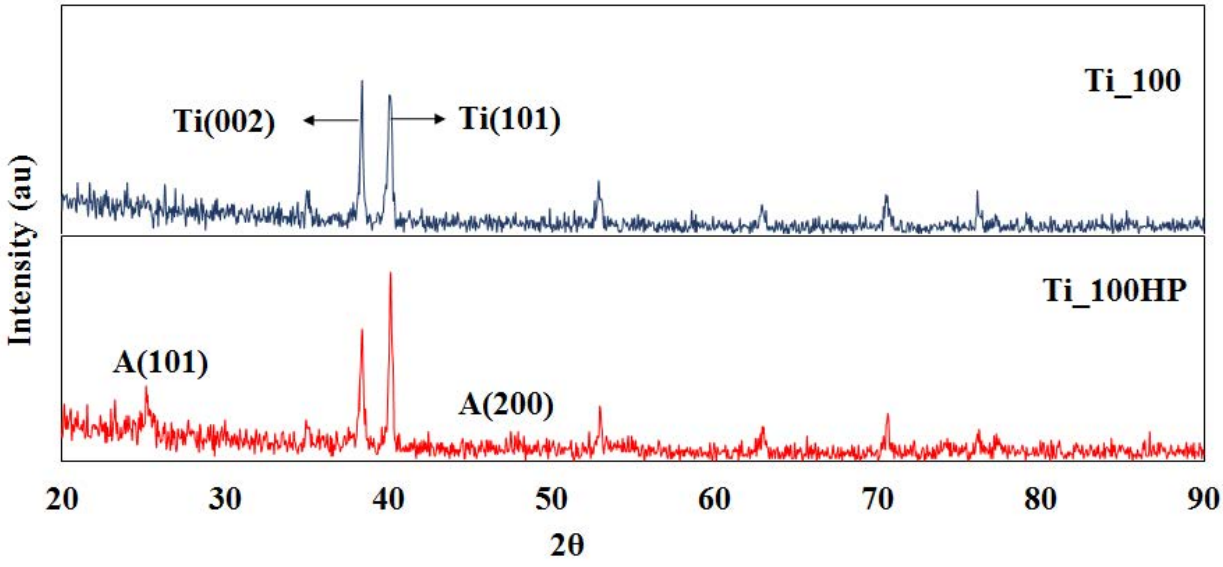

Figure 3. XRD patterns obtained for 100 μm thick mechanically polished Ti wire before (Ti_100) and after (Ti_100HP) H_2O_2 treatment. Ti and A refers to Titanium and anatase TiO_2, respectively [25].

observed which are not present in the untreated Ti-wire. These peaks have been assigned to be the Anatase TiO_2 as per the reference Anatase TiO_2 (JCPDS no 84-1286) reported previously [17]. Therefore, it can be concluded that the nanosheet like morphological features appearing after the H_2O_2 treatment are basically the Anatase TiO_2.

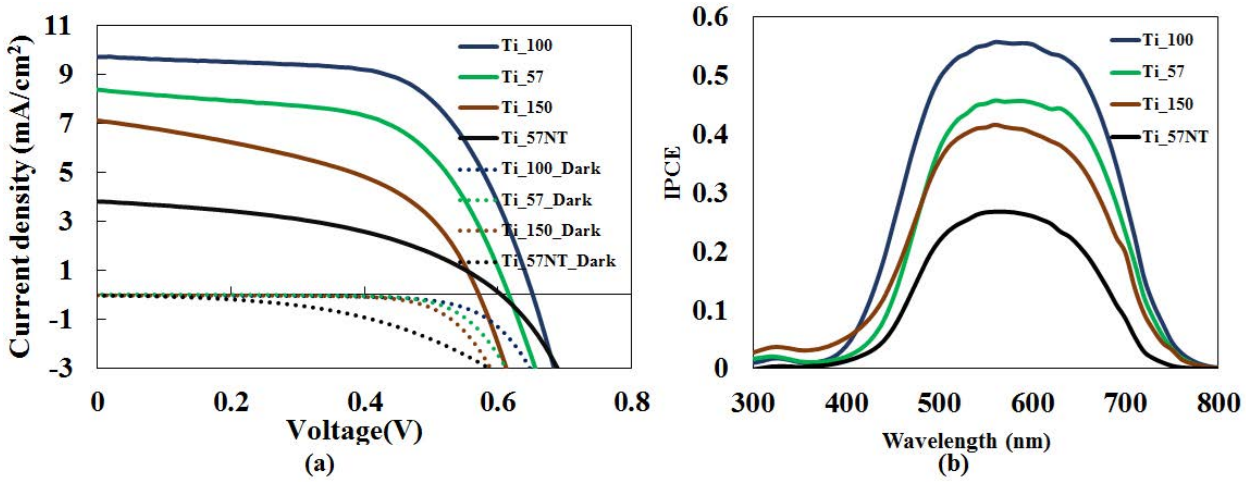

Figure 4. (a) Photo and dark current-voltage characteristics and (b) photocurrent action spectra for C-DSSCs based on photoanodes with Ti-wires of varying diameters [25].

Figure 4(a) shows the current-voltage (I-V) curves for the photoanodes fabricated using Ti wires with varying diameters utilized to fabricate C-DSSCs along with the photovoltaic parameters thus obtained shown in the Table 1. The solar cell based on 100 µm wire exhibited the best photovoltaic performance with a power conversion efficiency of 4.04%, which is much better than the photoanodes based on mechanically polished Ti-wires with diameters 57 µm (Ti_57~3.06%) and 150 µm (Ti_150~1.93%). At the same time, utilization of non-mechanically polished and as-received Ti-wire with diameter of 57 µm leads to much hampered photoconversion efficiency (Ti_57NT~1.03 %). From Table 1 it is clear that with the change in diameter of the wires there are changes in photovoltaic parameters. The high value of reverse saturation current for as-received Ti wire (Ti_NT) could be responsible for the lower short circuit current density (Jsc) of 3.82 mA/cm^2 and open circuit voltage (Voc) of (0.60 V) leading to lowest photoconversion efficiency. This might be associated with the surface impurities which are present on the wire surface (as TiO_x) seen through different SEM images obtained after polishing the surface in Figure 2(a, b). The surface impurity leads to poor adhesion and improper contact (necking) between coated nanoporous TiO_2 on the wire surface hindering the electron transport and enhancing the charge recombination. To explain the different Jsc values observed for cylindrical photoanodes based on Ti-wires with varying diameters, photocurrent action spectra (IPCE as function of wavelength) was also measured. The change in value of Jsc for these different photoanodes are in accordance with observed IPCE as shown in Figure 4(b). The

maximum value of IPCE was observed at the wavelength about 550 nm (absorption maximum for N-719 on TiO_2) demonstrating that the observed photocurrent is the result of photoexcited electron injection from the dye N-719 to the conduction band of TiO_2 followed by the electron transport.

Table 1 Photovoltaic and EIS parameters for C-DSSCs based on cylindrical photoanodes fabricated using Ti-wires of different diameters.

	Ti_57NT	**Ti_57**	**Ti_100**	**Ti_150**
Eff [%]	1.03	3.06	4.04	1.93
FF	0.45	0.59	0.64	0.47
Voc[V]	0.6	0.62	0.65	0.57
Jsc[mA/cm^2]	3.82	8.39	9.74	7.13
Dye loading (nmol/cm^2)	322.66	319.4	321.74	332.83
R1 (ohm)	25.97	24.94	14.48	12.48
R2 (ohm)	56.43	42.99	15.89	50.18
R3 (ohm)	2433	105.5	71.82	128.5

The differential behavior of observed Jsc for different photoanodes could be either due to different extent of recombination or contribution from extent of dye molecules attached on the nanoporous TiO_2 coated on the Ti-wire surfaces. To clarify these aspects, estimation of dye loading was performed, which indicates almost similar amount of dye adsorption for all of the four photoanodes as summarized in Table 1. Therefore, the differences in recombination could be one of the plausible explanations for the observed Jsc values as a function of wire diameter. A careful analysis of the Table 1 indicates that observed performance of solar cells are mainly controlled by fill factor (FF), which is directly affecting the solar cell efficiency. The reason for better fill factor of Ti_100 than Ti_57 could be due to decrease in resistance of Ti_100, which is contributed from increased cross-sectional area and less length of Ti_100 wire required for fabricating the same irradiation area (since resistance is directly proportional to length and

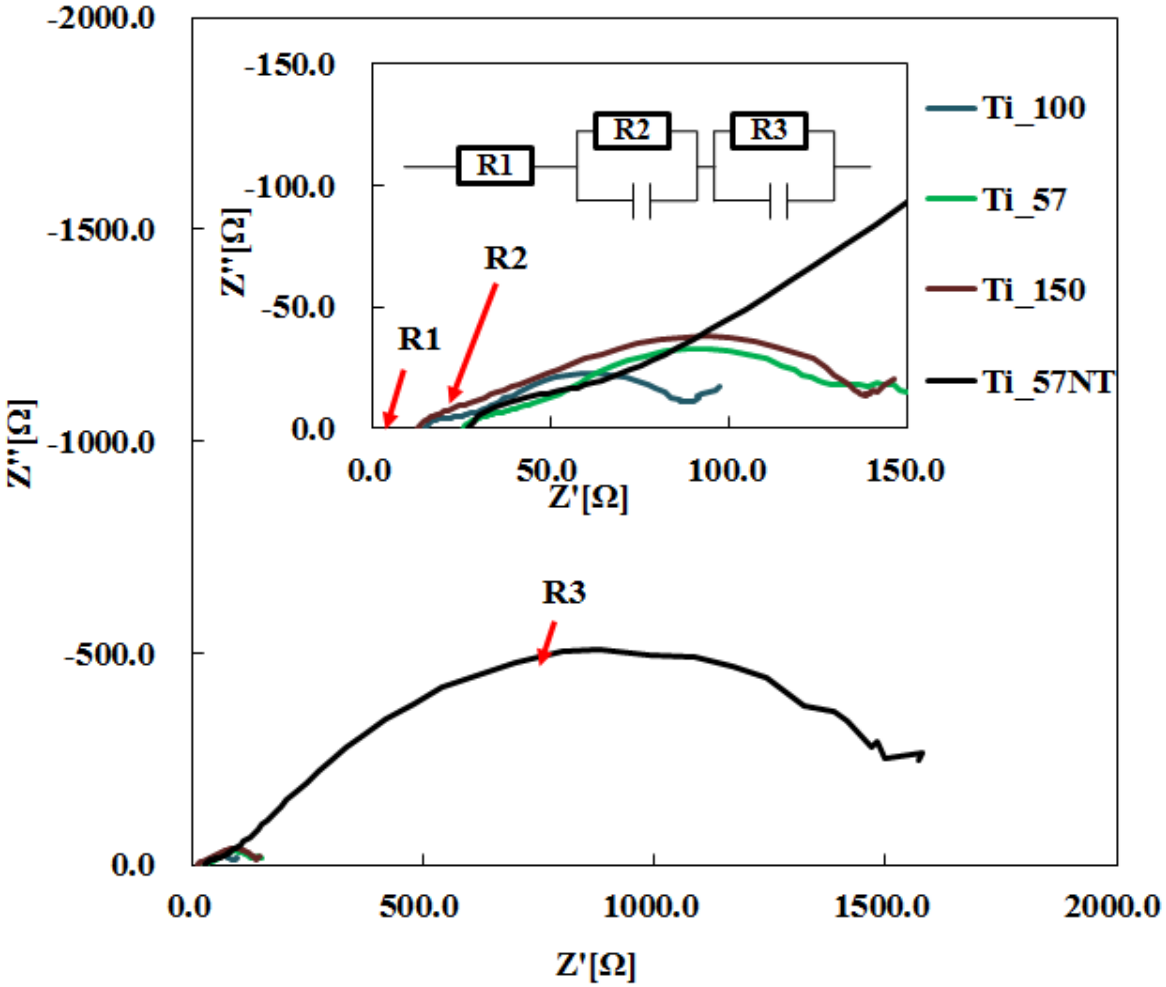

Figure 5. EIS spectra for C-DSSCs measured at AM 1.5 and constant Jsc of 1mA cm^{-2} [25].

inversely to cross sectional area). On the other hand, the same analogy seems not to be supported in case of Ti_150 and there might be some other reasons behind this. To have a further insight about differential behavior of FF for photoanodes based on Ti-wires of different diameters, EIS investigations were carried by plotting real verses imaginary part of complex electrical impedances (Nyquist plot) as shown in the Figure 5. There are mainly three resistances associated with C-DSSC as described in detail in our earlier publication [9].

These resistance have been estimated using equivalent circuit as shown in the inset of Figure 5 and are shown in the Table 1. Resistance R1 is associated with the series resistance of the solar cells and causes reduction in the FF and is due to the resistance of the wire working as current collecting substrate. From Table 1 it can be seen that the value R1 which is smaller for both of

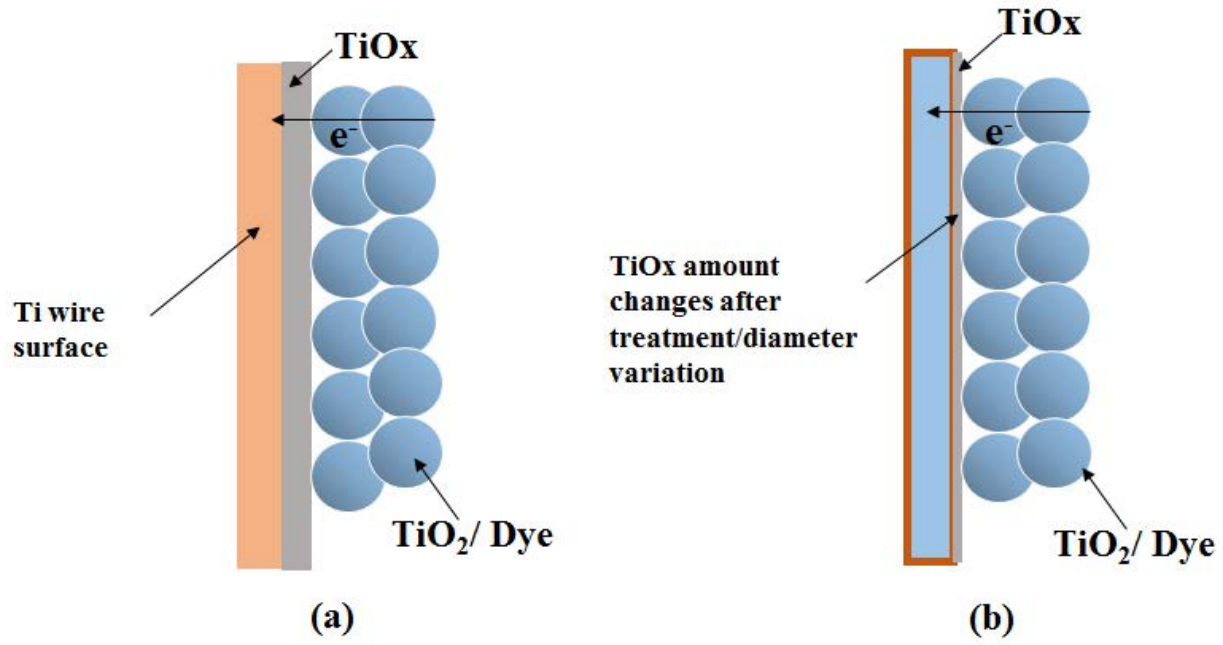

Figure 6. Schematic representation for implication of TiOx surface impurities on Ti wire surface resistance and electron transport with large (a) and small (b) TiOx layer [25].

Ti_150 (12.48 Ω) and Ti_100 (14.48 Ω) compared to Ti_57 (24.94 Ω), supports the order of FF for Ti_100 (0.64) > Ti_57 (0.59) but such trend seems not to be applicable for Ti_150 (0.47). It means the behavior of Ti_150 cannot be simply explained by only taking the series resistance of the wire in to consideration and their might be due to some other controlling factors. The second resistance element R2 is due to charge transfer at the counter electrode which does not provide conclusive information to explain the observed difference in C-DSSC performances since same counter electrode has been used for all the cases. The poor fill factor for Ti_150 (0.47) could be most probably attributed to the higher value of R3 (128.5 Ω) compared to 71.82 Ω and 105.5 Ω for Ti_100 and Ti_57, wires respectively. Origin of this R3 is associated with charge transfer resistance of working electrode/TiO_2 and TiO_2/electrolyte interfaces. High value of R3 is suggesting the poor electrical contact between coated nanoporous TiO_2 and the wire utilized for photoanode preparation [18, 19]. Similar high value of R3 (2433 Ω) is observed for Ti_57_NT with decreased FF. Therefore, the extent of adhesiveness between the nanoporous TiO_2 metallic substrate seems to play a dominant role towards controlling the FF as well as recombination in all the DSSC prepared from the coil based TCO-less photoanodes. It has been reported that

surface impurities like TiO_x adversely affect the proper electrical contact between the TiO_2 nanoparticle and substrate leading to hindered charge transport [14, 15]. Therefore, it can be thought that change in the diameter or surface treatment affect the extent of this available TiO_x surface impurities on the Ti-wires which controls the charge transport and affect the photovoltaic performance as shown in the Figure 4. This has been schematically shown in the Figure 6.

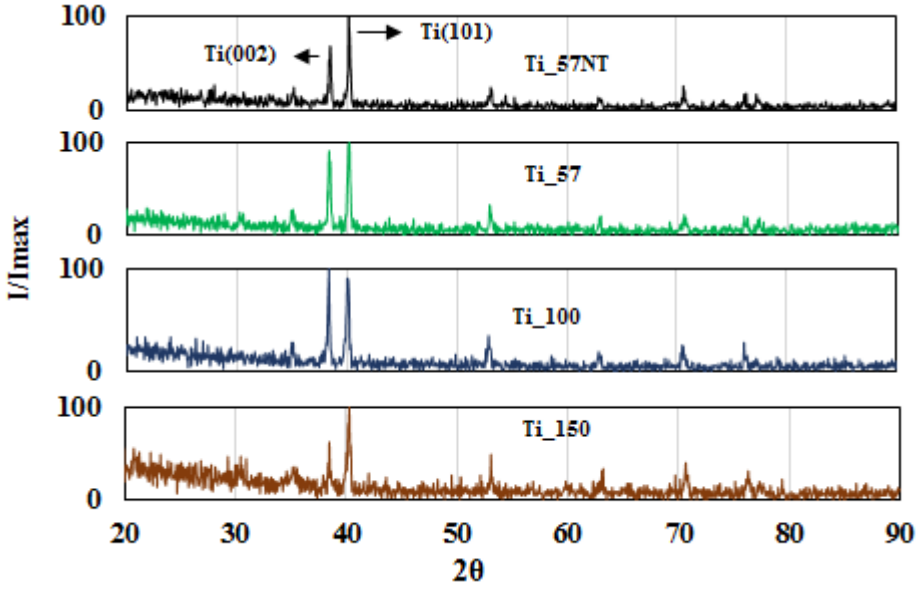

Figure 7. Normalized XRD pattern for Ti-wires with different diameters [25].

Variable amount of TiOx formation and impurity on the wires of different diameter was further analyzed using XRD investigations as shown in Figure 7. Ti_57 after mechanical polishing (Ti_57NT) exhibits relatively pure Ti surface which leads to increase in relative peak intensity of (002) as compared to (101). Relatively much decreased intensity of (002) peak for Ti_150 clearly indicates for the availability of largest amount of TiO_x when compared with Ti_57 and Ti_100, hence less pure Ti surface. Therefore, results pertaining to the differences in intensity of main (002) peak of pure sputtered Ti (Hexagonal closed packed phase) [20] relative to (101) peak conclude for differential amount of surface oxidized impurities or TiO_x on wire surface. Similar kind of observations has been made by Rajesh et al [21] for quantifying silver foil purity also using relative XRD peak intensities. Figure 8 shows the high-resolution XPS spectra of the Ti 2p peaks for Ti_100, Ti_150 and Ti_100HP to have a deeper insight about the formation of differential amount of TiO_x. The Ti $2p_{3/2}$ spin-orbital splitting photoelectrons for Ti_100HP is

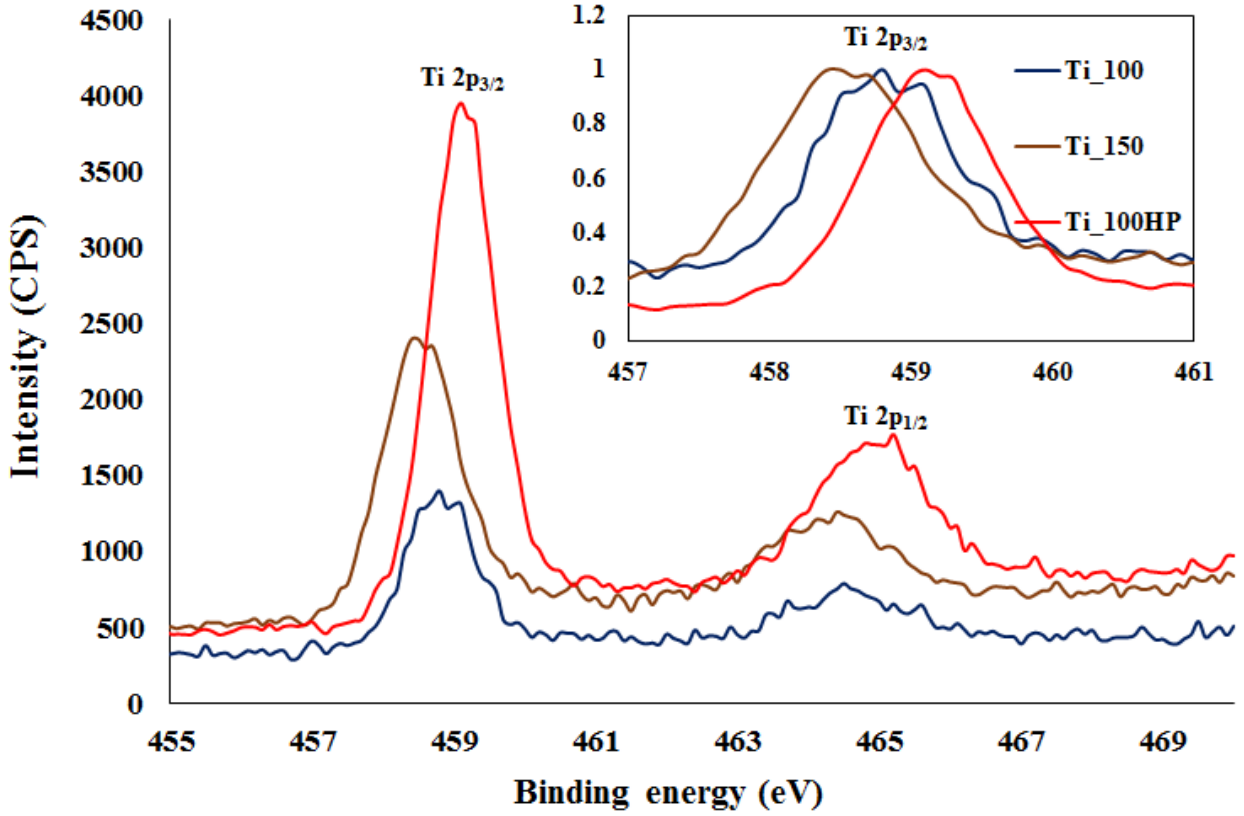

Figure 8. High-resolution XPS spectra of the Ti 2p peaks for Ti_100, Ti_150 and Ti_100HP [25].

located at 459.2 eV which is in agreement with the reported values for Anatase TiO_2 (Ti^{4+} normal state) [22]. It has been reported that spin-orbit splitting components are located in the range of 1-2 eV below the binding energy of Ti^{4+} (normal) state corresponding to the Ti^{2+} and Ti^{3+} states indicative of TiO_x formation [23]. In the case of Ti_100 it is shifted towards lower binding energy of 458.8 eV and with further increase in diameter to 150 µm wire (Ti_150) it exhibits even more down-shift at 458.5 eV clearly corroborating that Ti_150 surface is more prone to the formation of TiO_x compare to Ti_100. The observation that H_2O_2 surface treatment of Ti-wire leads to dramatic change in the surface morphological properties leading to generation of nanosheet like structure with enhanced surface area (Figure 2d) and they are basically the Anatase TiO_2 as confirmed by XRD results (Figure 3) prompted us to investigate their implication on photovoltaic behavior. The photovoltaic parameters for all of the H_2O_2 surface treated wires are summarized in the Table 2. It can be clearly seen that H_2O_2 treatment has favorable effect on improving the photovoltaic performance as compared to their respective un-

treated counterparts. The effect of H_2O_2 treatment is least for 57 µm (9.47 % increase in efficiency) and with the increase in diameter or surface area of wire the effect is more prominent and surprisingly most effective for 150 µm (58.03% increase in efficiency). However, due to large surface area and formation of relatively larger extent of TiO_x could be attributed to hinder towards the attainment of best solar cell efficiency using Ti_150HP as compared to Ti_57HP and Ti_100HP. Figure 9 exhibits the comparative photovoltaic characteristics for 100 µm Ti wire (Ti_100) based C-DSSC before and after the H_2O_2 treatment (Ti_100HP) for which we have observed the best photovoltaic performance. A perusal of this Figure 9(a) clearly corroborates

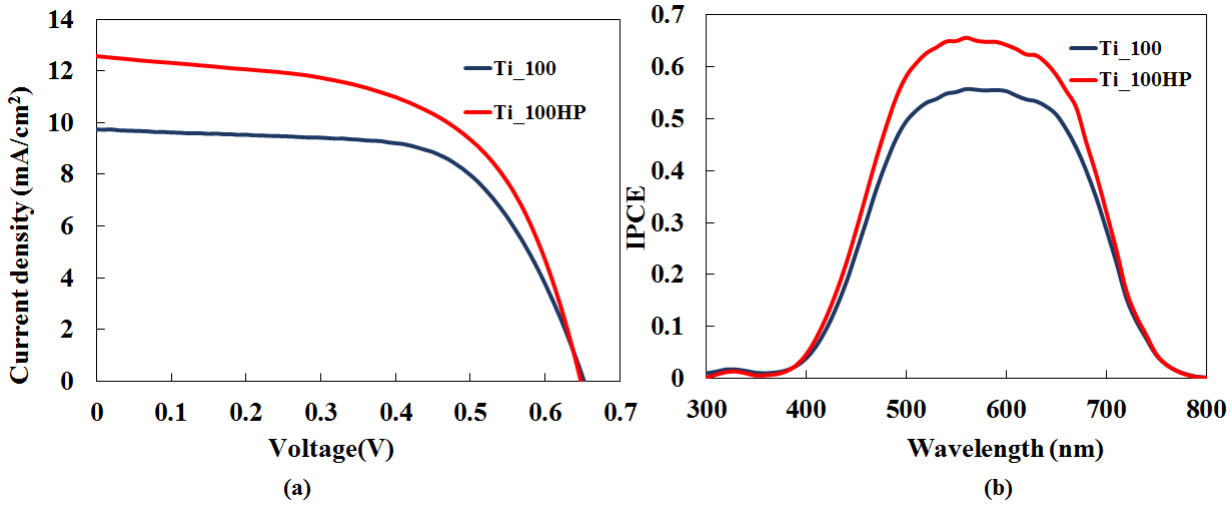

Figure 9. (a) Photovoltaic characteristics and (b) photocurrent action spectra for C-DSSC fabricated using 100 µm Ti-wire before and after the H_2O_2 surface treatment [25].

that Jsc is the main contributing factor for increased photoconversion efficiency of 4.71% from 4.04% since Voc and FF are not being affected appreciably. To explain the enhanced Jsc value observed for cylindrical coil based TCO-less photoanodes utilizing 100 µm Ti-wire before and after the H_2O_2 surface treatment, photocurrent action spectra was also measured as shown in the Figure 9(b). It can be seen that peak IPCE value have increased from around 55% to 65% at about 550 nm wavelength and is attributed to the enhanced Jsc of H_2O_2 treated Ti-wire. One of the possible reasons for the enhanced Jsc could be due to enhanced dye loading since wire surface area was found to be increased by Anatase TiO_2 nanosheet like microstructures which is in direct contact with the nanoporous TiO_2 layer utilized for the dye adsorption [24]. To confirm this assumption, extent of dye adsorption was also estimated and shown in the Table 2. Increase

in the dye loading from 321 (Ti_100) to 365 (Ti_100HP) nmol/cm^2 upon H_2O_2 surface treatment verifies the increase in Jsc and IPCE values.

Table 2 Photovoltaic parameters after H_2O_2 treatment on 57µm, 100µm and 150µm Ti wire based C-DSSC.

	Ti_57HP	**Ti_100HP**	**Ti_150HP**
Efficiency [%]	3.35	4.71	3.05
FF	0.51	0.58	0.65
Voc[V]	0.61	0.65	0.65
Jsc[mA/cm^2]	10.87	12.58	7.23
Dye loading (nmol/cm^2)	356.88	365	372.09

4.4 Conclusion:

In summary, it has been shown that surface properties of the Ti wires play an important role in controlling the performance of C-DSSCs. Investigations pertaining to the EIS revealed that extent of TiO_x surface impurities varies with the diameter of the wire which is responsible for the variable adhesion of coated nanoporous TiO_2 and Ti wires. It showed that TiO_2/dye/electrolyte interfacial charge transfer resistance was mainly affected by the diameter variation, which is maximum for untreated Ti_57NT wire due to large amount of surface impurity. This resistance is reduced to a comparatively less value after mechanical polishing of the wire surface. The variable amount of TiOx as function of wire diameter was further probed by XRD and XPS investigations also. Both investigations confirmed the existence of variable amount of TiOx on the different wire surfaces which was effecting our device performance. Solar cell performance first increased from 57 µm Ti wire to 100 µm and then decreased with further increase in diameter to 150 µm. C-DSSCs fabricated with photoanode utilizing mechanically polished Ti wire exhibited a considerable enhancement in solar cell efficiency from 1.03 % to 3.06 %. H_2O_2 surface treatment further improved the photoconversion efficiency from 4.04 % to 4.71%, which is due to the formation of Anatase (A-101) nanosheet like structures as confirmed by XRD and

XPS studies enhancing surface area and good contact assisting the enhanced dye loading and facile charge transport, respectively.

References:

1. Vlachopoulos, N., Liska, P., Augustynski, J., & Grätzel, M. (1988). Very efficient visible light energy harvesting and conversion by spectral sensitization of high surface area polycrystalline titanium dioxide films. *Journal of the American Chemical Society*, *110*(4), 1216-1220.
2. Ito, S., Murakami, T. N., Comte, P., Liska, P., Grätzel, C., Nazeeruddin, M. K., & Grätzel, M. (2008). Fabrication of thin film dye sensitized solar cells with solar to electric power conversion efficiency over 10%. *Thin solid films*,*516*(14), 4613-4619.
3. Kashiwa, Y., Yoshida, Y., & Hayase, S. (2008). All-metal-electrode-type dye sensitized solar cells (transparent conductive oxide-less dye sensitized solar cell) consisting of thick and porous Ti electrode with straight pores. *Applied Physics Letters*, *92*(3), 033308-033308.
4. Fan, X., Chu, Z. Z., Wang, F. Z., Zhang, C., Chen, L., Tang, Y. W., & Zou, D. C. (2008). Wire‐shaped flexible dye‐sensitized solar cells. *Advanced Materials*,*20*(3), 592-595.
5. Lv, Z., Fu, Y., Hou, S., Wang, D., Wu, H., Zhang, C., ... & Zou, D. (2011). Large size, high efficiency fiber-shaped dye-sensitized solar cells. *Physical Chemistry Chemical Physics*, *13*(21), 10076-10083.
6. Liu, Y., Wang, H., Shen, H., & Chen, W. (2010). The 3-dimensional dye-sensitized solar cell and module based on all titanium substrates. *Applied Energy*, *87*(2), 436-441.
7. Onoda, K., Ngamsinlapasathian, S., Fujieda, T., & Yoshikawa, S. (2007). The superiority of Ti plate as the substrate of dye-sensitized solar cells. *Solar Energy Materials and Solar Cells*, *91*(13), 1176-1181.
8. Usagawa, J., Pandey, S. S., Ogomi, Y., Noguchi, S., Yamaguchi, Y., & Hayase, S. (2013). Transparent conductive oxide‐less three‐dimensional cylindrical dye‐sensitized solar cell fabricated with flexible metal mesh electrode. *Progress in Photovoltaics: Research and Applications*, *21*(4), 517-524.
9. Kapil, G., Ohara, J., Ogomi, Y., Pandey, S. S., Ma, T., & Hayase, S. (2014). Fabrication and characterization of coil type transparent conductive oxide-less cylindrical dye-sensitized solar cells. *RSC Advances*, *4*(44), 22959-22963.

10. Yun, H. G., Jun, Y., Kim, J., Bae, B. S., & Kang, M. G. (2008). Effect of increased surface area of stainless steel substrates on the efficiency of dye-sensitized solar cells. *Applied physics letters*, *93*(13), 133311-133311.

11. Lv, Z., Yu, J., Wu, H., Shang, J., Wang, D., Hou, S., ... & Zou, D. (2012). Highly efficient and completely flexible fiber-shaped dye-sensitized solar cell based on TiO_2 nanotube array. *Nanoscale*, *4*(4), 1248-1253.

12. Yu, J., Wang, D., Huang, Y., Fan, X., Tang, X., Gao, C., ... & Wu, K. (2011). A cylindrical core-shell-like TiO_2 nanotube array anode for flexible fiber-type dye-sensitized solar cells. *Nanoscale Res Lett*, *6*, 94.

13. Tsai, T. Y., Chen, C. M., Cherng, S. J., & Suen, S. Y. (2013). An efficient titanium‐based photoanode for dye‐sensitized solar cell under back‐side illumination. *Progress in Photovoltaics: Research and Applications*, *21*(2), 226-231.

14. Lee, C. H., Chiu, W. H., Lee, K. M., Hsieh, W. F., & Wu, J. M. (2011). Improved performance of flexible dye-sensitized solar cells by introducing an interfacial layer on Ti substrates. *Journal of Materials Chemistry*, *21*(13), 5114-5119.

15. An, J., Guo, W., & Ma, T. (2012). Enhanced Photoconversion Efficiency of All‐Flexible Dye‐Sensitized Solar Cells Based on a Ti Substrate with TiO_2 Nanoforest Underlayer. *Small*, *8*(22), 3427-3431.

16. Lim, Y. C., Zainal, Z., Tan, W. T., & Hussein, M. Z. (2012). Anodization parameters influencing the growth of titania nanotubes and their photoelectrochemical response. *International Journal of Photoenergy*, *2012*.

17. Thamaphat, K., Limsuwan, P., & Ngotawornchai, B. (2008). Phase characterization of TiO2 powder by XRD and TEM. *Kasetsart J.(Nat. Sci.)*,*42*(5), 357-361.

18. Choi, H., Nahm, C., Kim, J., Moon, J., Nam, S., Jung, D. R., & Park, B. (2012). The effect of $TiCl_4$-treated TiO_2 compact layer on the performance of dye-sensitized solar cell. *Current Applied Physics*, *12*(3), 737-741.

19. Kim, M., You, I. K., Lee, K. W., Lee, I. H., & Yun, H. G. (2013). Electrochemical analysis of transparent oxide-less photovoltaic cell with perforation patterned metal substrate. *Applied Physics Letters*, *102*(18), 183904.

20. Arshi, N., Lu, J., Lee, C. G., Yoon, J. H., Koo, B. H., & Ahmed, F. (2013). Thickness effect on properties of titanium film deposited by dc magnetron sputtering and electron beam evaporation techniques. *Bulletin of Materials Science*, *36*(5), 807-812.

21. Rajesh, D., & Sunandana, C. S. (2012). Effect of etching on the optical properties of partially iodized commercial silver foils. *Indian Journal of Physics*, *86*(8), 681-686.

22. Erdem, B., Hunsicker, R. A., Simmons, G. W., Sudol, E. D., Dimonie, V. L., & El-Aasser, M. S. (2001). XPS and FTIR surface characterization of TiO_2 particles used in polymer encapsulation. *Langmuir*, *17*(9), 2664-2669.

23. Kumar, P. M., Badrinarayanan, S., & Sastry, M. (2000). Nanocrystalline TiO_2 studied by optical, FTIR and X-ray photoelectron spectroscopy: correlation to presence of surface states. *Thin Solid Films*, *358*(1), 122-130.

24. Ushiroda, S., Ruzycki, N., Lu, Y., Spitler, M. T., & Parkinson, B. A. (2005). Dye sensitization of the anatase (101) crystal surface by a series of dicarboxylated thiacyanine dyes. *Journal of the American Chemical Society*, *127*(14), 5158-5168.

25. Kapil, G., Pandey, S. S., Ogomi, Y., Ma, T., & Hayase, S. (2014). Titanium wire engineering and its effect on the performance of coil type cylindrical dye sensitized solar cells. *Organic Electronics*, 15(11), 3399-3405.

CHAPTER 5: INDOOR LIGHT APPLICATION OF COIL TYPE CYLINDRICAL DYE SENSITIZED SOLAR CELL UTILIZING REFLECTORS

5.1 INTRODUCTION

Dye-sensitized solar cells (DSSCs) have gained popularity among the researchers in the recent years because of the use of low-cost materials along with the possibility of fabricating upon flexible substrates [1-4]. Amongst the approaches adopted to fabricate flexible DSSCs, use of flexible photoanode as working electrode consisting of transparent conductive oxide (TCO) coated plastic films are most common [5]. This TCO layer is an expensive element and limits the DSSC for the mass level productions [6]. With the removal of this TCO and combining DSSC with the advantages of cylindrical geometry as reported in past [7, 8] led to fabrication of low cost DSSCs having the capability of light harvesting throughout the day. Another interesting area of application of DSSCs is to use it for the indoor lights under fluorescent or diffused light. This is the area where DSSCs can outperform inorganic materials based solar cell such as amorphous silicon based solar cell and Copper Indium Gallium Selenide (CIGS) solar cells [9]. We have already reported one of the fast and easy way to fabricate TCO-less DSSC based on titanium (Ti) wire as coil type cylindrical DSSC (C-DSSC) compatible to current incandescent lighting appliance production technology [7] using ruthenium (Ru) metal based N719 dye. The ruthenium metal is rare earth material and quite expensive [10]. Therefore, other alternatives to metal complex based dyes are organic dyes not using rare earth metals having vast possibility of molecular design [11, 12] has got a good deal of attentions inn the recent past. Apart from this, organic dyes exhibit high molar-extinction-coefficient which increases the light harvesting efficiency [13] even in thin films having their potentiality in the solid-state DSSCs fabrication.

Absorption spectra of the dyes play an important role in controlling the performance of the DSSC under white light as well as fluorescent light illuminations [10, 15]. Performance of the cylindrical DSSC under white light and diffused light has been studied by Fu et al with emphasis on improving the output power in presence of different reflector geometries such as parabolic, semi-elliptical, V-groove and semi-circular advocating the superiority of the parabolic reflectors [14]. In this chapter, investigation pertaining to the evaluation of performance of

TCO-less C-DSSCs under low intensity fluorescent light illumination using commercially available ruthenium based N719 and organic dyes such as D205 and Y-123 have been made. Results of electrochemical impedance spectroscopy (EIS) are discussed to explain the differential solar cell performances. Therefore, we have used parabolic reflectors combined with C-DSSC fabricated using different sensitizing dye to investigate their performance under low intensity fluorescent light illumination. The solar cell performances in the presence and absence of parabolic reflector was also measured and compared.

5.2 EXPERIMENTAL

Device fabrication Figure 1 shows the schematic diagram for the cross sectional view of C-DSSC fabricated in this work. Fabrication steps are explained in detail elsewhere [8]. Ti-wire with 100 µm diameter used as working electrode was wrapped in the shape of a coil. The TiO_2 layers coated on the wrapped metallic wires after sintering at 450ºC were subjected to absorption with the three sensitizing dyes (N719, D205 and Y123) having structure as shown in the Figure 2. The dye bath solution for the dye adsorption on the nanoporous TiO_2 was consisted of N719 (0.3 mM) in t-butyl alcohol and acetonitrile (1:1 V/V), D205 (0.5 mM) in t-butyl alcohol and

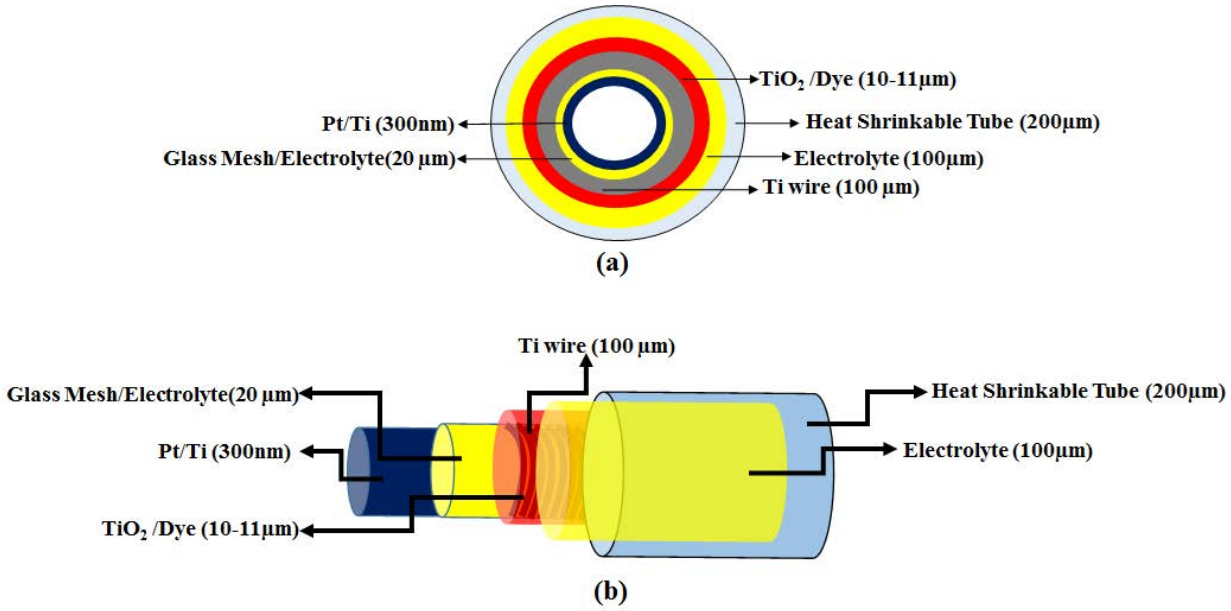

Figure 1. (a) Vertical Cross-sectional view of the C-DSSC (b) C-DSSC with the thickness of different elements used

acetonitrile (1:1 V/V) and Y-123 (0.1 mM) in ethanol. The dye adsorption time for N719, D205 and Y-123 was 24 hours, 4 hours and 16 hours, respectively. Electrolyte with 50 mM Iodine, 500 mM lithium iodide, 580 mM t-butylpyridine and 600 mM 1-ethyl-3methylimidazolium dicyanamide in acetonitrile was used. Different concentrations of iodine such as 10 mM and 0.1mM were also further utilized for the C-DSSC performance analysis under varying Iodine concentration.

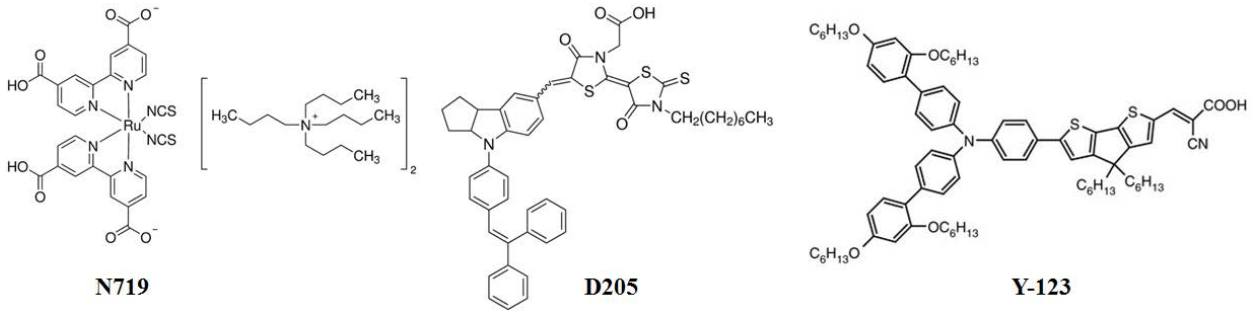

Figure 2 Molecular structure of the dyes used in this work.

Current-voltage (I-V) measurements and experimental setup

The measurements were done using solar simulator (KHP-1, Bunko-Keiki, Japan). For 1 SUN and diffused light measurements a xenon lamp (XLS-150A) was utilized. Fluorescent lamps were also used for indoor light study of the C-DSSC performance. The intensities used were around 0.2 mW/cm^2, 0.3 mW/cm^2, 0.4 mW/cm^2 and 0.5 mW/cm^2 (Toshiba ,Japan). Figure 3 shows the experimental setup utilized for the measurement using the parabolic reflectors. The parabolic geometry leads to maximum power input at the focus point as drawn in Figure 3(d). Therefore, for the best performances of C-DSSC measurements were done at focus point of the reflector. A reflecting film (Alanod solar, Miro-Sun, KK, Germany) was pasted on a parabolic surface designed using 3D printer to make the parabolic reflectors as shown in Figure 4. Different parabolic reflectors of equation such as 1/10 X^2, 1/20X^2 and 1/40 X^2 were used as shown in Figure 3(c).

Overview of Trace Pro 7.5.1(Used for simulation study) Trace Pro 7.5.1 program designs the various optical systems. It traces the rays to calculate the illumination distributions throughout the system. Models in the program are created by importing lens design from CAD files, or

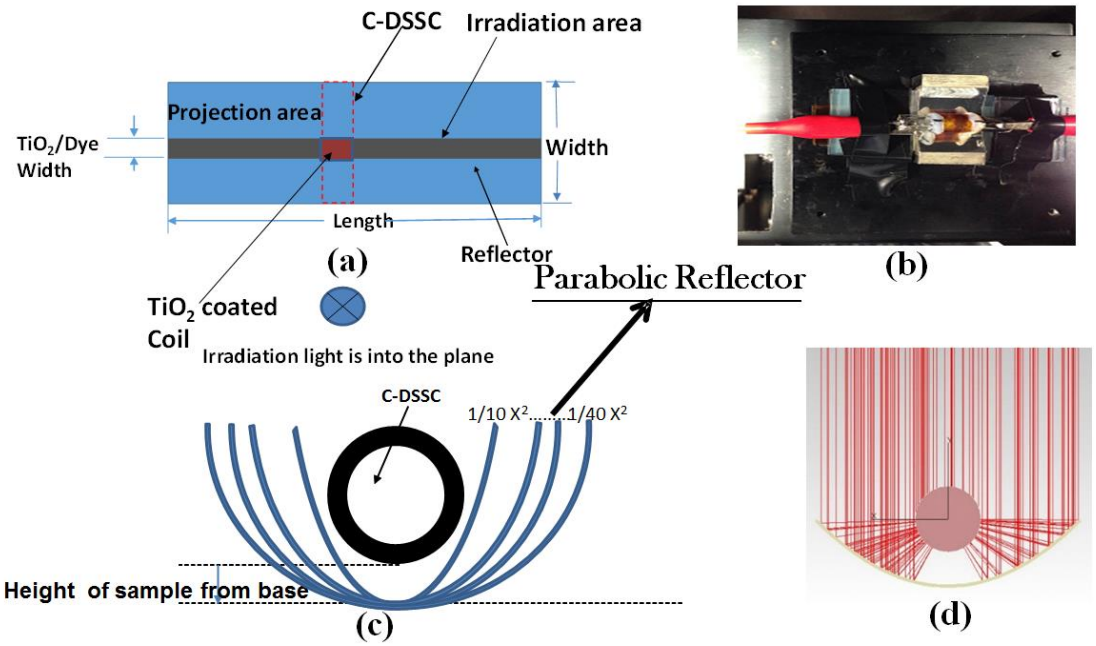

Figure 3. (a) Area of irradiation when reflector was used (b) Top view for the measurement done (c) Different reflectors used (d) Schematic showing the rays goes to focus after reflection

Figure 4. Reflectors used in the experiment

directly creating solid geometry within it. In the current study, we modeled our C-DSSC while adding the optical properties of the elements above mesoporous TiO_2 for checking the input power distribution on the TiO_2 surface. Different equation based parabolic reflectors were also modeled. The parameters for spectral irradiation of 1 SUN and fluorescent lamps were added for simulating the light sources. Both parallel and spherical sources were simulated for the study.

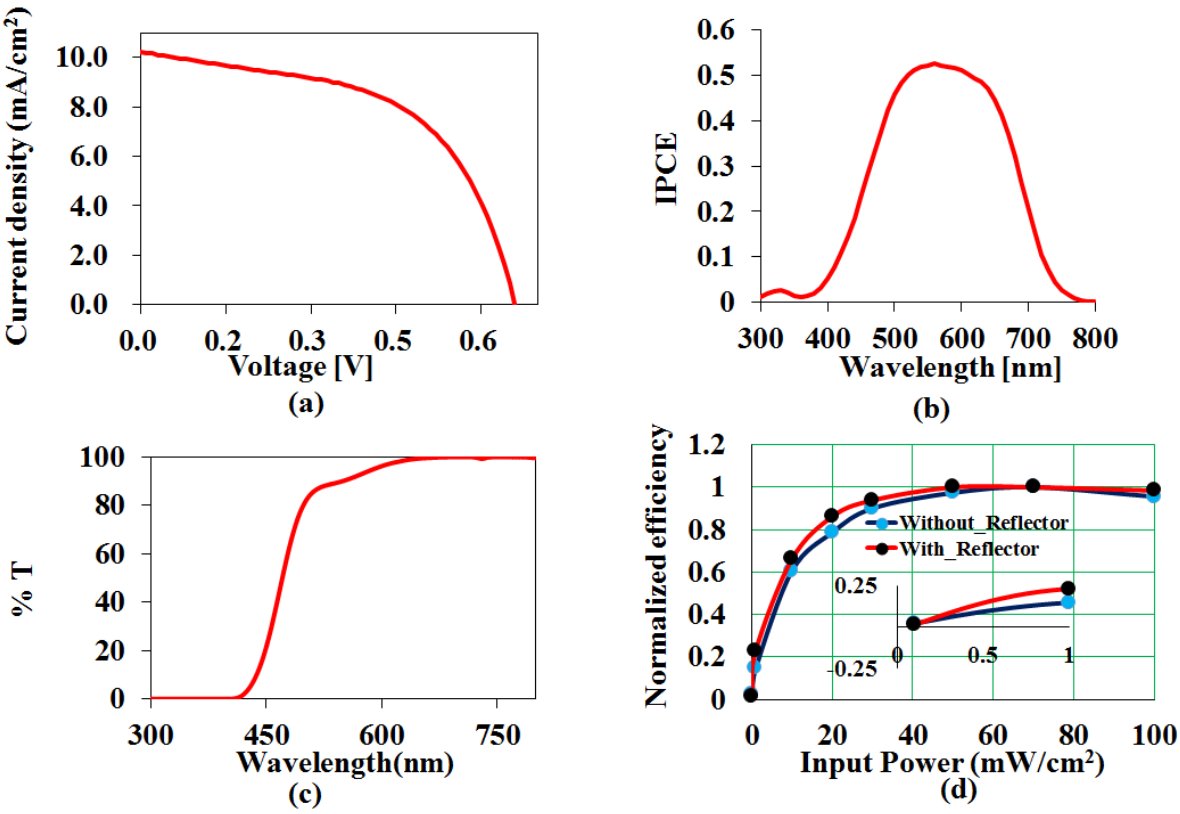

Figure 5 (a) Current-voltage characteristic of the C-DSSC (b) IPCE of the cell (c) Transmission of the electrolyte layer (d) white light performance of the cell with and without reflector at different intensities

5.3 RESULTS AND DISCUSSION

5.3.1 White light performance using N719 dye

The typical current-voltage (I-V) characteristic for the optimized C-DSSC fabricated is shown in Figure 5(a).The electrical parameters like short circuit current density (Jsc) =10.24 mA/cm^2, open-circuit voltage (Voc) = 0.66 and fill factor (FF) =0.54 were obtained for this C-DSSC leading the power conversion efficiency of 3.68%. This performance was obtained under white light illumination intensity of AM 1.5 (100 mWcm^2) without any mask. The area of irradiation taken to calculate short circuit current density (Jsc) and efficiency is the width of TiO_2 coated on the wires multiplied with the diameter of the glass tube used, which is commonly adopted by other research groups also [14]. Figure 5(b) shows the incident photon to current conversion efficiency (IPCE) which is up to 50% with maximum at around 550 nm (absorption peak for N719 dye). Low IPCE in the wavelength region of 300-400 nm is due to the absorption by the

iodine electrolyte in this region. This can also be clearly seen in Figure 5(c), which shows the transmission spectra of the electrolyte as it goes down to zero transmission value just below 450 nm. Figure 5(d) gives the change in the normalized efficiency with and without reflector, which shows better performance using the reflector especially at intensities below 1 mW/cm^2. This low intensity region is an important region for application of DSSCs compared to inorganic solar cells [9].

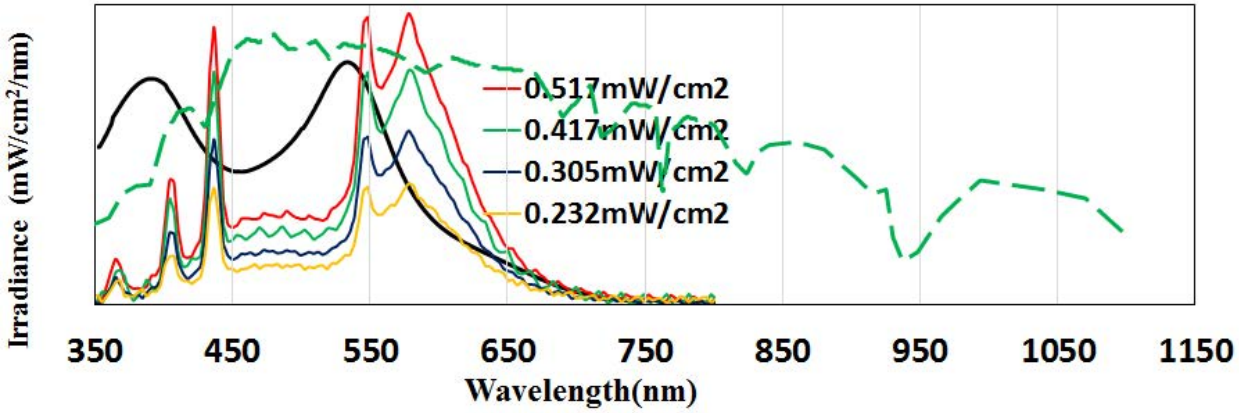

Figure 6. Spectral distribution for 1 SUN (dash green color), Fluorescent lamps with different intensities and absorption spectra for N719 dye (solid line in black)

Figure 6 shows spectral irradiation distribution of AM 1.5 sunlight and fluorescent lamps along with the absorption spectra for N719 attached to the TiO_2 surface. It clearly shows that there is far better spectral matching between absorption of N719 and fluorescent lamp light in the range of 350-750 nm compared to that of white light (intensities are in arbitrary unit).This matching plays the main role for the better PCE of DSSCs compared to inorganic solar cells under fluorescent lights [15].

5.3.2 Performance of C-DSSCs under fluorescent lamp using N719 dye

After satisfactory performance of the C-DSSC using N719 dye with white light, its performance was also analyzed under illumination using low intensity fluorescent lamp. With the use of the reflectors both of the efficiency and total output power was increased as shown in the Figure 7. This figure shows the best performance using reflector with equation 1/10 X^2 compared to other reflectors fabricated using different equations. Although all of the reflectors used for this had same projection area, however, difference in performance could be seen. This might be attributed

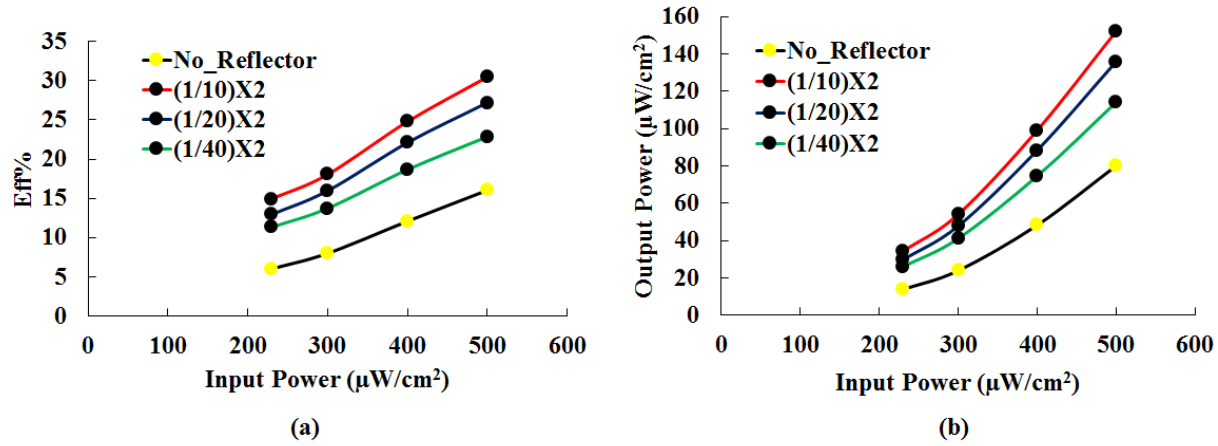

Figure 7. Performance of C-DSSC (N719 dye) utilizing reflectors of different equation

to differences in the input power distribution on the surface of the TiO_2. To confirm this we did some simulation study using Trace Pro 7.5.1 by preparing optical model of our C-DSSC. The refractive index of the constituent layers which are above TiO_2/Dye surface such as heat shrinkable tube & electrolyte was used to prepare the model & finally the input power distribution on the TiO_2/Dye surface was analyzed and total power was calculated. For this purpose first a parallel light source was used with input power intensity of 0.3 mW/cm^2. In this simulation study there is no loss of light energy hence the distance between the light source and reflector surface doesn't affect the simulation results in case of parallel light source.

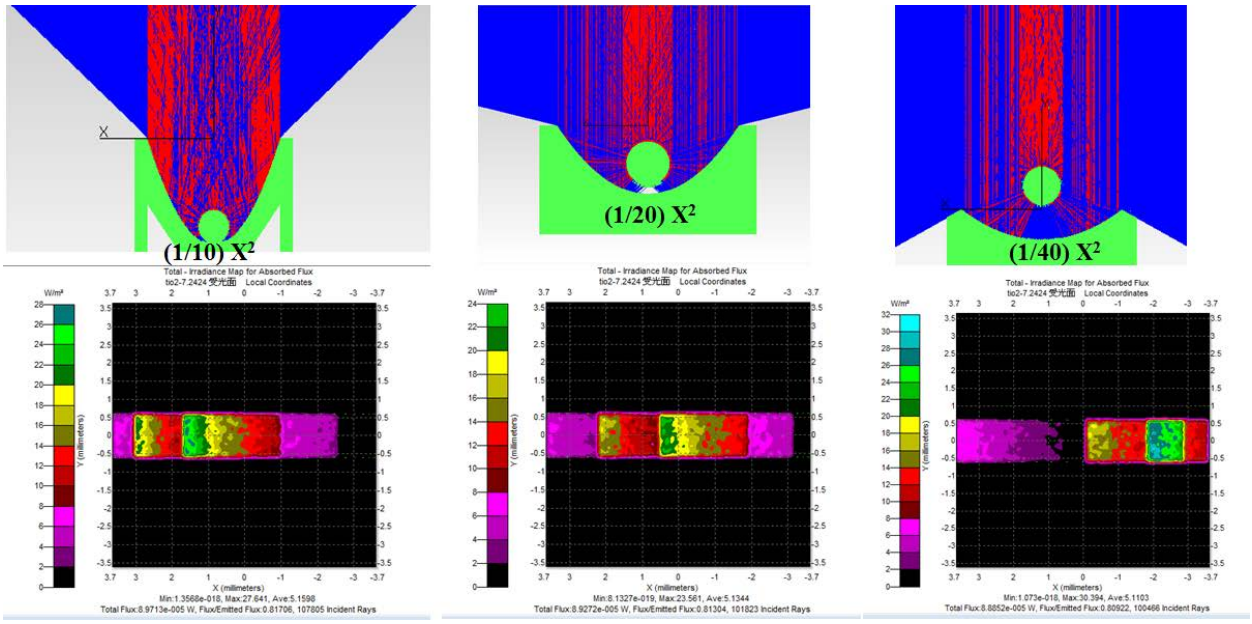

Figure 8. Input power distribution on the surface of TiO_2/Dye using parallel light source with 0.3 mW/cm^2 intensity

Table 1. Calculated input power on TiO_2/Dye (Reflectors are with projection area of 2*3cm^2)

	$(1/10)X^2$	$(1/20)X^2$	$(1/40)X^2$
Average Input Power (mW/cm^2)	0.328	0.325	0.326
Total input power(mW)	0.112	0.111	0.111

The results obtained for this are shown in Figure 8. The different intensities are shown with different colors according to the chart on the left of each plot. It shows approximately the same total input power as listed in Table 1 on the TiO_2/Dye surface with the use of all the reflectors. In principle it should not be the possible since we are getting different efficiency & output power, therefore, input power should be different. To completely understand we thought about the real time experimental situation, where light is not parallel but falling on the object surface from all direction. Hence, we simulated the same C-DSSC model with the use of spherical source with intensity of 100 mW/cm^2, keeping it at fixed distance from bottom of the

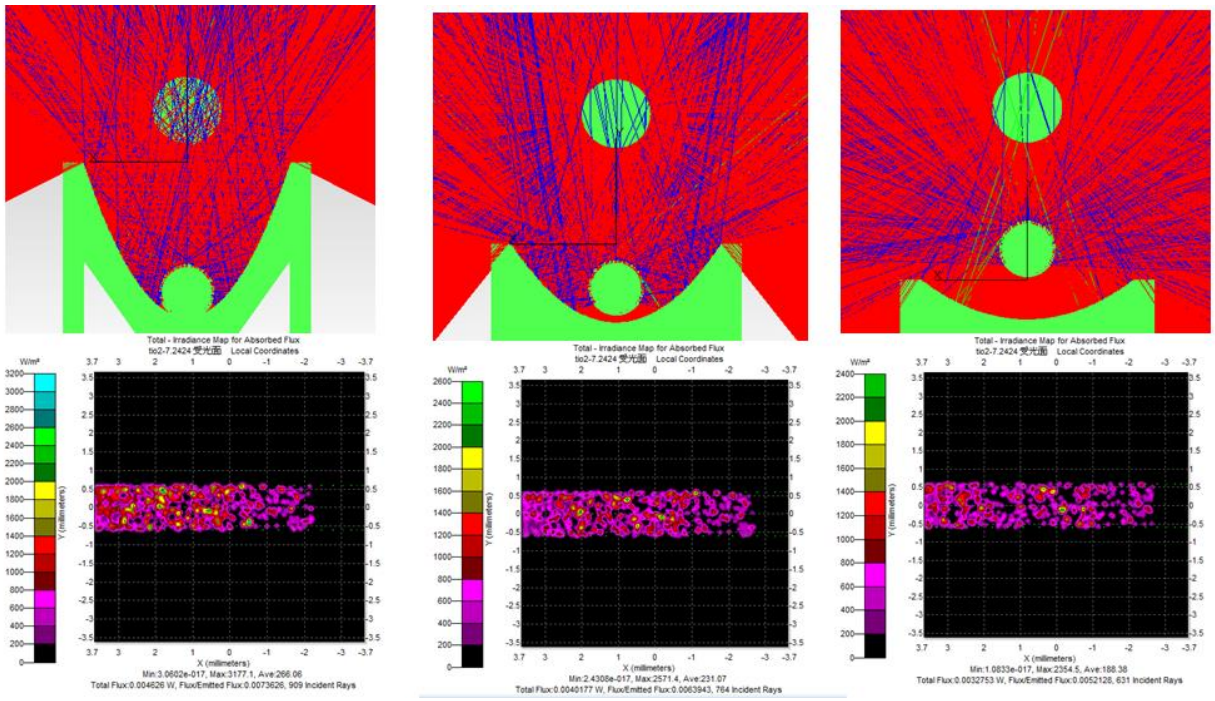

Figure 9. Input power distribution on the surface of TiO_2/Dye using spherical light source with 100 mW/cm^2 intensity

reflector in all the cases. Here, we found that total input power on the surface of TiO_2/Dye using 1/10 X^2 equation based reflector was maximum while it was minimum in case of reflector made using 1/40 X^2 as listed in Table 2. This possibly explains the reason for getting different results using different reflectors.

Table 2. Calculated input power on TiO_2/Dye (Reflectors are with projection area of 2*3cm^2)

	$(1/10)X^2$	$(1/20)X^2$	$(1/40)X^2$
Average Input Power (mW/cm^2)	16.59	14.71	11.97
Total input power(mW)	5.97	5.29	4.30

5.3.2.1 Effect of change in area of the reflector

This is an interesting result obtained in case of the C-DSSCs using reflectors with different projection area. We found that when we increased the length of the reflectors the output power

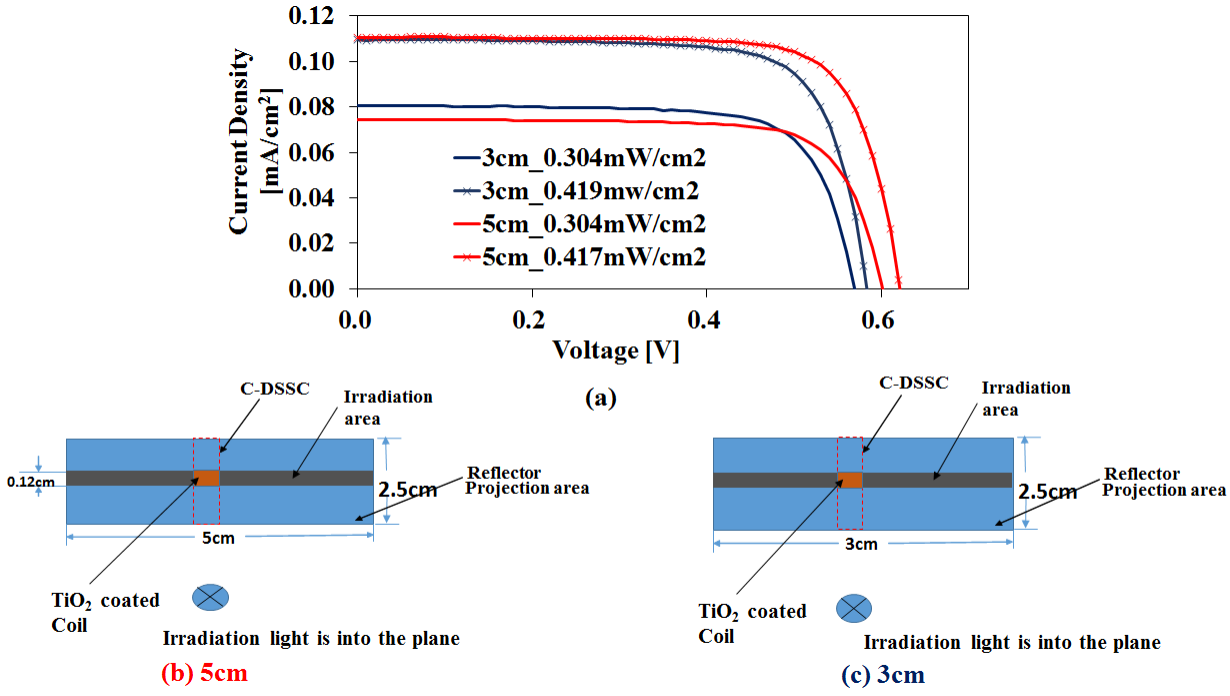

Figure 10. (a) Current-Voltage Characteristics using reflectors with different projection area (blue line is for 3 cm long & red line is for 5 cm long reflector)

was increasing as shown in the Table 3. We have taken 3 cm and 5 cm long reflectors with the same width as shown in Figure 10. In cases of both the reflectors the PCE obtained for the same intensity was approximately the same.

Table 3 Photovoltaic parameters of C-DSSC using reflectors with different projection area

	3cm_0.304mW/cm2	3cm_0.419mW/cm2	5cm_0.304mW/cm2	5cm_0.417mW/cm2
Efficiency [%]	11.21	11.47	11.13	12.57
FF	0.74	0.75	0.75	0.76
Voc[V]	0.57	0.58	0.60	0.62
Jsc[mA/cm^2]	0.08	0.11	0.07	0.11
Area[cm^2]	0.36	0.36	0.60	0.60
Output Power (mW)	0.012	0.017	0.020	0.031

However, the output power in case of larger reflector *i.e.* for 5 cm long reflector was higher than 3 cm long reflector which is due to increase of input power on the surface of the TiO_2/Dye with the larger reflector. Table 3 shows output power of the same C-DSSC was increased from 0.012 mW to 0.020 mW when intensity of 0.304 mW/cm^2 was used with increase in reflector area. Similarly, with the use of approximately 0.417 mW/cm^2 intensity the output power for the same C-DSSC was increased from 0.017 mW to 0.031 mW. However, PCE obtained in all cases was nearly the same for the same intensity used.

5.3.3 C-DSSC performance using different dyes (N719, D205 & Y123)

Figure 11 shows the photocurrent density-voltage (J-V) curves for the C-DSSCs using different sensitizing dyes measured at AM 1.5G condition along with their photovoltaic parameters shown in the Table 4. The C-DSSC sensitized using N719 dye exhibits best efficiency of 4.02 % outperforming the results obtained for D205 and Y-123 as 3.36 % and 2.30 %, respectively.

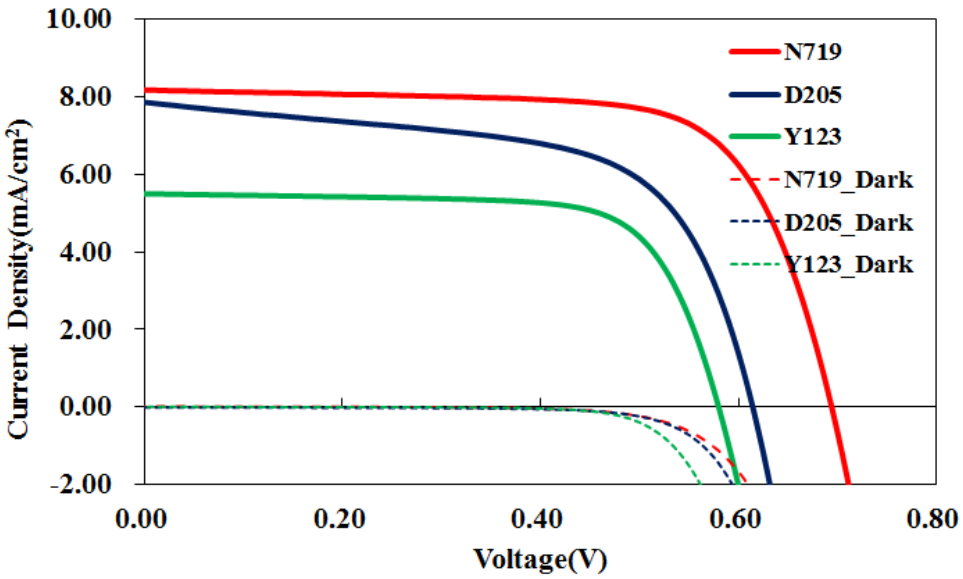

Figure 11. IV and dark current characteristics of the devices using different dye.

Table 4. Photovoltaic parameters for the C-DSSCs at 100mW/cm^2

	N719	**D205**	**Y-123**
Efficiency[%]	4.02 (3.66±0.32)	3.36 (3.06±0.26)	2.30 (2.3±0.02)
FF	0.71 (0.66±0.04)	0.70 (0.64±0.05)	0.72 (0.72±0.005)
Voc[V]	0.69 (0.66±0.03)	0.62 (0.62±0.01)	0.58 (0.57±0.01)
Jsc[mA/cm^2]	8.18 (8.2±0.32)	7.77 (7.68±0.24)	5.50 (5.55±0.07)

*Value shown in parenthesis exhibits the average data for each parameter along with standard deviation for three independent cells fabricated under identical conditions.

The open circuit voltage (Voc) in the case of N719 dye based C-DSSC is 0.69 V, which is quite higher than 0.62 V and 0.58 V of D205 and Y-123, respectively. This is mainly due to higher

recombination in the case of D205 and Y-123 based solar cells as can be seen in dark current characteristics shown in the Figure 11. This is in agreement with the previous reports showing higher recombination in organic dyes compared to Ru complex based N719 dye [13]. The fill-factor (FF) which is mainly affected by the adhesion between coated nanoporous TiO_2 and Ti substrate [16], is almost same for all of C-DSSCs based on different dyes used in the present investigation.

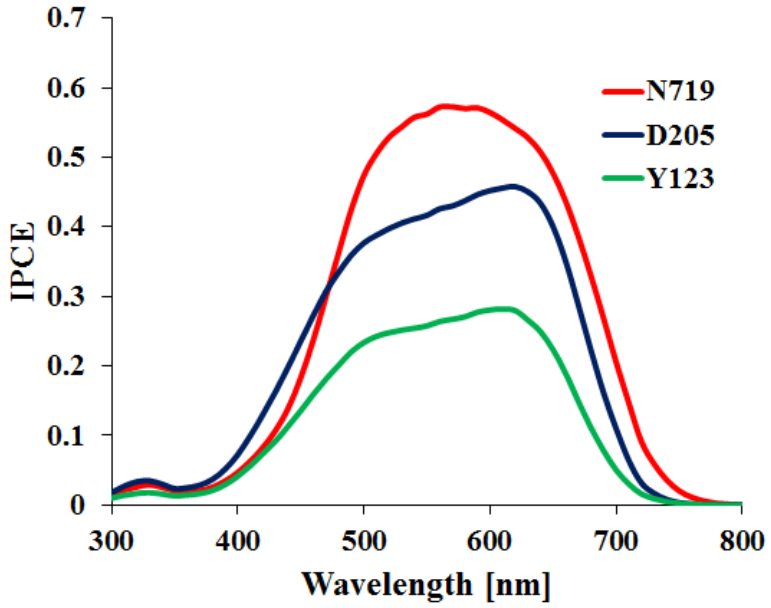

Figure 12. IPCE curve obtained for the devices.

Figure 12 exhibits the incident photon to current conversion efficiency (IPCE) for the different devices. The higher value of IPCE about 60% for N719 based device compared to around 50% and 30% for D205 and Y-123 based C-DSSCs, respectively, is in accordance with the observed Jsc values shown in the Figure 11. In all of the dyes the light absorption window is almost the same as can be seen in Figure 13, which shows solid-state UV-Visible electronic absorption spectra of the dyes adsorbed on the nanoporous TiO_2 thin film. This indicates that nearly similar light harvesting capability for dyes N719 and D205 except Y123, however, different recombination leads to different IPCE and Jsc.

To have further insight about the reason behind the different recombination, EIS measurement was also performed at the constant current of 1 mA/cm^2 under 1 Sun illumination

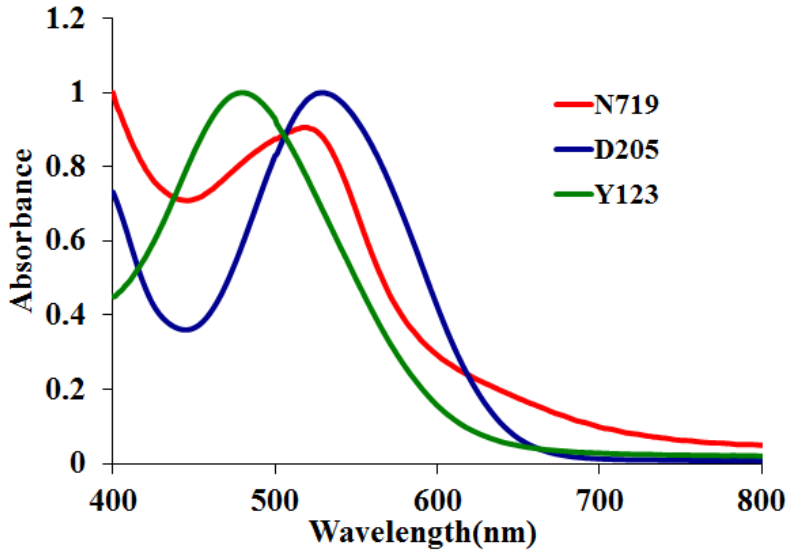

Figure 13. UV-Vis spectra on the TiO_2 thin film for the dyes used.

as shown in Figure 14 (a). The electrical equivalent circuit along with the different resistances is shown in Figure 14 (b) which was determined as per the previous reports [17]. R1 is the resistance to the electron flow in the Ti wire, which should be almost the same for all of the devices since Ti wire with same length and diameter was used to fabricate the different C-DSSCs. R2 is resistance related to charge transfer through counter electrode and responsible for the different fill factor (FF), which seems to be not a deciding parameter for different solar cell performance. R3 is the charge transfer resistance at TiO_2/Dye/electrolyte interface, which is 72.11 Ω for N719 based device compared to D205 (139.6 Ω) and Y123 (147.10 Ω). This resistance is mainly responsible for higher recombination in both of the organic dye based device in comparison to N719 based device.

To effectively utilize the C-DSSCs due to its cylindrical geometry, its top and bottom both of the surfaces are needed to be illuminated at the same time. As shown in the Figure 11, the solar cell performance under white light performance was only due to the top surface of the C-DSSC, which has contributed to the electrical power generation and the bottom surface which was under diffused or no light might have increased the resistance of the solar cell. Therefore, the parabolic reflectors were taken to tap the diffused light for fluorescent lamp lights as shown in Figure 15(a) & (b). It is well known that the parabolic geometry leads to the maximum power

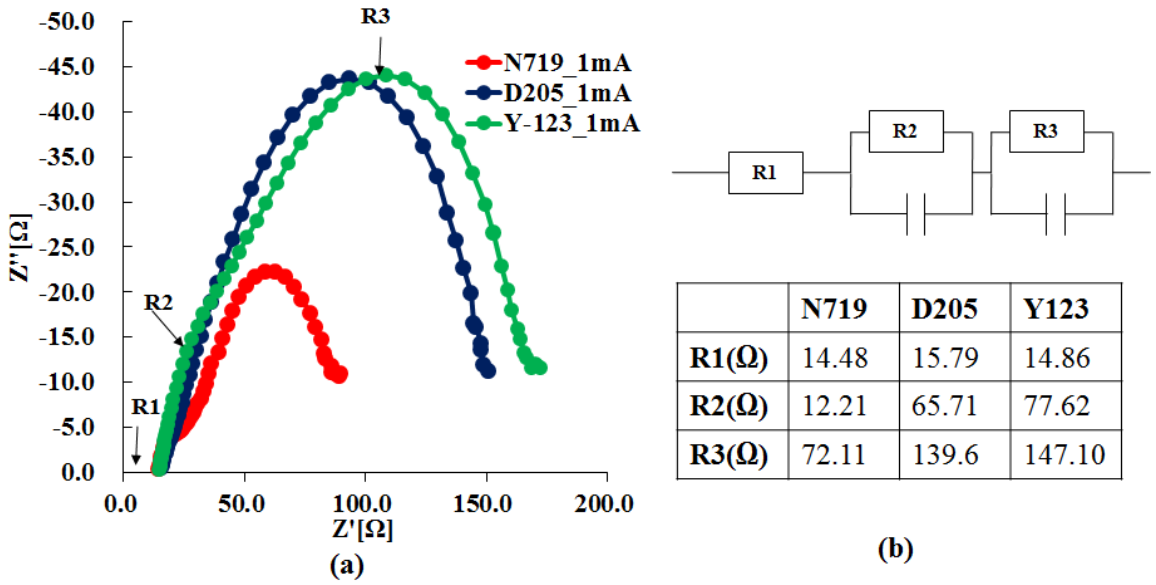

	N719	D205	Y123
R1(Ω)	14.48	15.79	14.86
R2(Ω)	12.21	65.71	77.62
R3(Ω)	72.11	139.6	147.10

Figure 14. EIS measured at constant current of 1mA/cm^2 under 1 SUN.

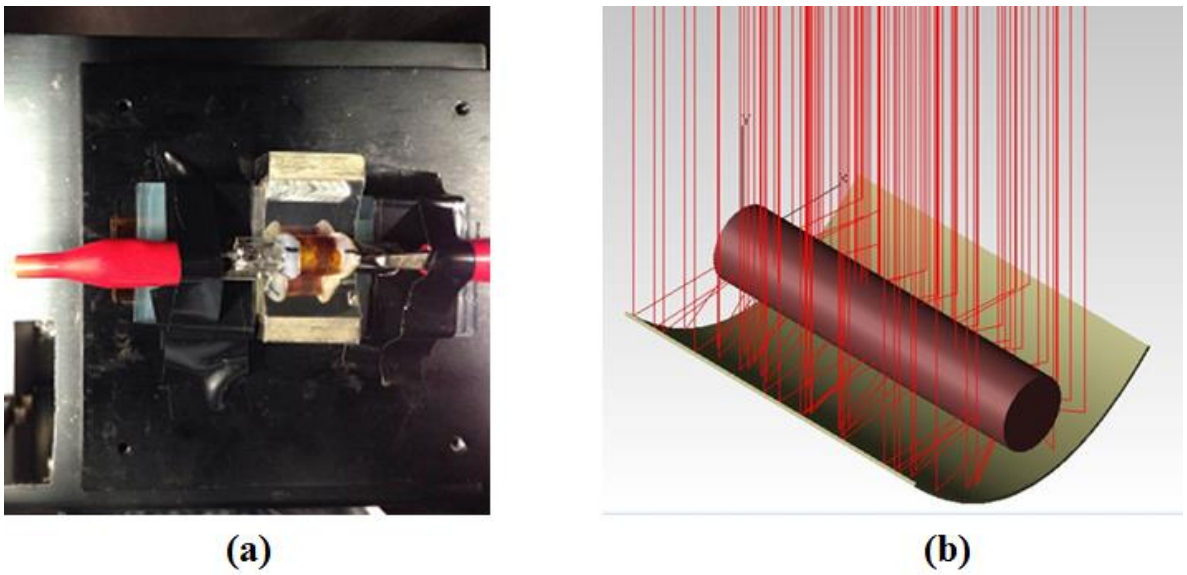

Figure 15. Experimental set up for the measurement done.

input at the focus point and the reflector used in this work reflects above 90% of light falling vertically from the top. Therefore, it allows to utilize the reflected light effectively for the bottom surface of the C-DSSCs. All the measurements were done with the utilization of reflector have

irradiation area as the width of TiO_2 coated surface multiplied with length of the reflector, which is the projection area of C-DSSC on the reflector surface.

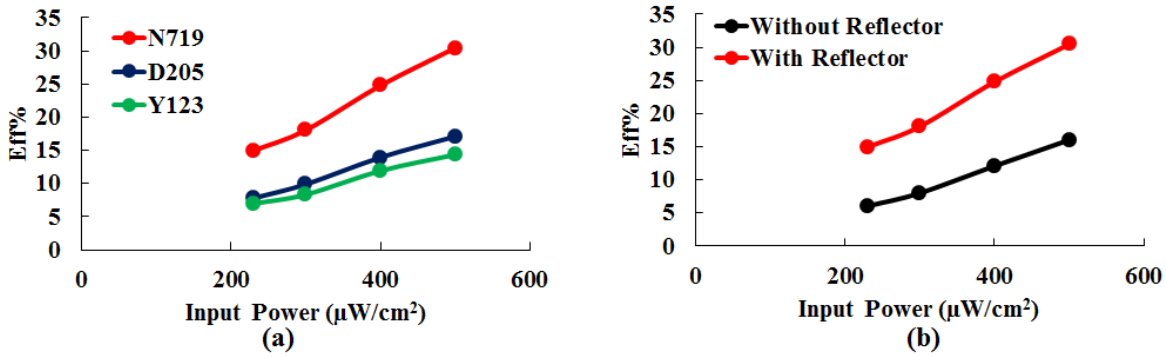

Figure 16. **(a)** Performance of the devices with reflector. **(b)** Performance of device using N719 dye

Figure 16a exhibits the performance of all of the devices at different light intensities in the presence of a parabolic reflector. It shows the similar trend as observed under the white light illumination but with much enhanced photoconversion efficiencies. The C-DSSC based on N719 dye shows efficiency around 15 % at 230 $\mu W/cm^2$ (1533 Lux) and it increases up to 30 % at 500 $\mu W/cm^2$ (3333 Lux). With the use of reflector the solar cell performance has increased almost two times compared to that of without reflector as shown in Figure 16(b). D205 and Y123 based DSSC shows nearly same performance at 230 $\mu W/cm^2$ and with the increase in the intensity there is little improved performance by the D205 based C-DSSC. This poor performance due to organic based dyes is probably due to the higher recombination, which are becoming more prominent under low intensity fluorescent lights. The resistance R3 in Figure 14 increases with the decrease in the intensity [18, 19] which enhances the recombination more for the organic dyes in comparison to N719 based device. The IV-curve for the best solar cell using N719 dye with and without reflector geometry at 1533 Lux intensity is shown in Figure 17 along with the average photovoltaic parameters shown in the Table 5. It can be seen from this figure and Table 5 that all of the photovoltaic parameters such as Jsc, Voc, FF, efficiency and out-put power were found to be enhanced when parabolic reflector was used during the photovoltaic characteristic measurement. Results thus obtained in this present work was also compared with the commercially available amorphous silicon based solar cells [20] for low intensity in-door applications. The output power of 34.40 $\mu W/cm^2$ obtained with reflector at 1533 Lux in the

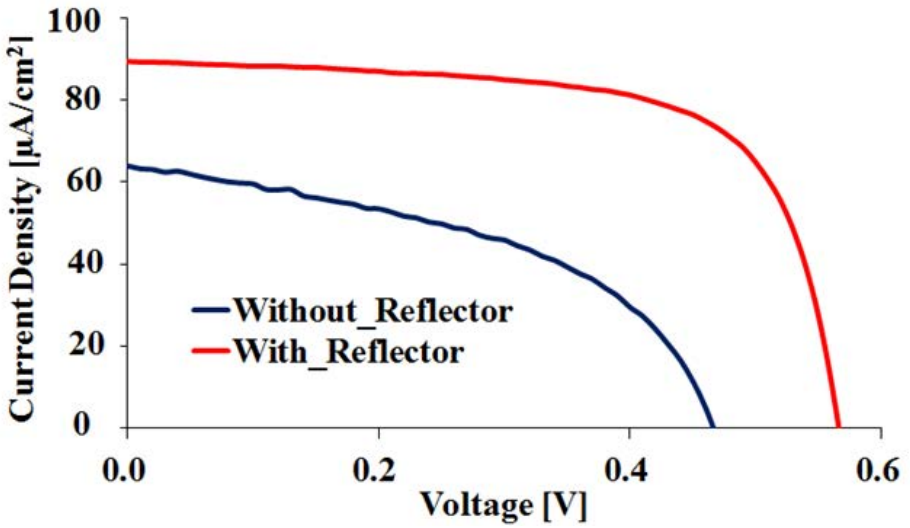

Figure 17. Performance of the device at around 1500 LUX using N719 dye.

Table 5 Photovoltaic parameters for the device using N719 dye at 1533 LUX.

	Without Reflector	**With Reflector**
Efficiency[%]	6.05 (5.61±1.6)	14.95 (12.79±1.6)
FF	0.47 (0.48±0.07)	0.68 (0.65±0.04)
Voc[V]	0.47 (0.45±0.05)	0.57 (0.55±0.03)
Jsc[μA/cm²]	63.86 (59.94±6.5)	89.35 (80.46±6.2)
Output Power(μW/cm²)	13.90 (12.98±3.66)	34.40 (28.96±3.8)

*Value shown in parenthesis exhibits the average data for each parameter along with standard deviation for three independent cells fabricated under identical condition.

present work seems to exhibit the satisfactory performance when it was compared to amorphous silicon based solar cell under the fluorescent light at 200 Lux giving out-put power of 7 μW/cm^2 varying linearly up to >1000 Lux.

5.4 CONCLUSIONS

Ti coil based TCO-less cylindrical DSSC have been fabricated and used for indoor light applications. Performance under both of the white and fluorescent light was measured with and without reflector. Different parabolic reflectors having equations of 1/10 X^2, 1/20 X^2 and 1/40 X^2 were fabricated using 3D printer and utilized effectively to enhance both efficiency and the total output power. C-DSSC was optically modelled using Trace Pro 7.5.1 optical simulation software in order to investigate the distribution of input power on the cylindrical photoanodes of the C-DSSCs. Based on this optical simulation, it was found that main reason for high output power with reflectors is due to increase in the input power on TiO_2/Dye surface. C-DSSC using Ru metal based N719 dyes showed better performance compared to organic dyes such as D205 and Y123 both in 1 SUN as well as fluorescent light illuminations. The C-DSSC based on N719 dye giving the efficiency of 4.02 % under 1 SUN was dramatically improved to about 30 % under fluorescent light illumination with the intensity of 0.5 mW/cm^2. The TiO_2/Dye/electrolyte interface resistance was responsible for the variable device performance. The output power obtained at around 1500 LUX showed satisfactory performance of C-DSSC implemented with the reflector in comparison to commercially available amorphous Si based solar cells.

References

1.Grätzel, M. (2004). Conversion of sunlight to electric power by nanocrystalline dye-sensitized solar cells. *Journal of Photochemistry and Photobiology A: Chemistry*, *164*(1), 3-14.

2.Smestad, G., Bignozzi, C., & Argazzi, R. (1994). Testing of dye sensitized TiO_2 solar cells I: experimental photocurrent output and conversion efficiencies. *Solar energy materials and solar cells*, *32*(3), 259-272.

3.Kashiwa, Y., Yoshida, Y., & Hayase, S. (2008). All-metal-electrode-type dye sensitized solar cells (transparent conductive oxide-less dye sensitized solar cell) consisting of thick and porous Ti electrode with straight pores. *Applied Physics Letters*, *92*(3), 033308-033308.

4.Molla, M., Mizukoshi, N., Furukawa, H., Ogomi, Y., Pandey, S. S., Ma, T., & Hayase, S. (2014). Transparent conductive oxide‐less back contact dye‐sensitized solar cells using cobalt electrolyte. *Progress in Photovoltaics: Research and Applications*.

5.Nazeeruddin, M. K., Pechy, P., Renouard, T., Zakeeruddin, S. M., Humphry-Baker, R., Comte, P., & Grätzel, M. (2001). Engineering of efficient panchromatic sensitizers for nanocrystalline TiO2-based solar cells. *Journal of the American Chemical Society*, *123*(8), 1613-1624.

6.Greijer, H., Karlson, L., Lindquist, S. E., & Hagfeldt, A. (2001). Environmental aspects of electricity generation from a nanocrystalline dye sensitized solar cell system. *Renewable Energy*, *23*(1), 27-39.

7. Kapil, G., Ohara, J., Ogomi, Y., Pandey, S. S., Ma, T., & Hayase, S. (2014). Fabrication and characterization of coil type transparent conductive oxide-less cylindrical dye-sensitized solar cells. *RSC Advances*, *4*(44), 22959-22963.

8.Usagawa, J., Pandey, S. S., Ogomi, Y., Noguchi, S., Yamaguchi, Y., & Hayase, S. (2013). Transparent conductive oxide‐less three‐dimensional cylindrical dye‐sensitized solar cell fabricated with flexible metal mesh electrode. *Progress in Photovoltaics: Research and Applications*, *21*(4), 517-524.

9.Hinsch, A., Brandt, H., Veurman, W., Hemming, S., Nittel, M., Würfel, U., ... & Fichter, K. (2009). Dye solar modules for facade applications: recent results from project ColorSol. *Solar Energy Materials and Solar Cells*, *93*(6), 820-824.

10. Mishra, A., Fischer, M. K., & Bäuerle, P. (2009). Metal‐free organic dyes for dye‐sensitized solar cells: From structure: Property relationships to design rules. *Angewandte Chemie International Edition*, *48*(14), 2474-2499.

11. Ito, S., Zakeeruddin, S. M., Humphry‐Baker, R., Liska, P., Charvet, R., Comte, P., ... & Grätzel, M. (2006). High‐Efficiency Organic‐Dye‐Sensitized Solar Cells Controlled by Nanocrystalline‐TiO_2 Electrode Thickness. *Advanced Materials*,*18*(9), 1202-1205.

12. Yum, J. H., Baranoff, E., Kessler, F., Moehl, T., Ahmad, S., Bessho, T., ... & Grätzel, M. (2012). A cobalt complex redox shuttle for dye-sensitized solar cells with high open-circuit potentials. *Nature communications*, *3*, 631.

13. Wang, H., Liu, M., Zhang, M., Wang, P., Miura, H., Cheng, Y., & Bell, J. (2011). Kinetics of electron recombination of dye-sensitized solar cells based on TiO_2 nanorod arrays sensitized with different dyes. *Physical Chemistry Chemical Physics*, *13*(38), 17359-17366.

14. Fu, Y., Lv, Z., Hou, S., Wu, H., Wang, D., Zhang, C., ... & Zou, D. (2011). Conjunction of fiber solar cells with groovy micro-reflectors as highly efficient energy harvesters. *Energy & Environmental Science*, *4*(9), 3379-3383.

15. Sridhar, N., & Freeman, D. (2011). A study of dye sensitized solar cells under indoor and low level outdoor lighting: comparison to organic and inorganic thin film solar cells and methods to address maximum power point tracking. In *26th European photovoltaic solar energy conference and exhibition*.

16. An, J., Guo, W., & Ma, T. (2012). Enhanced Photoconversion Efficiency of All‐Flexible Dye‐Sensitized Solar Cells Based on a Ti Substrate with TiO_2 Nanoforest Underlayer. *Small*, *8*(22), 3427-3431.

17. Lan, J. L., Wei, T. C., Feng, S. P., Wan, C. C., & Cao, G. (2012). Effects of iodine content in the electrolyte on the charge transfer and power conversion efficiency of dye-sensitized solar cells under low light intensities. *The Journal of Physical Chemistry C*, *116*(49), 25727-25733.

18. Longo, C., & De Paoli, M. A. (2003). Dye-sensitized solar cells: a successful combination of materials. *Journal of the Brazilian Chemical Society*, *14*(6), 898-901.

19. Lv, Z., Wu, H., Cai, X., Fu, Y., Wang, D., Chu, Z., & Zou, D. (2012). Influence of electrolyte refreshing on the photoelectrochemical performance of fiber-shaped dye-sensitized solar cells. *International Journal of Photoenergy*, *2012*.

20. http://www.panasonic.net/energy/amorton/jp/pdf/P120B.pdf

CHAPTER 6: GENERAL CONCLUSIONS

Possibility of fabrication of dye-sensitized solar cells (DSSCs) on the flexible substrates was explored and a new cylindrical solar cell architecture using the metallic wires named as C-DSSC was proposed. The main idea was to develop a cost effective and industrially viable cylindrical solar cells for large area applications. Efforts were directed to remove the existing problems in previous device architectures such as shading effect and complex fabrication process along with improvement of its performance in this novel device architecture. In addition, use of these solar cells for indoor light application using parabolic reflectors with some optical simulation was also demonstrated.

In the first chapter of the thesis, I did some literature survey on the flexible solar cells which gave me an idea and possible area of research in DSSC. The TCO-less cylindrical architecture owing to its advantages such as uniform solar harvesting, higher total output in day as compared to conventional flat solar cell along with its cost effectiveness have shown its potential for commercialization and also less research in this area motivated to develop a new architecture.

In the second chapter, I gave a brief introduction on characterization techniques used in analyzing a typical DSSC. A short literature survey along with principle underlying the working principle of different characterizations tools used in the present work was done

Chapter three deals with my beginning of experimental work regarding proposal of novel device architecture along with confirmation of it's functioning. In this context, fabrication of a novel TCO-less cylindrical dye-sensitized solar cell with more ease and fast method of fabrication was demonstrated and compared to other previous TCO-less DSSC architectures. It has been shown that nature of wire and surface treatment plays an important role in controlling the device performance. EIS investigation revealed that better electrical contact between metal wires and nanoporous TiO_2 was controlling the overall photovoltaic performance. Various aspects related to performance of our device such as passivating nature of Ti and its effect on the performance of our solar cell was conducted in detail leading to observation 3.88% photoconversion efficiency using SS/Ti (stainless-steel sputtered with titanium).

Chapter four was mainly focused on performance of our solar cell using Ti wire only to find some answers of the queries which came in the previous chapter related to use of Ti as substrate. Ti wire was obvious choice also due to its low resistance, good flexibility, superior corrosion resistance and high temperature stability which was suitable for C-DSSC fabrication. Here it was found that mechanically polished Ti wire exhibited a considerable enhancement in solar cell efficiency from 1.03 % to 3.06 %. H_2O_2 surface treatment further improved the photoconversion efficiency from 4.04 % to 4.71%, which is due to the formation of anatase (A-101) nanosheet like structures enhancing surface area and good contact assisting the enhanced dye loading and facile charge transport, respectively.

Finally, chapter five showed an important application of DSSC for generating electricity under indoor light conditions. The cylindrical geometry allows the use of reflectors to tap the diffused and reflected light, hence keeping this in mind I showed that C-DSSC can be used more effectively using the parabolic reflectors. C-DSSC was optically modelled using Trace Pro 7.5.1 and it was found that main reason for high output power with reflectors is due to increase in the input power on TiO_2/Dye surface. Different dyes such as N719, D205 & Y123 were taken to evaluate the effect on the performance of C-DSSCs under low intensity fluorescent light illuminations. Fluorescent light with intensities (0.1 mW/cm^2 to 0.5mW/cm^2) were used for comparative study of solar cell performances. In the end, the output power obtained for C-DSSCs at 1500 LUX illumination exhibited comparable performance with that commercially available amorphous Si based solar cell.

FUTURE PROSPECTS

The idea and knowledge gained about the surface properties of metallic wire and use of these metallic wires for developing cylindrical TCO-less DSSCs could be used with some high performing dyes such as black dye and zinc porphyrin dye (in case of conventional flat DSSC the PCE using these is 11 % & 13% respectively) and dye cocktails along with suitable electrolyte combination could possibly enhance the C-DSSC performance even further. Another important aspect is to implement the Ti substrate in future to some other fields of solar cell especially in case of solution processed organic-inorganic hybrid solar cells (OIHSCs). In OIHSCs, a TCO-less architecture with these metallic substrates could be a breakthrough. Recent past has witnessed that solution processed organic-inorganic hybrid solar cells (OIHSC) have now reached photoconversion efficiency (PCE) of about 20 % which is almost equal to the CIGS and expected to reach up to crystalline silicon (25%) solar cells. Now demand of time is a real big challenge to bring this lab research to common society considering the cost, stability and environmental concerns.

Overall cost depends directly on fabrication cost and inversely on the efficiency and its stability. Therefore, by adopting TCO-less device architecture in combination with high PCE of OIHSC would rather make it easier to enhance efficiency of TCO-less cylindrical solar cells. Although there are few reports on fabricating the OIHSCs on PET/ITO and stainless steel wires, however, reported PCEs are very low, therefore, still have sufficient rooms for the further improvement. Also, the long term stability owing to the high moisture sensitivity of OIHSC due to improper sealing could be solved with the use of heat shrinkable tube and cylindrical geometry.

BIBLIOGRAPHY

Journal Papers (*Corresponding author)

1. **Gaurav Kapil***, Jin Ohara, Yuhei Ogomi, Shyam S. Pandey, Tingli Ma and Shuzi Hayase*: ***"Fabrication and characterization of coil type transparent conductive oxide-less cylindrical dye sensitized solar cells",*** RSC Adv., 2014, 4, 22959. (**IF**:3.708)

2. **Gaurav Kapil***, Shyam S. Pandey, Yuhei Ogomi, Tingli Ma and Shuzi Hayase*:"***Titanium wire engineering and its effect on the performance of coil type cylindrical dye sensitized solar cells",*** Organic electronics, 2014, 15, 3399–3405. (**IF**:3.676)

3. Tarun Chand Vagvala*, **Gaurav Kapil**, Shyam S. Pandey, Yuhei Ogomi, Shuzi Hayase*: ***"Non-isothermal curing kinetics of epoxy resin composite utilizing Ga (III) xanthate as a latent catalyst",*** Journ. App. Polym. Sci., 2015, DOI: 10.1002/app.42149. (**IF**: 1.6).

4. K. Narayanaswamy, T. Swetha, **Gaurav Kapil**, Shyam S. Pandey*, Shuzi Hayase and Surya Prakash Singh*: "***Simple Metal-Free Dyes Derived from Triphenylamine for DSSC: A Comparative Study of Two Different Anchoring Group",*** Electrochimica Acta, 2015, 169, 256-263.(**IF**: 4.433)

5. **Gaurav Kapil***, Yuhei Ogomi, Shyam S. Pandey, Tingli Ma, Shuzi Hayase* ***:"Implication of different dyes on the performance of coil type cylindrical dye sensitized solar cells for indoor applications",*** Jour. Of Nano. Sci. & Nano. 2015***(accepted)*** (**IF**: 1.339)

6. Anubha Bilgaiyan, Tejendra Dixit, **Gaurav Kapil**, Shyam S Pandey, Shuji Hayase, Iyamperumal Anand Palani and Vipul Singh***: "Effect of Addition of KI on the Hydrothermal Growth of ZnO Nanostructures Towards Hybrid Optoelectronic Device Applications",*** Jour. Of Nano. Sci. & Nano. 2015***(accepted)***(**IF**: 1.339)

7. **Gaurav Kapil** , Jin Hui Wang, Yuhei Ogomi, Shyam S. Pandey, Tingli Ma and Shuzi Hayase : ***"Combining simulation and experimental analysis for indoor light application of Titanium-coil based cylindrical dye sensitized solar cells"*** (in Preparation)

CONFERENCE PRESENTATIONS

1. **Gaurav Kapil** , Jin Hui Wang, Yuhei Ogomi, Shyam S. Pandey, Tingli Ma and Shuzi Hayase : ***"Investigation of effective utilization of titanium (Ti) coil based cylindrical dye sensitized solar cells for indoor light application"*;** presented at the 95th Annual Meeting of the Chemical Society of Japan, Nihon University, Chiba, Japan, March 26-29, 2015. (ORAL)
2. **Gaurav Kapil**, Yuhei Ogomi, Shyam S. Pandey, Tingli Ma, Shuzi Hayase: ***" Implication of different dyes on the performance of coil type cylindrical dye sensitized solar cells for indoor applications";*** presented at The 11th International Conference on Nano-Molecular Electronics (ICNME 2014), Kobe, December 17-19, 2014. (ORAL)
3. **Gaurav Kapil**, Shyam S. Pandey, Yuhei Ogomi, Tingli Ma, Shuzi Hayase: *"**Effect of surface treatment and cross-sectional area of Ti wire on the performance of coil based TCO-less cylindrical DSSCs"*;** presented at The 15th IUMRS-International Conference in Asia (IUMRS-ICA 2014), Fukuoka University, Fukuoka, Japan, August 24-30, 2014. (ORAL)
4. **Gaurav Kapil**, Shyam S. Pandey, Yuhei Ogomi, Tingli Ma, Shuzi Hayase:*"**Utilization of metallic coils for TCO-less cylindrical DSSC: investigation of photovoltaic performance under lower light intensities"***; presented at SPIE optics + photonics 2014, San Diego Convention Center, San Diego, California, USA, August 19-21, 2014.(POSTER)
5. **Gaurav Kapil**, Shyam S. Pandey, Yuhei Ogomi, Tingli Ma, Shuzi Hayase***"Effect of Titanium coil photoanodes on the performance of cylindrical dye-sensitized solar cells";*** presented at Kyushu Branch Chemical Society Meeting (KBCS)-2014, Japan. (POSTER)
6. **Gaurav Kapil**, Shyam S. Pandey, YuheiOgomi, Tingli Ma and Shuzi Hayase: ***"Approaches implemented to enhance the photovoltaic characteristics of Coil based TCO-less cylindrical dye sensitized solar cell";*** presented at the 94th Annual Meeting of the Chemical Society of Japan, Nagoya University, Aichi, Japan, March 27-30, 2014. (ORAL)

7. **Gaurav Kapil,** Jin Ohara, Yuhei Ogomi, Shyam S. Pandey and Shuzi Hayase: ***"Optimization and fabrication of Coil based TCO-less cylindrical dye-sensitized solar cells";*** presented at MRS-JSAP-Autumn-2013 Joint Symposia Program, Doshisha University, Kyotanabe Campus, Japan, September 16-20, 2013.(ORAL)

8. **Gaurav Kapil,** Jin Ohara, Yuhei Ogomi, Shyam S. Pandey and Shuzi Hayase: ***"Investigation pertaining to fabrication of Coil based Cylindrical DSSC";*** presented at Kyushu Branch Chemical Society Meeting (KBCS)-2013, Japan.(POSTER)

ACKNOWLEDGEMENT

First and foremost, I would like to express my deepest appreciation to my supervisor **Prof. Shyam S. Pandey**, especially his cool and calm nature have really made even my hectic schedule for research work a fun and time to enjoy for me. I do remember that whenever I needed he gave me time for discussion about my research work and really motivated me throughout my research work. He genuinely supported me throughout my research work. Truly without his guidance and persistent help this thesis would not have been possible.

I wish to express my sincere thanks to **Prof. Shuzi Hayase**, for showing faith in me for doing this project. I am really thankful to him for providing me necessary facilities for the research. He continually and convincingly conveyed a spirit of adventure in regard to research and an excitement in regard to explore new areas of research apart from my own research work.

I would like to take this opportunity to thank **Prof. Tingli Ma**, her vast research experience have helped me a lot to give the present shape to my thesis work. Her time to time guidance and valuable suggestions during research meetings were really fruitful for me to enhance the knowledge regarding my research work.

I would take this opportunity to pay my warm regards to my respected Professor in India **Prof. Rajiv Prakash**, who recommended me to work in Hayase, Pandey & Ma lab.

I place on record, my sincere thanks to **Prof. Yuhei Ogomi**, **Prof. Wataru Takashima & Dr. Teresa S. Ripolles** for giving me advices during my research work.

I would like to express my special thanks to **Dr. Terumi Nishimura** & **Mr. Kazuhiko Sakamoto** for making the positive working environment of the lab with their happy and jolly faces every day.

I can't find words from dictionary to say thanks to my colleagues **Mr. Azwar Hayat**, **Mr. Tarun Chandra Vagwala** & **Mr. Zaman Molla** for their beautiful company. I am really happy that we all are together in the stage to complete our doctorate work.

In Japan, I would give my special thanks to all my Indian friends especially **Mr. Gyanendra Nath Tripathi** & **Mr. Ajay Kumar Baranwal** for their nice company of almost two and half year.

I express warm thanks to my Table Tennis partners **Dr. Cao Zhenbo**, **Mr. Ravi Nath Tripathi**, **Mr. Nishanth Koganti** and all other friends for giving me their enjoyable company.

In India, I would like to thank my friend **Mr. Narendra Mahra** for his support and attention. I also thank my parents (**Mr. Kewala Nand Kapil & Mrs. Pushpa Kapil**) & my sister (**Miss. Namarata Kapil**) who are always a constant source of inspiration for me & all my family members for their constant support and encouragement.

Finally I also place on record, my sense of gratitude to all the members of **Hayase, Pandey & Ma lab, all the staff members and students of KIT**, who directly or indirectly have helped me during my stay in Japan.